



This is to certify that the

dissertation entitled

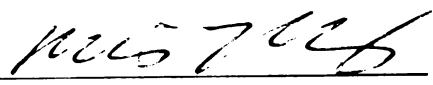
**Study on Optimized Upwind Schemes for
Computational Aeroacoustics and Extension
of a Fully Conservative Chimera to Finite
Difference Schemes**

presented by

Rangfu Chen

has been accepted towards fulfillment
of the requirements for

Ph.D. degree in Mech. Engr.


Major professor

Date November 19, 1998

PLACE IN RETURN BOX to remove this checkout from your record.
TO AVOID FINES return on or before date due.
MAY BE RECALLED with earlier due date if requested.

DATE DUE	DATE DUE	DATE DUE
<hr/>	<hr/>	<hr/>
<hr/>	<hr/>	<hr/>
<hr/>	<hr/>	<hr/>
<hr/>	<hr/>	<hr/>
<hr/>	<hr/>	<hr/>

**STUDY ON OPTIMIZED UPWIND SCHEMES FOR
COMPUTATIONAL AEROACOUSTICS AND EXTENSION
OF A FULLY CONSERVATIVE CHIMERA TO FINITE
DIFFERENCE SCHEMES**

By

Rangfu Chen

A DISSERTATION

Submitted to
Michigan State University
in partial fulfillment of the requirements
for the degree of

DOCTOR OF PHILOSOPHY

Department of Mechanical Engineering

1998

ABSTRACT

STUDY ON OPTIMIZED UPWIND SCHEMES FOR COMPUTATIONAL AREOACOUSTICS AND EXTENSION OF A FULLY CONSERVATIVE CHIMERA TO FINITE DIFFERENCE SCHEMES

By

Rangfu Chen

A computational methodology has been developed in the first part of the thesis for the simulations of acoustic radiation, propagation and reflection. The developed methodology is high order accurate, uses less grid points per wave length comparing to standard high order accurate numerical methods, and automatically damps out spurious short waves. Furthermore, the methodology can be applied to acoustic problems in the presence of objects with curved geometries. To achieve these results, high order accurate optimized upwind schemes, which are applied to discretize spatial derivatives on interior grid points, have been developed. High order accurate optimized one-side biased schemes, which are only applied to discretize the spatial derivatives on grid points near computational boundaries, have also been constructed. The developed schemes are combined with a time difference scheme to fully discretize acoustic field equations in multi-dimension in arbitrary curvilinear coordinates. Numerical boundary conditions are investigated and intuitively illustrated. Applications of the developed methodology to a sequence of one-dimensional and multi-dimensional acoustic problems are performed. The numerical results have validated the developed methodology and demonstrated advantages of the methodology over

central-difference Dispersion-Relation-Preserving method. Numerical results have also shown that the optimized upwind schemes minimize not only the dissipation error but also the dissipation error, while retaining the numerical stability.

The second part of the thesis deals with a fully conservative Chimera methodology. The fully conservative Chimera was originally developed based on a finite volume approach. A finite difference scheme is shown to be identical to a finite volume scheme with proper definition of control volumes and metrics. The fully conservative Chimera has been successfully extended to finite difference schemes for viscous flows including turbulence models and successfully implemented into NASA's widely used code OVERFLOW. In the implementation Roe's numerical fluxes are employed to compute the inviscid fluxes across the patch interfaces. The thin layer approximation is used in the calculating of viscous fluxes. The implementation also includes implicit treatment of the patch interfaces, which is shown to be extremely important to in stabilizing the overall time-marching procedure. The implementation of the fully conservative Chimera into the OVERFLOW allows the error in the traditional Chimera approach due to non-conservative data interpolations to be evaluated through direct comparisons. Tests on several inviscid, viscous laminar and turbulent, exterior flows with complex geometries are performed to validate the implementations and demonstrate superiority of the conservative Chimera methodology.

ACKNOWLEDGEMENT

I would like to express my sincere appreciations to the guidance committee, especially my advisor Dr. Mei Zhuang, for their valuable discussions and encouragement. I would like to thank Dr. Z. J. Wang of CFD Research Corporation (CFDRC) for his advice, help and encouragement on the second part of the thesis. With his recommendation and help, I have the opportunity to work in CFDRC where I gained a great deal of knowledge and experiences in Computational Fluid Dynamics (CFD), computer languages, graphics and operating systems. The work in the second part of the thesis was funded by NASA Ames Research Center under Contract NAS2-14226, with Dr. Pieter Buning being the technical monitor, Dr. Z. J. Wang being the principal investigator. Helps from many colleagues from CFDRC are very appreciated. The use of CFD-FASTRAN, CFD-GEOM, CFD-VIEW from CFDRC are gratefully acknowledged. Prof. Christopher K. W. Tam of Florida State University provided a sample code of the Dispersion-Relation-Preserving (DRP) method. His contribution is also gratefully acknowledged.

Special thanks go to my wife Ms. Fengxia Ji for taking good care of me and our energetic daughter Stephanie Chen, all the time. Without her great support, I would not have been able to work on and finish the thesis.

TABLE OF CONTENTS

	LIST OF TABLES	viii
	LIST OF FIGURES	ix
	LIST OF SYMBOLS	xv
1	INTRODUCTION	1
1.1	Background of Computational Aeroacoustics	1
1.2	Background of Conservative Chimera	6
1.3	Outline of the Thesis	8
2	ACOUSTIC FIELD EQUATIONS	11
2.1	Equations in Vector Form	11
2.2	Equations in Cartesian Coordinates	15
2.2.1	Three-Dimensional Equations	15
2.2.2	Two-Dimensional Equations	17
2.3	Equations in General Curvilinear Coordinates	17
2.3.1	Three-Dimensional Equations	17
2.3.2	Two-Dimensional Equations	22
2.4	Wave Decomposition	24
3	OPTIMIZED UPWIND SCHEMES	27
3.1	Model Wave Equation	27
3.2	Optimized Upwind Spatial Discretizations	31
3.3	Extension of Optimized Upwind Schemes to Acoustic Field Equations in Multi-Dimension	48

3.4	Time Discretizations	52
3.5	Boundary Conditions	55
3.5.1	Optimized One-Side Biased Spatial Discretizations Near Boundaries	57
3.5.2	Wall Boundary Condition	60
3.5.3	Radiation Boundary Condition	63
3.5.4	Outflow Boundary Condition.....	66
4	APPLICATION OF OPTIMIZED UPWIND SCHEMES.....	68
4.1	One-Dimensional Model Wave Equation	68
4.2	Acoustic Radiation from an Oscillating Piston.....	72
4.3	Acoustic Propagation in a Two-Dimensional Uniform Flow	79
4.4	Acoustic Reflections	83
4.4.1	Reflection of an Acoustic Pulse off a Straight Wall in a Two- Dimensional Uniform Flow	83
4.4.2	Scattering of an Acoustic Pulse off a Cylinder	85
4.4.3	Reflection of an Acoustic Pulse off a Sphere.....	90
5	FINITE DIFFERENCE VERSUS FINITE VOLUME DISCRETIZATIONS	93
5.1	Navier-Stokes Equations	93
5.2	Finite Difference Versus Finite Volume Discretizations.....	97
5.3	Finite Difference Grid and Finite Volume Grid	100
6	IMPLEMENTATION OF CONSERVATIVE CHIMERA IN OVERFLOW	102
6.1	Review of the Chimera Approach.....	102
6.2	Numerical Fluxes through the Patch Interface.....	104
6.3	Implicit Treatment of the Patch Interface	109

7	VALIDATION AND DEMONSTRATION OF THE FULLY CONSERVATIVE CHIMERA IN OVERFLOW	115
7.1	Transonic Flow Through a Channel with a 10% Bump.....	115
7.2	Laminar and Turbulent Boundary Layers over a Flat Plane	120
7.3	Grid Refinement Study with Turbulent Flow over a Two-Element Airfoil	123
7.4	Turbulent Flow over a Three-Element Airfoil	130
7.5	Summary	136
8	DEMONSTRATION OF THE FULLY CONSERVATIVE CHIMERA IN OVERFLOW	137
8.1	Hypersonic Flow Around a Launch Rocket.....	137
8.2	Demonstration of Local Refinement with Hypersonic Flow Around a Launch Rocket	139
8.3	Flow over a Wing and Store Combination.....	143
8.4	Transonic Flow Around a Combination of Wing and Missiles	147
9	CONCLUSIONS.....	152
9.1	Summary	152
9.2	Suggestions to Future Work.....	156
	REFERENCE.....	159

LIST OF TABLES

Table 1	Coefficients for the 7-stencil optimized upwind schemes45
Table 2	Coefficients for one-side biased schemes used in boundaries58

LIST OF FIGURES

Figure 1	Real part (a) and imaginary part (b) of effective numerical wavenumber versus wavenumber for 7-stencil schemes: Optimized upwind scheme ($N=4$, $M=2$, $P=4$); Tam & Webb's central DRP ($N=3$, $M=3$, $P=4$); Tam & Webb's backward DRP used near boundary ($N=4$, $M=2$, $P=4$); Standard six-order accurate upwind scheme ($N=4$, $M=2$, $P=6$).	47
Figure 2	Schematically showing the mapping of a physical space to a computational space.....	57
Figure 3	Effective numerical wavenumber versus wavenumber for one-side biased 7-stencil schemes: Present optimized scheme used near boundary ($N=5$, $M=1$, $P=4$); Tam & Webb's backward DRP used near boundary ($N=5$, $M=1$, $P=4$); Standard six-order accurate scheme ($N=5$, $M=1$, $P=6$).	59
Figure 4	Schematically showing acoustic, vorticity and entropy wave sources in a uniform flow.....	64
Figure 5	Comparison of exact and computed solutions at $t=400$ with different schemes for the one-dimensional modal wave equation with an initial Gaussian pulse.	70
Figure 6	Comparison of computational errors by different schemes for the one-dimensional modal wave equation with a initial Gaussian pulse.....	70
Figure 7	Comparison of exact solution and computed results at $t=200$ with (a): the optimized upwind schemes, (b): Tam and Webb's central DRP without damping, for the one-dimensional modal wave equation with an initial discontinuity.	71
Figure 8	Schematically showing the computational domain for acoustic radiation from an oscillating piston.....	72
Figure 9	Pressure distribution computed with the optimized upwind scheme at the beginning of a cycle.	75
Figure 10	Pressure contours at the beginning of a cycle computed with the optimized upwind scheme.....	76
Figure 11	Pressure contours at the beginning of a cycle computed with Tam and Webb's central DRP method without damping.....	76

Figure 12	Comparison of pressure distributions along the axis of symmetry at the beginning of a cycle.	77
Figure 13	Comparison of computational errors for pressure along the axis of symmetry at the beginning of a circle.	78
Figure 14	Schematically showing the computational domain, boundary conditions and initial disturbances for acoustic propagation in a two-dimensional uniform flow.	80
Figure 15	Density distribution computed with the optimized upwind scheme at $t=80$	80
Figure 16	The comparison of density distributions along the line $y=x$ at $t = 80$	82
Figure 17	The comparison of computational errors for density along the line $y=x$ at $t = 80$	82
Figure 18	Pressure distribution computed with the optimized upwind scheme at $t=80$	83
Figure 19	The comparison of computational errors for pressure along the wall at $t = 80$	84
Figure 20	The comparison of computational errors for pressure along the line $x=0$ at $t=80$	85
Figure 21	Schematic diagram showing the computational domain and boundaries of acoustic scattering problem.	86
Figure 22	Pressure distribution computed with the optimized upwind scheme at $t = 7$ for the first case in which an acoustic pulse is released initially.	88
Figure 23	Time history of pressure fluctuation at points A, B and C as indicated in Figure 21.	88
Figure 24	Pressure wave pattern at $t = 40$ simulated by the optimized upwind scheme.	89
Figure 25	Directivity of radiated sound computed by the optimized upwind scheme.	89
Figure 26	Pressure patterns on the surface of the sphere and the plane of $z = 0$ at $t = 2.5$	92

Figure 27	Pressure patterns on the surface of the sphere and the planes of $x=0$, $y=0$ and $z=0$ at $t=2.5$92
Figure 28	Coordinate transformation and the grid cell around grid point (i, j, k).....95
Figure 29	Schematically showing finite volume grid (solid line) and mutual finite difference grid (dash line).101
Figure 30	Schematically showing cut cells, smallest faces and patch interface.103
Figure 31	Two-zonal overlapped grid system for the transonic flow over a 10% bump.116
Figure 32	Pressure contours computed using OVERFLOW with the conservative Chimera.....117
Figure 33	Pressure contours computed using OVERFLOW with the original Chimera.....117
Figure 34	Comparison of pressure coefficients profiles on lower wall of the channel. 118
Figure 35	Comparison of convergence histories in using OVERFLOW with the conservative Chimera and the original Chimera.118
Figure 36	Grids after local refinement for the simulation of flow over a bump by OVERFLOW with the conservative Chimera.119
Figure 37	Pressure contours computed by OVERFLOW with the conservative Chimera and with local grid refinement.....119
Figure 38	Grids for the study of boundary layer growth over a flat plane120
Figure 39	Velocity distributions cross interfaces between major and minor grids inside the turbulent boundary layer over a flat plane.121
Figure 40	Velocity contours cross interfaces between major and minor grids inside the laminar boundary layer over a flat plane.....122
Figure 41	Velocity contours cross interfaces between major and minor grids inside the turbulent boundary layer over a flat plane.....122
Figure 42	Velocity contours cross interfaces between major and minor grids inside the laminar boundary layer over a flat plane.....122
Figure 43	The coarse grid for the turbulent flow over the two-element airfoil124

Figure 44	Patch interface for the conservative Chimera in the coarse grid.....	124
Figure 45	Holes cut for the original Chimera in the coarse grid.....	125
Figure 46	Mach contours around two-element airfoil computed by OVERFLOW with the conservative Chimera.	127
Figure 47	Mach contours around two-element airfoil computed by OVERFLOW with the original Chimera.	127
Figure 48	Pressure contours around two-element airfoil computed by OVERFLOW with the conservative Chimera.	128
Figure 49	Pressure contours around two-element airfoil computed by OVERFLOW with the original Chimera.	128
Figure 50	Convergence histories for OVERFLOW with conservative Chimera and original Chimera in the fine grids.	129
Figure 51	Pressure distributions along the airfoil computed by OVERFLOW with the original and the conservative Chimera in different levels of grids.	129
Figure 52	Pressure distributions along the rear airfoil computed by OVERFLOW with the original and the conservative Chimera in different levels of grids.	130
Figure 53	Medium grids and patch interfaces for the thee-element airfoil	131
Figure 54	Pressure contours around the three-element airfoil computed using OVERFLOW with the conservative Chimera on the finest grid.	132
Figure 55	Pressure contours around the three-element airfoil computed using OVERFLOW with the original Chimera on the finest grid.	132
Figure 56	Pressure distributions along airfoil surfaces computed using OVERFLOW with the original Chimera.	134
Figure 57	Pressure distributions along airfoil surfaces computed using OVERFLOW with the conservative Chimera.....	134
Figure 58	Comparison of pressure distributions along the airfoil surfaces computed using OVERFLOW with the conservative and the original Chimera.	135
Figure 59	Comparison of pressure distributions for the inviscid flow along the airfoil surfaces computed with OVERFLOW.....	135

Figure 60	Four zone Chimera grid for hypersonic flow around a launch rocket.....	138
Figure 61	Mach distributions on the surfaces of the rocket and the boosters and on the last cross-streamwise plane computed using OVERFLOW with the conservative Chimera.....	138
Figure 62	Mach contours on the surfaces of the rocket and the boosters.	139
Figure 63	Grids around the rocket and the boosters with local refinement.....	140
Figure 64	Mach contours on the body surfaces and on the last cross stream plane simulated with OVERFLOW with the conservative Chimera.	141
Figure 65	Density contours on the body surfaces computed with OVERFLOW with the conservative Chimera.....	142
Figure 66	Mach distributions on the body surfaces and some sections simulated with CFD-FASTRAN with local grid refinement.	142
Figure 67	Mach contours on the body surfaces simulated with CFD-FASTRAN with local grid refinement.	143
Figure 68	Grids and the configuration of the wing-store combination.	144
Figure 69	Patch interfaces, smallest faces and holes cut by the ZIG.	144
Figure 70	Pressure contours on the surfaces of the wing and the store and on one spanwise section computed using OVERFLOW with the conservative Chimera.....	145
Figure 71	Mach contours on the surfaces of the wing and the store and on a spanwise section computed using OVERFLOW with the conservative Chimera.....	146
Figure 72	Residual history for the simulation of flow over wing and store combination by OVEFLOW with conservative chimera.	146
Figure 73	Configuration of the combination of wing and two missiles.	147
Figure 74	Grids for the combination of wing and two missiles.	148
Figure 75	Holes automatically cut in the ZIG.....	148
Figure 76	Pressure contours on the surfaces and two streamwise sections simulated using OVEFLOW with the conservative Chimera.	150

Figure 77	Pressure contours on the surfaces and two streamwise sections simulated using CFD-FASTRAN with the conservative Chimera.....	150
Figure 78	Pressure contours on the surfaces and two spanwise sections simulated using OVEFLOW with the conservative Chimera.	151
Figure 79	Pressure contours on the surfaces and two spanwise sections simulated using CFD-FASTRAN with the conservative Chimera.	151

LIST OF SYMBOLS

Roman Symbols

A, B, C	Jacobian matrices with respect to the conservative variable vector in x, y, z directions respectively
A_0, B_0, C_0	Jacobian matrices with respect to the mean flow primitive variable vector in x, y, z directions respectively
\mathcal{A}	Jacobian matrix for the smallest face
$\tilde{A}, \tilde{B}, \tilde{C}$	Jacobian matrices with respect to conservative variable vector in the generalized curvilinear coordinate ξ, η, ζ directions respectively
$\tilde{A}_0, \tilde{B}_0, \tilde{C}_0$	Jacobian matrices with respect to the mean flow primitive variable vector in the generalized curvilinear coordinate ξ, η, ζ directions respectively
$\vec{E}, \vec{F}, \vec{G}$	Inviscid flux vectors in x, y, z directions respectively
$\vec{E}_v, \vec{F}_v, \vec{G}_v$	Viscous flux vectors in x, y, z directions respectively
\mathcal{F}	Flux through the smallest face
$\tilde{\mathcal{F}}$	Numerical approximation to the flux through the smallest face
J	Determinant of the Jacobian matrix of generalized curvilinear transform
M, N	Stencils from the right and left
\vec{Q}	Conservative flow variable vector
R	Specific gas constant, right cell, curvature radius of the wall
\vec{R}	Vector of right hand side of discretized equations, magnitude vector in fundamental solutions
S	Cell face, face area
\vec{S}	Right hand side of acoustic field equations, source term vector

T	Temperature, eigenvector matrix in one-dimension
T_ξ, T_η, T_ζ	Eigenvector matrices corresponding to $\tilde{A}, \tilde{B}, \tilde{C}$ or $\tilde{A}_0, \tilde{B}_0, \tilde{C}_0$
V	Magnitude of velocity, cell volume
\vec{V}	Velocity vector
\tilde{V}	Relative speed of sound to the mean flow
a_j, a_j^{NM}	Coefficients in finite different schemes to discretize spatial derivatives
b_l	Coefficients in finite different schemes to discretize temporal derivatives
c	Speed of sound, propagating speed of scalar wave equation
c_v	Specific heat at constant volume
e	Internal energy per unit mass
e_t	Total energy per unit mass
i, j, k, l	Grid point indices
i	The pure imaginary number
\vec{n}	Face normal
p	Pressure
\vec{q}	Primitive variable vector
\vec{r}	Position vector
t	Time
u, v, w	Velocity components in x, y, z directions respectively
v_p	Wave phase velocity
v_g	Wave group velocity
x, y, z	Cartesian coordinates

Greek Symbols

α	Wavenumber
$\bar{\alpha}$	Effective numerical wavenumber
β_0	Parameter in optimization procedure
γ	Specific heat ratio
Δt	Time step
$\Delta x, \Delta y, \Delta z$	Space steps in x, y, z directions respectively
$\Delta \xi, \Delta \eta, \Delta \zeta$	Space steps in the generalized curvilinear coordinate ξ, η, ζ directions respectively
Δ_ξ, ∇_ξ	Forward and backward-difference operators in ξ direction
δ_{ij}	Kronecker delta function
$\delta_\xi, \delta_\eta, \delta_\zeta$	Central difference operators in the generalized curvilinear coordinate ξ, η, ζ directions respectively
$\varepsilon_2, \varepsilon_4$	Second order and fourth order dissipation coefficients respectively
θ	Angle
θ_0	Generic mean flow velocity component in the generalized curvilinear coordinates
κ	Thermal conductivity
$\Lambda_\xi, \Lambda_\eta, \Lambda_\zeta$	Diagonal eigenvalue matrices corresponding to matrices $\tilde{A}_0, \tilde{B}_0, \tilde{C}_0$ in the generalized curvilinear coordinate ξ, η, ζ directions respectively
$\tilde{\Lambda}_\xi, \tilde{\Lambda}_\eta, \tilde{\Lambda}_\zeta$	Diagonal eigenvalue matrices corresponding to matrices $\tilde{A}, \tilde{B}, \tilde{C}$ in the generalized curvilinear coordinate ξ, η, ζ directions respectively
λ	Eigenvalue, weighting coefficient in optimization procedure
μ_L, μ_T	Laminar viscosity and turbulence eddy viscosity respectively
ξ, η, ζ	General curvilinear coordinates

ρ	Density
σ	Parameter in optimization procedure
$\vec{\Phi}$	Fundamental solution vector
ϕ	Phase in the fundamental solution for scalar model wave equation
ϕ_1, ϕ_2	Angles
ϕ_s	Phase in the fundamental solution for semi-discrete scalar model wave equation
φ	Fundamental solution for scalar model wave equation
φ_s	Fundamental solution for semi-discrete scalar model wave equation
ω	Frequency
$\bar{\omega}$	Effective numerical frequency

Ancillary Symbols

$(\tilde{})$	Fourier transform, numerical approximation, quantity in the generalized curvilinear coordinate
$(\bar{})$	Numerical approximations to the inviscid and viscous fluxes
$()_0$	Mean flow quantity
$()_L$	Quantity evaluated at left cell L
$()_R$	Quantity evaluated at right cell R
$()_{i,j,k}$	Quantity evaluated at cell (i, j, k)
$()^+$	Matrix with only non-negative eigenvalues in matrix splitting procedure
$()^-$	Matrix with only non-positive eigenvalues in matrix splitting procedure
$()'$	Disturbance with respect to the mean flow quantity
$()^{(n)}$	Quantity at time level n

1 INTRODUCTION

The thesis contains two relatively independent parts. The first part is about the study and applications of optimized upwind schemes for Computational Aeroacoustics (CAA). The second part is on extending a fully conservative Chimera algorithm to finite difference schemes and implementing it in NASA's widely used OVERFLOW code.

1.1 Background of Computational Aeroacoustics

Aeroacoustic problems arise in many engineering applications such as jet noise, automobile noise, fan and turbomachinery noise, propeller and helicopter noise, duct acoustics, and especially aircraft noise (Eversman, 1991). As air traffic continues to increase quickly, the Federal Aviation Regulation (FAR) is expected to enforce stricter rules which require 3-4 dB reduction in current aircraft noise levels (Mecham *et al.*, 1994). The ability to predict and reduce noise levels efficiently has become increasingly important to both aircraft industry and government agencies such as NASA. As a field of study on the generation and propagation of sound in aerodynamic flow fields, aeroacoustics is getting more and more attentions. Current methods used in aeroacoustics, however, rely on simple theoretical models which are not able to well characterize acoustic waves, or experimental tests which are usually expensive and time-consuming to carry out (Motsinger *et al.*, 1991). CAA emerged as a relatively new area of research which focuses on numerically predicting the generation and propagation of sound in aerodynamic flow fields (Hardin *et al.*, 1995). With continuous advancement in computer hardware and software, CAA will

gradually reach its goal to accurately compute sound generating mechanisms, directivity, spectral features and the propagation of the sound to the far field. CAA has the potential to finally provide design engineers a useful tool in a design environment to fully and rapidly assess the effect that changes in the product or product environment have on the sound field.

Aeroacoustic problems are governed by the same equations as those in aerodynamics, namely the Navier Stokes equations. Aeroacoustic problems, however, have their own nature, characteristics and objectives, which are distinctly different from those commonly encountered in aerodynamics (Tam, 1995). First of all, aeroacoustic noises are inherently unsteady which implies that accurate time-dependent calculations should be performed. The need to accurately resolve the temporal fluctuations in the calculation requires that a sufficient number of time steps are included in each period resolved. In order to perform spectral analysis of the computed solution, a long-time computation is necessary. Second of all, acoustic waves can cover a broad frequency range. To cover the range of human hearing, for example, frequencies from 50 Hz to 20 kHz would need to be resolved. This would require both a large domain to resolve at least one wavelength of the longest wave and a fine mesh to accurately resolve the shortest wave. Third of all, fluctuations caused by acoustic waves are typically very small. The fluctuation velocities associated with the jet noise, for example, are four orders of magnitude smaller than the mean flow, which could even be smaller than the numerical errors incurred in the computation of mean flow. Finally, boundary conditions should be placed in the far field such that acoustic waves can go out of the boundary without reflections. These characteristics for aeroacoustic problems demand numerical schemes be almost free of numerical dispersions and dissipations

to enforce that the obtained numerical waves travel over a long distance with accurate speed and magnitude, and make computation of aeroacoustic waves challenging.

Current computer hardwares are not capable of predicting sound generation and propagation by directly performing three-dimensional, time dependent computation of flow past or through arbitrary complex geometries. The memory and CPU requirements by the direct numerical simulation of the full Navier-Stokes equations are prohibitive, although very high order accurate computational methods may be used so that the numerical error is order smaller than acoustic fluctuations. Alternative less expensive computational approaches must be used. Non-linearity, however, is crucial to the noise generation process which is related to turbulence in the flow. Currently used turbulence modeling is a barrier to resolve the generation process. Turbulence models, which are computationally cheap, but model the physics necessary to adequately resolve the mechanisms of sound generation, are needed.

Nevertheless, different approaches with some simplifications had been developed and are currently being researched. The approach which combines near- and far-field analysis numerically solves the Navier-Stokes with turbulence models or large eddy simulation (LES) near source region (Duque *et al.*, 1995, 1996, Lim *et al.*, 1993). The acoustic far field is determined with the Acoustic Analogy or Kirchhoff method. The Acoustic Analogy originally introduced by Lighthill (1952) is most developed method and widely in use in the aircraft industry. The Kirchhoff method originally suggested by Hawkings is currently under development and gaining popularity as the higher resolution aerodynamics and more powerful computer are getting available (Farassat, 1996). Another approach is to first solve the Navier-Stokes to obtain mean flow solution. The set of linear equations gov-

erning the acoustic field obtained by perturbing the Navier-Stokes equations about the mean flow are then solved. The effect of viscosity on the propagation of sound is neglected. A set of numerical schemes with least numerical dispersion and dissipation must be developed to solve the linear equations for acoustic waves. This approach is current trend of Computational Fluid Dynamics based (CFD-based) CAA, which is under development and is the least mature compared to the Acoustic Analogy and Kirchhoff methods.

CFD has made rapid progress over the past two decades in many aspects including grid generation and algorithms. Grid generation techniques, for example, had advanced from very beginning Cartesian uniform grid to body-fitted arbitrary curvilinear grids, from single zonal grid to multi-zonal Chimera grids, from structured to unstructured polyhedral grids (Mavriplis, 1995). High resolution schemes such as Total Variation Diminishing (TVD) and essentially non-oscillatory (ENO) schemes were developed in dealing with the discontinuities such as shock waves in the flow field (Chakravarthy *et al.*, 1987, Harten *et al.*, 1987, Yee, 1989). Various implicit schemes have been proposed and applied to unstructured grids to accelerate convergence to the steady state (Blanco *et al.*, 1998, Venkatakrishnan, 1995). CFD is being increasingly employed as a valuable tool for design in many industries, such as aircraft industry for aircraft load prediction, and automotive for underhood convection heat transfer, and etc. Current CFD commercial codes are able to provide an integrate tool on the geometry definition, grid generation, physical model definition, flow solver and field visualization (CFD Research Corporation, 1993, 1998). However, they are using standard low-order methods (usually second order) and are designed for the computation of mean flows (Buning *et al* 1991). Their applications to CAA are not truly feasible because of the enormous computer memory and time requirements.

Many CFD schemes such as the MacCormack scheme, standard upwind schemes and ENO etc. have been extended to higher order using more stencil points and applied to the computation of acoustic problems (Hardin *et al.*, 1995, Hixon, 1997). Many compact and non-compact optimized schemes including Tam and Webb's Dispersion-Relation-Preserving (DRP) schemes were designed for the linear acoustic waves (Kim *et al.*, 1997, Lele, 1992, Lin *et al.*, 1995, 1997, Tam and Webb, 1993, Tam *et al.*, 1993, Zhuang *et al.*, 1997, 1998, Zigg *et al.*, 1993). It has been shown that for waves with high wavenumbers (short waves) optimized schemes require less grid points per wavelength (PPW) than traditional high order CFD schemes. The property of requiring less PPW is essential in CAA, since a large computational domain is usually required. Most optimized schemes, however, are restricted to central difference algorithms (Lockard *et al.*, 1995, Zigg, 1997). This restriction inevitably leads to stability problems. Spurious oscillations in numerical solutions are generated, when there are discontinuities in flow field which are often encountered near objects. The elimination of the spurious oscillations must be dealt with through the use of filters or explicit dissipation terms. Although filters or dissipation terms are proved quite successful in many acoustic problems, they are problem-dependent and require the prior knowledge of the problems.

Upwind schemes have been widely used in CFD and shown very efficient and robust (Anderson *et al.*, 1984, Barth, 1990, Warming *et al.*, 1975, Li, 1997). Upwind schemes ensure that waves propagate in correct physical directions. With the built-in dissipation, upwind schemes automatically damp out high wavenumbers component in the solution. Since the dissipation does not distinguish the spurious waves from actual acoustic waves, upwind schemes need to be optimized so that the effects of dissipation on a large range of

acoustic waves are minimized. It is our objective of the thesis to investigate, develop and apply high order, optimized, upwind schemes for CAA.

1.2 Background of Conservative Chimera

The generation of a computational grid may require up to eighty percent of total work for a CFD flow simulation with complex geometries. There is a great demand of automatic grid generation to reduce the extensive requirement of the man power in grid generation. Unstructured grid approach seems to be the most promising for the automatic grid generation and is getting dominant in commercial CFD flow solvers nowadays. Unstructured grid, however, imposes difficulties on the control of qualities of grid cells. Stability and accuracy associated to numerical schemes are usually sensitive to the qualities of grid cells. This is particularly true when dealing with viscous laminar and turbulent flows. Severely screwed cells certainly reduce the order of accuracy of numerical schemes and bring out the instability to the numerical results. Furthermore, unstructured grid requires more memory and CPU overhead because the connectivity of grid cells must be explicitly described. In a structured grid the connectivity of grid cells is simply implied in grid indices. The structured grid, however, is very difficult to handle complex geometries. Multi-zonal overlapped structured grid approach (Chimera) was first introduced about a decade ago by Steger et al and Benek *et al* (Benek *et al.*, 1983, Steger *et al.*, 1983, 1985). Chimera approach divides the computational domain into a number of geometrically simple sub-domains (zones or blocks) for which independent structured grids can be easily generated. Chimera approach keeps the simplicity of structured grid, while having the flexibility in grid generation and on the control of grid qualities. This approach can also dramatically

reduce the degree of difficulty and man power required for the grid generation. Since its introduction to the CFD, Chimera approach has been very attractive and extended to solve both steady and unsteady Navier-Stokes equations for complex geometries (Eberhardt *et al.*, 1985, Parks *et al.*, 1991, Rogers *et al.*, 1992, 1994, Soetrisno *et al.*, 1994). Several widely used CFD codes in the aerospace industry such as OVERFLOW (Buning *et al.*, 1991) and CFL3D have include the Chimera approach.

With Chimera, each independent grid is generated in each zone and the grids between the neighboring zones are overlapped. During the computation the values of flow variables between the overlapped grids must be exchanged. In the traditional approach, the inter-grid communications are accomplished through data interpolation. As a results, the conservation form of the numerical discretization is lost even if a conservative scheme is used in each grid of the system. Although there are debates on whether conservation is necessary for smooth flows, it is generally recognized that the non-conservative data interpolation approach may cause problems across discontinuities. There was an evidence that conservation for the internal flow through a nozzle must be guaranteed to correctly predict the thrust of a rocket engine (Davis *et al.*, 1992). Furthermore, the Navier-Stokes equations are obtained from the conservations laws and Lax (1972) mathematically proved that the solutions of a conservative scheme guarantee the correct propagation speeds of discontinuities provided the solutions convergence.

Since it was realized that the data interpolation has the deficiency of losing conservation when the Chimera was first proposed, extensive research efforts have been devoted to improved the conservative properties of Chimera (Berger, 1987, Moon *et al.*, 1989, Wang and Yang, 1995). But the full conservation in Chimera is not successfully accomplished

until recently Wang and Yang (1995) developed a fully conservative Chimera approach. Wang *et al* first implemented the fully conservative Chimera into an inviscid flow solver and later successfully extent to tackle three-dimensional flow problems for the first time.

The fully conservative Chimera was developed originally based on finite volume approach (Wang *et al.*, 1994, 1995). The OVERFLOW which is being widely used in the industry and government agency was written based on finite different approach. The OVERFLOW includes the ability of Chimera with traditional data interpolation. It is our objective to extend the fully conservative Chimera to the OVERFLOW. The implementation of the fully conservative Chimera into the OVERFLOW allows the errors in the traditional Chimera approach due to non-conservative data interpolations to be evaluated through direct comparison. The OVERFLOW is a huge software packages for the simulation of compressible flows. The OVERFLOW of version *1.6ap* after the implementation of the fully conservative Chimera contains about a hundred thousand lines of source codes in FORTRAN. The work of extension and implementation of the fully conservative Chimera in the OVERFLOW is part of SBIR Phase II project of “A Fully Conservative Chimera Approach for Structured/Unstructured Grids in Computational Fluid Dynamics” supported by NASA Ames Research Center with Dr. Z.J. Wang from CFDRC as the principle investigator and Dr. Pieter Buning as the technical monitor.

1.3 Outline of the Thesis

Chapters 2, 3 and 4 are devoted to the first part of the thesis, the study on optimized upwind schemes for computational aeroacoustics and applications of the schemes to acoustic problems. Chapter 2 derives the acoustic field equations in different forms from

the Euler equations by ignoring second and higher order small perturbation terms. The properties and Jacobian matrices associated to the acoustic field equations in the generalized curvilinear coordinate system are also derived in this chapter. Chapter 3 is devoted to the development and construction of the optimized upwind schemes. The properties of model wave equations are introduced. The schemes in one dimension are developed first by minimizing the difference of numerical effective wavenumber and actual wavenumber. A fourth order accurate, 7-stencil, optimized, upwind scheme is given. The generation of the schemes to the acoustic field equations in the generalized curvilinear coordinate system is included. Detailed boundary conditions and optimized one-side biased schemes used for grid points near the boundary are also given. In Chapter 4, the developed 7-stencil optimized upwind scheme is first validated with one-dimensional model wave equation. Then applications of the optimized upwind schemes to multi-dimensional benchmark problems are carried out. Comparisons of the numerical solutions with analytical solutions are made to show the advantages of the optimized upwind schemes over the central DRP method. Finally the optimized upwind schemes are applied to the two-dimensional and three-dimensional acoustic problems with the presence of curved objects.

Chapter 5, 6, 7 and 8 are for the extension of the fully conservative Chimera to finite difference schemes, implementation in the OVERFLOW, and validation and demonstration of the implementation. Chapter 5 reviews the fully conservative Chimera based on the finite volume approach. The differences between finite volume and finite difference discretizations are illustrated. Chapter 6 describes the implementation of the fully conservative Chimera in the OVERFLOW. In this chapter the emphasizes are on the implicit treatments of the patch interface which is very sensitive to the stability and convergency.

Chapter 7 is devoted to the validation of the implementation of the fully conservative Chimera in the OVERFLOW. A sequence of inviscid, laminar and turbulent flows are simulated by the OVERFLOW with the conservative Chimera. The direct comparisons between the fully conservative Chimera and the traditional Chimera are made. Chapter 8 demonstrates cases to show the capability of the conservative Chimera in tackling more complicate flow problems.

Chapter 9 summarizes the conclusions obtained in the thesis. The suggestions for the future work is also included in this chapter.

2 ACOUSTIC FIELD EQUATIONS

The generation and propagation of sound in aerodynamics flow fields can be mathematically described by Navier-Stokes equations. As mentioned in the introduction, it is prohibitively expensive to predict sound propagation and radiation by the direct numerical simulation of the full Navier-Stokes equations. On the other hand, the disturbances associated with the sound wave are small and the effect of viscosity on the propagation and radiation of the sound is negligible. Therefore the modeling of acoustic field can be based on the linearization of equations governing the motion of an inviscid, non-heat-conducting perfect gas, i.e. the Euler equations.

2.1 Equations in Vector Form

The continuity equation which describes the conservation of mass can be written as:

$$\frac{\partial \rho}{\partial t} + (\vec{V} \cdot \nabla)\rho + \rho(\nabla \cdot \vec{V}) = 0 \quad (2.1)$$

where ρ , p and \vec{V} are density, pressure and velocity respectively. The inviscid momentum equations, i.e. the Euler equations, can be written as the following:

$$\rho \left(\frac{\partial \vec{V}}{\partial t} + (\vec{V} \cdot \nabla)\vec{V} \right) = -\nabla p \quad (2.2)$$

For the inviscid flow without the absorption of radiation originating outside the system or the local emission of radiation by the fluid itself, the energy equation derived from the

conservation of energy is usually written as:

$$\frac{\partial}{\partial t} \left(e + \frac{V^2}{2} \right) + (\vec{V} \cdot \nabla) \left(e + \frac{V^2}{2} \right) = -\nabla \cdot (p\vec{V}) \quad (2.3)$$

where e is the internal energy per unit mass and V is the magnitude of velocity \vec{V} , i.e. $V^2 = \vec{V} \cdot \vec{V}$. Using the notation of substantial derivative (material derivative)

$$\frac{D}{Dt} = \frac{\partial}{\partial t} + (\vec{V} \cdot \nabla) \quad (2.4)$$

and noticing

$$\frac{D}{Dt} \left(e + \frac{V^2}{2} \right) = \frac{De}{Dt} + \vec{V} \cdot \frac{D\vec{V}}{Dt} \quad (2.5)$$

$$\nabla \cdot (p\vec{V}) = p\nabla \cdot \vec{V} + \vec{V} \cdot \nabla p \quad (2.6)$$

and combining the Euler equation (2.2), we can write the energy equation (2.3) in the following form:

$$\rho \frac{De}{Dt} = -p\nabla \cdot \vec{V} \quad (2.7)$$

For a perfect gas, the equation of state, the specific heat at constant volume c_v and the internal energy e can be respectively written as the followings:

$$p = \rho RT \quad c_v = \frac{R}{\gamma - 1} \quad e = c_v T = \frac{1}{\gamma - 1} \frac{p}{\rho},$$

where T is the temperature, γ is the specific heat ratio and R is the specific gas constant.

The specific heat ratio and the gas constant have different values for different gases. For air at the standard condition, for example, $\gamma = 1.4$ and $R = 287 \text{ J}/(\text{kg} \cdot \text{K})$. With the above relations, we have

$$\rho \frac{De}{Dt} = \frac{1}{\gamma - 1} \rho \frac{D}{Dt} \left(\frac{p}{\rho} \right) = \frac{1}{\gamma - 1} \left(\frac{Dp}{Dt} - \frac{1}{\rho} \frac{D\rho}{Dt} \right) \quad (2.8)$$

Using the continuity equation (2.1) and substituting (2.8) into (2.7), we get the energy equation for the inviscid perfect gas written as the following:

$$\frac{\partial p}{\partial t} + (\vec{V} \cdot \nabla)p + \gamma p (\nabla \cdot \vec{V}) = 0 \quad (2.9)$$

We use the continuity equation (2.1), the Euler equations (2.2) and the energy equation (2.9) to derive the acoustic field equations for the perfect gas. Consider the small perturbations on the mean state of a flow, ρ_0 , p_0 and \vec{V}_0 , so that

$$\rho = \rho_0 + \rho'$$

$$p = p_0 + p'$$

$$\vec{V} = \vec{V}_0 + \vec{V}'$$

The resulting acoustic field equations, after second order and higher order terms in the small perturbations in the continuity equation, Euler equations and the energy equation are ignored, are written as the following:

$$\frac{\partial \rho'}{\partial t} + (\vec{V}_0 \cdot \nabla)\rho' + (\vec{V}' \cdot \nabla)\rho_0 + \rho_0(\nabla \cdot \vec{V}') + \rho'(\nabla \cdot \vec{V}_0) = 0 \quad (2.10)$$

$$\rho' \left(-\frac{1}{\rho_0} \nabla p_0 \right) + \rho_0 \left(\frac{\partial \vec{V}'}{\partial t} + (\vec{V}_0 \cdot \nabla) \vec{V}' + (\vec{V}' \cdot \nabla) \vec{V}_0 \right) = -\nabla p' \quad (2.11)$$

$$\frac{\partial p'}{\partial t} + (\vec{V}_0 \cdot \nabla) p' + (\vec{V}' \cdot \nabla) p_0 + \gamma p_0 (\nabla \cdot \vec{V}') + \gamma p' (\nabla \cdot \vec{V}_0) = 0 \quad (2.12)$$

They are representing acoustic continuity, acoustic momentum and acoustic energy respectively. Here we have used the fact that the mean states ρ_0 , p_0 and \vec{V}_0 satisfy the continuity equation, Euler equations and the energy equation. From now on, the prime used for the perturbations will be dropped for simplicity. Putting all the derivative terms of the perturbations to the left hand side and all the terms without derivatives of the perturbations to the right hand side, we can write the acoustic field equations as the following:

$$\frac{\partial \rho}{\partial t} + (\vec{V}_0 \cdot \nabla) \rho + \rho_0 (\nabla \cdot \vec{V}) = -(\vec{V} \cdot \nabla) \rho_0 - \rho (\nabla \cdot \vec{V}_0) \quad (2.13)$$

$$\frac{\partial \vec{V}}{\partial t} + (\vec{V}_0 \cdot \nabla) \vec{V} + \frac{1}{\rho_0} \nabla p = -(\vec{V} \cdot \nabla) \vec{V}_0 + \frac{1}{\rho_0} \rho \nabla p_0 \quad (2.14)$$

$$\frac{\partial p}{\partial t} + (\vec{V}_0 \cdot \nabla) p + \gamma p_0 (\nabla \cdot \vec{V}) = -(\vec{V} \cdot \nabla) p_0 - \gamma p (\nabla \cdot \vec{V}_0) \quad (2.15)$$

They are called acoustic continuity, acoustic momentum and acoustic energy respectively. It can be easily shown that the above equations will remain the same in non-dimensional form providing the scaled factors are given as the follows: the density ρ is scaled by ρ_r (a reference density), the velocity \vec{V} is scaled by c_r (the reference speed of sound), pressure p is scaled by $\rho_r c_r^2$, time t is scaled by L/c_r where L is a suitable reference length, and the spatial coordinates are scale by L . If there is no mean flow, i.e. $\vec{V}_0 = 0$, there are only

acoustic disturbances. From equations (2.13), (2.14) and (2.15), we have

$$\frac{\partial \rho}{\partial t} + \rho_0 (\nabla \cdot \vec{V}) = 0 \quad (2.16)$$

$$\frac{\partial \vec{V}}{\partial t} + \frac{1}{\rho_0} \nabla p = 0 \quad (2.17)$$

$$\frac{\partial p}{\partial t} + \gamma p_0 (\nabla \cdot \vec{V}) = 0 \quad (2.18)$$

Now the acoustic continuity equation (2.16) and energy equation (2.18) are identical because $p = \gamma \frac{p_0}{\rho_0} \rho$. Taking time derivative on equation (2.18) and substituting (2.17) into (2.18), we have

$$\frac{\partial^2 p}{\partial t^2} = \gamma \frac{p_0}{\rho_0} (\nabla \cdot \nabla) p = c_0^2 \Delta p \quad (2.19)$$

which is the standard second order scalar wave equation with the speed c_0 of sound as the propagating speed, where $c_0^2 = \gamma \frac{p_0}{\rho_0}$ and $\Delta = \nabla \cdot \nabla$ is the Laplace operator.

2.2 Equations in Cartesian Coordinates

2.2.1 Three-Dimensional Equations

In three-dimensional Cartesian coordinate system (x, y, z) , we have $\vec{V} = (u, v, w)$, where u , v and w are the velocity components in x -, y - and z -directions respectively. Denote variable vector $\vec{q} = (\rho, u, v, w, p)$ which is referred as primitive variable vector,

we can write acoustic field equations in three-dimensional Cartesian coordinate system as:

$$\frac{\partial \vec{q}}{\partial t} + A_0 \frac{\partial \vec{q}}{\partial x} + B_0 \frac{\partial \vec{q}}{\partial y} + C_0 \frac{\partial \vec{q}}{\partial z} = \vec{S} \quad (2.20)$$

where the components of vector \vec{S} are the right hand side of acoustic field equations (2.13), (2.14) and (2.15). \vec{S} depends on the flow field variations. For a uniform mean flow and no noise sources are presented, $\vec{S} = 0$. The Jacobian matrices A_0 , B_0 and C_0 , which depend on the mean states only, can be written respectively as the following:

$$A_0 = \begin{bmatrix} u_0 & \rho_0 & 0 & 0 & 0 \\ 0 & u_0 & 0 & 0 & \frac{1}{\rho_0} \\ 0 & 0 & u_0 & 0 & 0 \\ 0 & 0 & 0 & u_0 & 0 \\ 0 & \gamma p_0 & 0 & 0 & u_0 \end{bmatrix} \quad (2.21)$$

$$B_0 = \begin{bmatrix} v_0 & 0 & \rho_0 & 0 & 0 \\ 0 & v_0 & 0 & 0 & 0 \\ 0 & 0 & v_0 & 0 & \frac{1}{\rho_0} \\ 0 & 0 & 0 & v_0 & 0 \\ 0 & 0 & \gamma p_0 & 0 & v_0 \end{bmatrix} \quad (2.22)$$

$$C_0 = \begin{bmatrix} w_0 & 0 & 0 & \rho_0 & 0 \\ 0 & w_0 & 0 & 0 & 0 \\ 0 & 0 & w_0 & 0 & 0 \\ 0 & 0 & 0 & w_0 & \frac{1}{\rho_0} \\ 0 & 0 & 0 & \gamma p_0 & w_0 \end{bmatrix} \quad (2.23)$$

2.2.2 Two-Dimensional Equations

In two-dimensional Cartesian coordinate system, say, (x, y) , then velocity $\vec{V} = (u, v)$ and flow variable vector $\vec{q} = (\rho, u, v, p)$. The acoustic field equations in two-dimensional Cartesian coordinate system become:

$$\frac{\partial \vec{q}}{\partial t} + A_0 \frac{\partial \vec{q}}{\partial x} + B_0 \frac{\partial \vec{q}}{\partial y} = \vec{S} \quad (2.24)$$

The matrices A_0 , and B_0 can be respectively written as follows:

$$A_0 = \begin{bmatrix} u_0 & \rho_0 & 0 & 0 \\ 0 & u_0 & 0 & \frac{1}{\rho_0} \\ 0 & 0 & u_0 & 0 \\ 0 & \gamma p_0 & 0 & u_0 \end{bmatrix} \quad (2.25)$$

$$B_0 = \begin{bmatrix} v_0 & 0 & \rho_0 & 0 \\ 0 & v_0 & 0 & 0 \\ 0 & 0 & v_0 & \frac{1}{\rho_0} \\ 0 & 0 & \gamma p_0 & v_0 \end{bmatrix} \quad (2.26)$$

2.3 Equations in General Curvilinear Coordinates

2.3.1 Three-Dimensional Equations

For a general curvilinear coordinate transformation in three-dimension, we have

$$\xi = \xi(x, y, z)$$

$$\eta = \eta(x, y, z)$$

$$\zeta = \zeta(x, y, z)$$

If the general curvilinear coordinate transformation is introduced into the equation (2.20), and the Cartesian variable vector $\vec{q} = (\rho, u, v, w, p)$ is retained as the dependent variable vector, we have

$$\frac{\partial \vec{q}}{\partial t} + \tilde{A}_0 \frac{\partial \vec{q}}{\partial \xi} + \tilde{B}_0 \frac{\partial \vec{q}}{\partial \eta} + \tilde{C}_0 \frac{\partial \vec{q}}{\partial \zeta} = \vec{S} \quad (2.27)$$

where

$$\tilde{A}_0 = A_0 \xi_x + B_0 \xi_y + C_0 \xi_z \quad (2.28)$$

$$\tilde{B}_0 = A_0 \eta_x + B_0 \eta_y + C_0 \eta_z \quad (2.29)$$

$$\tilde{C}_0 = A_0 \zeta_x + B_0 \zeta_y + C_0 \zeta_z \quad (2.30)$$

and the Jacobian matrices, \tilde{A}_0 , \tilde{B}_0 and \tilde{C}_0 , are

$$\tilde{A}_0, \tilde{B}_0, \text{ or } \tilde{C}_0 = \begin{bmatrix} \theta_0 & \rho_0 k_x & \rho_0 k_y & \rho_0 k_z & 0 \\ 0 & \theta_0 & 0 & 0 & \frac{k_x}{\rho_0} \\ 0 & 0 & \theta_0 & 0 & \frac{k_y}{\rho_0} \\ 0 & 0 & 0 & \theta_0 & \frac{k_z}{\rho_0} \\ 0 & \gamma p_0 k_x & \gamma p_0 k_y & \gamma p_0 k_z & \theta_0 \end{bmatrix} \quad (2.31)$$

where

$$\theta_0 = u_0 k_x + v_0 k_y + w_0 k_z,$$

with $k = \xi$ for \tilde{A}_0 , $k = \eta$ for \tilde{B}_0 and $k = \zeta$ for \tilde{C}_0 . The Jacobian matrices \tilde{A}_0 , \tilde{B}_0 and \tilde{C}_0 have a set of eigenvalues and a complete distinct set of eigenvectors which are related to the propagation of vorticity, entropy and acoustic waves. Therefore, similarity transformations can be used to diagonalize \tilde{A}_0 , \tilde{B}_0 and \tilde{C}_0 , so that

$$\tilde{A}_0 = T_\xi \Lambda_\xi T_\xi^{-1}$$

$$\tilde{B}_0 = T_\eta \Lambda_\eta T_\eta^{-1}$$

$$\tilde{C}_0 = T_\zeta \Lambda_\zeta T_\zeta^{-1}$$

where

$$\Lambda_\xi = \text{Diag}(\tilde{u}_0, \tilde{u}_0, \tilde{u}_0, \tilde{u}_0 + c_0 \sqrt{\xi_x^2 + \xi_y^2 + \xi_z^2}, \tilde{u}_0 - c_0 \sqrt{\xi_x^2 + \xi_y^2 + \xi_z^2}) \quad (2.32)$$

$$\Lambda_\eta = \text{Diag}(\tilde{v}_0, \tilde{v}_0, \tilde{v}_0, \tilde{v}_0 + c_0 \sqrt{\eta_x^2 + \eta_y^2 + \eta_z^2}, \tilde{v}_0 - c_0 \sqrt{\eta_x^2 + \eta_y^2 + \eta_z^2}) \quad (2.33)$$

$$\Lambda_\zeta = \text{Diag}(\tilde{w}_0, \tilde{w}_0, \tilde{w}_0, \tilde{w}_0 + c_0 \sqrt{\zeta_x^2 + \zeta_y^2 + \zeta_z^2}, \tilde{w}_0 - c_0 \sqrt{\zeta_x^2 + \zeta_y^2 + \zeta_z^2}) \quad (2.34)$$

$$\tilde{u}_0 = u_0 \xi_x + v_0 \xi_y + w_0 \xi_z$$

$$\tilde{v}_0 = u_0 \eta_x + v_0 \eta_y + w_0 \eta_z$$

$$\tilde{w}_0 = u_0 \zeta_x + v_0 \zeta_y + w_0 \zeta_z$$

$\text{Diag}(\lambda_1, \lambda_1, \lambda_1, \lambda_2, \lambda_3)$ is a diagonal matrix with $\lambda_1, \lambda_1, \lambda_1, \lambda_2$ and λ_3 as its five diago-

nal elements respectively. c_0 is the speed of sound which can be evaluated from the expression $c_0^2 = \gamma p_0 / \rho_0$. T_k and Λ_k with $k = \zeta, \eta, \zeta$ are referred as eigenvector matrices and eigenvalue matrices, because they consists of the set of eigenvectors and eigenvalues respectively. The eigenvector matrices and their inverse matrices can be written as the following:

$$T_k = \begin{bmatrix} \tilde{k}_x & \tilde{k}_y & \tilde{k}_z & \frac{\rho_0}{\sqrt{2}c_0} & \frac{\rho_0}{\sqrt{2}c_0} \\ 0 & -\tilde{k}_z & \tilde{k}_y & \frac{\tilde{k}_x}{\sqrt{2}} & -\frac{\tilde{k}_x}{\sqrt{2}} \\ \tilde{k}_z & 0 & -\tilde{k}_x & \frac{\tilde{k}_y}{\sqrt{2}} & -\frac{\tilde{k}_y}{\sqrt{2}} \\ -\tilde{k}_y & \tilde{k}_x & 0 & \frac{\tilde{k}_z}{\sqrt{2}} & -\frac{\tilde{k}_z}{\sqrt{2}} \\ 0 & 0 & 0 & \frac{\rho_0 c_0}{\sqrt{2}} & \frac{\rho_0 c_0}{\sqrt{2}} \end{bmatrix} \quad (2.35)$$

$$T_k^{-1} = \begin{bmatrix} \tilde{k}_x & 0 & \tilde{k}_z & -\tilde{k}_y & -\frac{\tilde{k}_x}{c_0^2} \\ \tilde{k}_y & -\tilde{k}_z & 0 & \tilde{k}_x & -\frac{\tilde{k}_y}{c_0^2} \\ \tilde{k}_z & \tilde{k}_y & -\tilde{k}_x & 0 & -\frac{\tilde{k}_z}{c_0^2} \\ 0 & \frac{\tilde{k}_x}{\sqrt{2}} & \frac{\tilde{k}_y}{\sqrt{2}} & \frac{\tilde{k}_z}{\sqrt{2}} & \frac{1}{\sqrt{2}\rho_0 c_0} \\ 0 & -\frac{\tilde{k}_x}{\sqrt{2}} & -\frac{\tilde{k}_y}{\sqrt{2}} & -\frac{\tilde{k}_z}{\sqrt{2}} & \frac{1}{\sqrt{2}\rho_0 c_0} \end{bmatrix} \quad (2.36)$$

where

$$\tilde{k}_x = \frac{k_x}{\sqrt{k_x^2 + k_y^2 + k_z^2}}, \tilde{k}_y = \frac{k_y}{\sqrt{k_x^2 + k_y^2 + k_z^2}}, \tilde{k}_z = \frac{k_z}{\sqrt{k_x^2 + k_y^2 + k_z^2}} \quad (2.37)$$

The eigenvalues of the Jacobian matrices determine the direction of propagation of waves. For positive value of \tilde{u}_0 in the matrix \tilde{A}_0 , for example, we can roughly say that the eigenvectors corresponding to \tilde{u}_0 are propagating in the direction along which ξ -axis is increasing. In another word, the eigenvectors are propagating in positive ξ direction. Upwind schemes use different stencil points for wave propagating in different directions. In the numerical methods shown in next chapter, the Jacobian matrices, \tilde{A}_0, \tilde{B}_0 and \tilde{C}_0 , are split into two matrices. One has only non-positive eigenvalues and the other has only non-negative eigenvalues. Therefore the following matrix is needed in the matrix splitting:

$$T_k \Lambda T_k^{-1} = \begin{bmatrix} \lambda_1 & \frac{\rho_0 \tilde{k}_x}{2c_0} \alpha & \frac{\rho_0 \tilde{k}_y}{2c_0} \alpha & \frac{\rho_0 \tilde{k}_z}{2c_0} \alpha & \frac{1}{2c_0^2} \beta \\ 0 & \frac{\tilde{k}_x^2}{2} \beta + \lambda_1 & \frac{\tilde{k}_x \tilde{k}_y}{2} \beta & \frac{\tilde{k}_x \tilde{k}_z}{2} \beta & \frac{\tilde{k}_x}{2\rho_0 c_0} \alpha \\ 0 & \frac{\tilde{k}_x \tilde{k}_y}{2} \beta & \frac{\tilde{k}_y^2}{2} \beta + \lambda_1 & \frac{\tilde{k}_y \tilde{k}_z}{2} \beta & \frac{\tilde{k}_y}{2\rho_0 c_0} \alpha \\ 0 & \frac{\tilde{k}_x \tilde{k}_z}{2} \beta & \frac{\tilde{k}_y \tilde{k}_z}{2} \beta & \frac{\tilde{k}_z^2}{2} \beta + \lambda_1 & \frac{\tilde{k}_z}{2\rho_0 c_0} \alpha \\ 0 & \frac{\rho_0 c_0 \tilde{k}_x}{2} \alpha & \frac{\rho_0 c_0 \tilde{k}_y}{2} \alpha & \frac{\rho_0 c_0 \tilde{k}_z}{2} \alpha & \frac{1}{2}(\lambda_2 + \lambda_3) \end{bmatrix} \quad (2.38)$$

where

$$\Lambda = \text{Diag}(\lambda_1, \lambda_1, \lambda_1, \lambda_2, \lambda_3) \quad , \quad \alpha = \lambda_2 - \lambda_3 \quad \text{and} \quad \beta = \lambda_2 + \lambda_3 - 2\lambda_1 .$$

2.3.2 Two-Dimensional Equations

With a general curvilinear coordinate transformation in two-dimension

$$\xi = \xi(x, y)$$

$$\eta = \eta(x, y)$$

we have

$$\frac{\partial}{\partial t} \vec{q} + \tilde{A}_0 \frac{\partial}{\partial \xi} \vec{q} + \tilde{B}_0 \frac{\partial}{\partial \eta} \vec{q} = \vec{S} \quad (2.39)$$

$$\tilde{A}_0 = A_0 \xi_x + B_0 \xi_y \quad (2.40)$$

$$\tilde{B}_0 = A_0 \eta_x + B_0 \eta_y \quad (2.41)$$

and the Jacobian matrices, \tilde{A}_0 and \tilde{B}_0 , are

$$\tilde{A}_0 \text{ or } \tilde{B}_0 = \begin{bmatrix} \theta_0 & \rho_0 k_x & \rho_0 k_y & 0 \\ 0 & \theta_0 & 0 & \frac{k_x}{\rho_0} \\ 0 & 0 & \theta_0 & \frac{k_y}{\rho_0} \\ 0 & k_x \gamma p_0 & k_y \gamma p_0 & \theta_0 \end{bmatrix} \quad (2.42)$$

with $k = \xi$ for \tilde{A}_0 and $k = \eta$ for \tilde{B}_0 . Where $\theta_0 = u_0 k_x + v_0 k_y$. The Jacobian matrices \tilde{A}_0 and \tilde{B}_0 also have a set of eigenvalues and a complete distinct set of eigenvectors which are related to the propagation of entropy, vorticity and acoustic waves. \tilde{A}_0 and \tilde{B}_0 can be diagonalized and written as:

$$\tilde{A}_0 = T_\xi \Lambda_\xi T_\xi^{-1}$$

$$\tilde{B}_0 = T_\eta \Lambda_\eta T_\eta^{-1}$$

where

$$\Lambda_\xi = \text{Diag}(\tilde{u}_0, \tilde{u}_0, \tilde{u}_0 + c_0 \sqrt{\xi_x^2 + \xi_y^2}, \tilde{u}_0 - c_0 \sqrt{\xi_x^2 + \xi_y^2}) \quad (2.43)$$

$$\Lambda_\eta = \text{Diag}(\tilde{v}_0, \tilde{v}_0, \tilde{v}_0 + c_0 \sqrt{\eta_x^2 + \eta_y^2}, \tilde{v}_0 - c_0 \sqrt{\eta_x^2 + \eta_y^2}) \quad (2.44)$$

$$\tilde{u}_0 = u_0 \xi_x + v_0 \xi_y$$

$$\tilde{v}_0 = u_0 \eta_x + v_0 \eta_y$$

$$T_k = \begin{bmatrix} 1 & 0 & \frac{\rho_0}{\sqrt{2}c_0} & \frac{\rho_0}{\sqrt{2}c_0} \\ 0 & \tilde{k}_y & \frac{\tilde{k}_x}{\sqrt{2}} & -\frac{\tilde{k}_x}{\sqrt{2}} \\ 0 & -\tilde{k}_x & \frac{\tilde{k}_y}{\sqrt{2}} & -\frac{\tilde{k}_y}{\sqrt{2}} \\ 0 & 0 & \frac{\rho_0 c_0}{\sqrt{2}} & \frac{\rho_0 c_0}{\sqrt{2}} \end{bmatrix} \quad (2.45)$$

$$T_k^{-1} = \begin{bmatrix} 1 & 0 & 0 & -\frac{1}{c_0} \\ 0 & \tilde{k}_y & -\tilde{k}_x & 0 \\ 0 & \frac{\tilde{k}_x}{\sqrt{2}} & \frac{\tilde{k}_y}{\sqrt{2}} & \frac{1}{\sqrt{2}\rho_0 c_0} \\ 0 & -\frac{\tilde{k}_x}{\sqrt{2}} & -\frac{\tilde{k}_y}{\sqrt{2}} & \frac{1}{\sqrt{2}\rho_0 c_0} \end{bmatrix} \quad (2.46)$$

with

$$\tilde{k}_x = \frac{k_x}{\sqrt{k_x^2 + k_y^2}}, \tilde{k}_y = \frac{k_y}{\sqrt{k_x^2 + k_y^2}} \quad (2.47)$$

By the same argument as in the three-dimension, we need to obtain the matrix $T_k \Lambda T_k^{-1}$ with the diagonal matrix $\Lambda = \text{Diag}(\lambda_1, \lambda_1, \lambda_2, \lambda_3)$. The manipulation of the matrix multiplication shows that

$$T_k \Lambda T_k^{-1} = \begin{bmatrix} \lambda_1 & \frac{\rho_0 \tilde{k}_x}{2c_0} \alpha & \frac{\rho_0 \tilde{k}_y}{2c_0} \alpha & \frac{1}{2c_0^2} \beta \\ 0 & \frac{\tilde{k}_x^2}{2} \beta + \lambda_1 & \frac{\tilde{k}_x \tilde{k}_y}{2} \beta & \frac{\tilde{k}_x}{2\rho_0 c_0} \alpha \\ 0 & \frac{\tilde{k}_x \tilde{k}_y}{2} \beta & \frac{\tilde{k}_y^2}{2} \beta + \lambda_1 & \frac{\tilde{k}_y}{2\rho_0 c_0} \alpha \\ 0 & \frac{\rho_0 c_0 \tilde{k}_x}{2} \alpha & \frac{\rho_0 c_0 \tilde{k}_y}{2} \alpha & \frac{1}{2}(\lambda_2 + \lambda_3) \end{bmatrix} \quad (2.48)$$

where α and β are defined as in three-dimension.

2.4 Wave Decomposition

To illustrate that the Jacobian matrices have a set of complete distinct set of eigenvectors which are related to the propagation of waves, we consider acoustic field equation in a uniform flow in one-dimension, which can be written as:

$$\frac{\partial \vec{q}}{\partial t} + A_0 \frac{\partial \vec{q}}{\partial x} = 0 \quad (2.49)$$

where wave vector $\vec{q} = (\rho, u, p)$. The Jacobian matrix is

$$A_0 = \begin{bmatrix} u_0 & \rho_0 & 0 \\ 0 & u_0 & \frac{1}{\rho_0} \\ 0 & r p & u_0 \end{bmatrix}$$

and it can be diagonalized as

$$A_0 = T \Lambda T^{-1} = \begin{bmatrix} 1 & \frac{\rho_0}{\sqrt{2}c_0} & \frac{\rho_0}{\sqrt{2}c_0} \\ 0 & \frac{1}{\sqrt{2}} & -\frac{1}{\sqrt{2}} \\ 0 & \frac{\rho_0}{\sqrt{2}c_0} & \frac{\rho_0}{\sqrt{2}c_0} \end{bmatrix} \begin{bmatrix} u_0 & 0 & 0 \\ 0 & u_0 + c_0 & 0 \\ 0 & 0 & u_0 - c_0 \end{bmatrix} \begin{bmatrix} 1 & 0 & -\frac{1}{c_0^2} \\ 0 & \frac{1}{\sqrt{2}} & \frac{1}{\sqrt{2}\rho_0 c_0} \\ 0 & -\frac{1}{\sqrt{2}} & \frac{1}{\sqrt{2}\rho_0 c_0} \end{bmatrix}$$

It is seen that the matrix T contains three independent eigenvectors of the Jacobian matrix A_0 . Denote these three eigenvectors as χ_1, χ_2 and χ_3 respectively. We can then project the disturbance vector \vec{q} on these three independent eigenvectors and write the disturbance vector as $\vec{q} = s_1 \chi_1 + s_2 \chi_2 + s_3 \chi_3$, where s_1, s_2 and s_3 are the three projections in the three directions. Substituting the above expression into equation (2.49) and using the property of eigenvectors, we obtain

$$\begin{aligned} & \frac{\partial}{\partial t}(s_1 \chi_1) + u_0 \frac{\partial}{\partial x}(s_1 \chi_1) + \\ & \frac{\partial}{\partial t}(s_2 \chi_2) + (u_0 + c_0) \frac{\partial}{\partial x}(s_2 \chi_2) + \\ & \frac{\partial}{\partial t}(s_3 \chi_3) + (u_0 - c_0) \frac{\partial}{\partial x}(s_3 \chi_3) = 0 \end{aligned} \quad (2.50)$$

Therefore the disturbance vector can be decomposed into three vectors which are propagating with speeds of u_0 , $u_0 + c_0$ and $u_0 - c_0$ respectively. Note that χ_1 is traveling along with the flow and has no contributions to pressure disturbance p , which is referred as entropy wave. χ_2 and χ_3 are propagating with the relative speeds of sound to the flow and they have influences on the pressure disturbances, which are known as acoustic waves. Similar analogy can be applied to the eigenvalues and eigenvectors of the Jacobian matrices in multi-dimension. The disturbance waves in the multi-dimension can be decomposed into different waves, namely entropy, vorticity and acoustic waves. The entropy and vorticity waves are propagating with the flow and have no effects on the pressure disturbance, while the acoustic waves are propagating with the relative speeds of sound to the flow. The contributions to the pressure disturbances are only from the last two columns of T_k in equation (2.35) in three-dimension and equation (2.45) in two-dimension, which implies that pressure disturbances are only affected by the acoustic waves.

3 OPTIMIZED UPWIND SCHEMES

In this chapter, we start from one-dimensional scalar model wave equation with a constant propagating speed. The basic properties of the model wave equation, the Fourier transform, the traditional finite different approach and the newly developed Dispersion-Relation-Preserving (DRP) (Tam and Webb, 1993) on the model wave equation are briefly reviewed. The optimized upwind spatial discretizations are introduced and developed on one-dimensional uniform grid first. The generalization and extension of the spatial discretizations to the multi-dimensional uniform grids are derived subsequently. Finally time integration and boundary conditions are discussed.

3.1 Model Wave Equation

Consider the scalar model wave equation

$$\frac{\partial u}{\partial t} + c \frac{\partial u}{\partial x} = 0 \quad (3.1)$$

with the initial distribution

$$u(x, 0) = u_0(x) \quad (3.2)$$

where c is the propagating speed of the wave and $u = u(x, t)$. Without the loss of generality, we assume that $c > 0$. The solution for the above initial value problem of the equations (3.1) and (3.2) can be easily obtained and written as the following

$$u(x, t) = u_0(x - ct)$$

or

$$u(x + ct, t) = u_0(x)$$

which simply implies that the solution at point (x, t) is the initial value at $x - ct$. In another word, the solution is a right traveling wave. For example, consider a “snapshot” of the solution taken at t_0 . After time of interval Δt has passed, the wave solution has moved to the right (in the positive x-axis direction) by $c\Delta t$.

Consider the Fourier transform of the solution $u(x, t)$ and its inverse transform:

$$\tilde{u}(\alpha, t) = \frac{1}{2\pi} \int_{-\infty}^{\infty} u(x, t) e^{-i\alpha x} dx \quad (3.3)$$

$$u(x, t) = \int_{-\infty}^{\infty} \tilde{u}(\alpha, t) e^{i\alpha x} d\alpha \quad (3.4)$$

where $i = \sqrt{-1}$ and α is the wavenumber. Application of Fourier transform requires some limitation on the solution $u(x, t)$, e.g. $u(x, t)$ is absolutely integrable. We assume that Fourier transform is always applicable on the solution. The Fourier inverse transform indicates that the solution $u(x, t)$ can be decomposed into the infinite sum of simple harmonic waves. Applying the Fourier transform to the initial value problems of equations (3.1) and (3.2), we have

$$\frac{d}{dt} \tilde{u}(\alpha, t) + ic\alpha \tilde{u}(\alpha, t) = 0 \quad (3.5)$$

$$\tilde{u}(\alpha, 0) = \tilde{u}_0(\alpha) \quad (3.6)$$

where

$$\tilde{u}_0(\alpha) = \frac{1}{2\pi} \int_{-\infty}^{\infty} u_0(x) e^{-i\alpha x} dx.$$

Solving equation (3.5), we obtain:

$$\begin{aligned} \tilde{u}(\alpha, t) &= \tilde{u}_0(\alpha) e^{-ic\alpha t} \\ u(x, t) &= \int_{-\infty}^{\infty} \tilde{u}_0(\alpha) e^{i\alpha(x-ct)} d\alpha \end{aligned} \quad (3.7)$$

Therefore the solution of initial value problem of equations (3.1) and (3.2) is the sum of sinusoidal-traveling-waves with various wavenumbers. The expression (3.7) also indicates that all the sinusoidal-traveling-waves are propagating to the right with the speed c . As a matter of fact, for scalar linear wave equation, the behavior of the solution can be understood and studied through the fundamental solution of the sinusoidal-traveling-waves in the following form:

$$\varphi(x, t) = e^{i(\alpha x - \omega t)} \quad (3.8)$$

where ω is the angular frequency. Denote $\phi = \alpha x - \omega t$ which is referred as the phase. Substituting equation (3.8) into equation (3.1), we obtain

$$\omega = c\alpha \quad (3.9)$$

This is the dispersion relation for the one-dimensional scalar wave equations (3.1). It states that for a wave with a given wavenumber α , its frequency ω is determined by the dispersion relation. On the other hand, we may say that for a wave with a given frequency ω , its wavenumber is determined by the dispersion relation. In general, for an arbitrary

scale wave equation, to satisfy the wave equation, the wavenumber α and the angular frequency ω are related through an equation which can be formally written as the following:

$$G(\omega, \alpha) = 0 \quad (3.10)$$

The relation between ω and α through the above equation is called the dispersion relation of the wave equation. The wave phase velocity is defined as $v_p = \omega/\alpha$ which is the propagating velocity of the surface at which the phase does not change, i.e. ϕ is a constant. If angular frequency can be further expressed explicitly as a function of the wavenumber, i.e. $\omega = \omega(\alpha)$, the wave group velocity can be introduced and defined as $v_g = d\omega/d\alpha$ which is the propagating velocity of different wavenumbers. For the one-dimensional scalar wave equations (3.1), $v_p = v_g = c$. The wave phase velocity and wave group velocity are the same constant regardless of wavenumbers. Although an initial arbitrary wave may consist of the sinusoidal-traveling-waves with different wavenumbers, its waveshape and its magnitude remain unchanged after arbitrarily large propagating distance. Therefore the model equation (3.1) is dispersionless and dissipationless.

For the system of wave equations in multi-dimension, equation (2.20), for example, the behaviors of the solutions of the system can also be understood and studied through the fundamental solution of the sinusoidal-traveling-waves. Denote $\vec{X} = (x, y, z)$ and $\vec{\alpha} = (\alpha_1, \alpha_2, \alpha_3)$. The the fundamental solution can be written as

$$\vec{\Phi}(\vec{X}, t) = \vec{R} e^{i(\vec{\alpha} \cdot \vec{X} - \omega t)} \quad (3.11)$$

where \vec{R} is a constant vector. By the same argument as that for the one-dimensional scalar wave equation, the $\vec{\alpha}$ and ω are related through the equation

$$\vec{G}(\omega, \vec{\alpha}) = 0 \quad (3.12)$$

The relation between ω and $\vec{\alpha}$ through the above equation is called the dispersion relation of the system. The phase velocity is now defined as

$$\vec{V}_p = \frac{\omega}{|\vec{\alpha}|^2} \vec{\alpha}$$

which is in the same direction as $\vec{\alpha}$. This is because the surface with specific phase ϕ_0 is given by

$$\vec{\alpha} \cdot \vec{X} - \omega t = \phi_0$$

the normal vector of the surface is just $\vec{\alpha}$ and the phase velocity is in the same direction as the normal.

3.2 Optimized Upwind Spatial Discretizations

Finite difference schemes discretize partial differential equations by approximating and replacing partial differential derivatives with finite differences. The discretizations result in algebraic equations which can then be solved by various well-developed numerical methods. The algebraic equations resulted from the discretizations should be consistent with the original differential equations and their solutions should be stable and converge to the solutions of the differential equations. In another word, the solutions of the algebraic equations approach the solution of the differential equations when the grid sizes and time steps are approaching to zero. There are basically two ways to discretize the differential equations. One is to treat spatial and temporal derivatives in the differential equa-

tions separately. In this approach, the discretizations of spatial derivatives result in a system of semi-discrete ordinary partial differential equations in which the temporal derivatives can then be further discretized by either well-developed methods such as Runge-Kutta methods and multi-stages methods or by optimized time discretizations. The second approach is to approximate the spatial and temporal derivatives simultaneously. No intermediate semi-discrete forms are produced. Classical Lax-Wendroff and MacCormack finite difference schemes belong to the second category. In this thesis, the optimized upwind schemes following the first approach only are studied and developed.

Refer to the scalar model wave equation (3.1). Consider the approximation of the first order spatial derivative $\partial u / \partial x$ by a finite difference on a uniform grid of spacing Δx

$$\left(\frac{\partial u}{\partial x}\right)_l \approx \frac{1}{\Delta x} \sum_{j=-N}^M a_j u_{l+j} \quad (3.13)$$

where $u_{l+j} = u((l+j)\Delta x, t)$, $\left(\frac{\partial u}{\partial x}\right)_l = \frac{\partial u}{\partial x}(l\Delta x, t)$ and a_j is coefficient needed to be determined according to required order of accuracy and other properties. l is an integer representing grid node. For a pure initial value problem, l can be any integer. In real computation, however, it requires finite computational domain. Therefore l must have lower and upper bound. The finite difference approximation (3.13) requires M stencils of u to the right and N stencils of u to the left of the node l . Substituting (3.13) into the model wave equation (3.1), we obtain a system of semi-discrete ordinary differential equations which can be written as the following:

$$\left(\frac{du}{dt}\right)_l + \frac{c}{\Delta x} \sum_{j=-N}^M a_j u_{l+j} = 0 \quad (3.14)$$

Consider the fundamental solution with a given wavenumber α in the form of

$$\varphi_s(l\Delta x, t) = e^{i(\alpha l\Delta x - \omega t)} \quad (3.15)$$

where subscript s stands for semi-discrete to distinguish the fundamental solution of the one-dimensional scalar wave equation (3.1). Substituting equation (3.15) into the semi-discrete equation (3.14), we have

$$e^{i(\alpha l\Delta x - \omega t)} \left(-i\omega + \frac{c}{\Delta x} \sum_{j=-N}^M a_j e^{i\alpha j\Delta x} \right) = 0 \quad (3.16)$$

Denote

$$\bar{\alpha} = -\frac{i}{\Delta x} \sum_{j=-N}^M a_j e^{i\alpha j\Delta x} \quad (3.17)$$

then equation (3.16) gives the dispersion relation of the semi-discrete equation (3.14) as the following:

$$\omega = c\bar{\alpha} \quad (3.18)$$

It is observed that equation (3.18) is identical to the dispersion relation in equation (3.9), if $\bar{\alpha}$ is replaced by α . By the analysis similar to the derivation of the solution for the one-dimensional scalar wave equation (3.1) with the Fourier transform, it is necessary that $\bar{\alpha}$ approximates α accurately for relative broad wavenumbers to assure that the solution of the semi-discrete equation (3.14) can be a good approximation to the solution of the wave equation (3.1). $\bar{\alpha}$ is called the effective numerical wavenumber of the finite difference

scheme (3.13). For fixed spacing Δx , $\bar{\alpha}$ is a periodic function of α . The spacing Δx depends on the range of wavenumber which needs to be resolved in the real computation. For example, if the scheme is being used to resolve the waves with the wave length longer than $4\Delta x$, in another word, using four grid points per wavelength (PPW), $\frac{2\pi}{\alpha} \geq 4\Delta x$ or $\alpha\Delta x \leq \frac{\pi}{2}$. Therefore, it is convenient to consider $\alpha\Delta x$ together as a variable. From (3.17), it is seen that $\bar{\alpha}\Delta x$ is now a periodic function of $\alpha\Delta x$ with 2π as the period.

Since $\bar{\alpha}$ can be a complex number, $\bar{\alpha} = \bar{\alpha}_r + i\bar{\alpha}_i$, where $\bar{\alpha}_r$ and $\bar{\alpha}_i$ are the real and imaginary parts of $\bar{\alpha}$ respectively. From the dispersion relation (3.18), we can write the fundamental solution with a given wavenumber α for the semi-discrete equation (3.14) as

$$\varphi_s(l\Delta x, t) = e^{i(\alpha l\Delta x - c\bar{\alpha}t)} = e^{i\alpha[l\Delta x - c(\bar{\alpha}_r/\alpha)t]} e^{c\bar{\alpha}_i t} \quad (3.19)$$

The wave phase velocity $v_p = c(\bar{\alpha}_r/\alpha)$ is not the constant c , unless $\bar{\alpha}_r = \alpha$ which is not realistic in a computation. v_p depends on the wavenumber α . Waves with different wavenumbers are propagating with different speeds. Therefore for an initial arbitrary wave which may consist of the sinusoidal-traveling-waves with different wavenumbers, its waveshape is no longer able to remain unchanged. This phenomena is called dispersion. Note that if $\bar{\alpha}_i \neq 0$, in addition to travelling with different speeds, waves with different wavenumbers are now growing or diminishing with different factors. From the expression (3.19), if there exists a wavenumber so that $c\bar{\alpha}_i > 0$, the magnitude of the wave corresponding to the wavenumber α increases without an upper bound as time increases. The numerical solution is unstable and the discretization is referred as unstable. If $c\bar{\alpha}_i < 0$ for all wavenumbers, the magnitude of the solution has a upper bound as time increases. The discretization is, therefore, referred as stable. The phenomena that the magnitude of a

wave grows and diminishes as it travels is called dissipation. Therefore, contrast to the dispersionless and dissipationless one-dimensional scalar wave equation (3.1), the semi-discrete equation (3.14) is dispersive and dissipative if $\bar{\alpha}_r \neq \alpha$ and $\bar{\alpha}_i \neq 0$. Comparing fundamental solutions (3.19) and (3.8), we have

$$\frac{\varphi_s(l\Delta x, t)}{\varphi(l\Delta x, t)} = e^{ic(\alpha - \bar{\alpha}_r)t} e^{c\bar{\alpha}_i t} \quad (3.20)$$

Therefore the phase and magnitude errors introduced by the approximation of the one-dimensional scalar wave equation (3.1) with the semi-discrete equation (3.14) are respectively as;

$$|\phi_s(t) - \phi(t)| = |c(\alpha - \bar{\alpha}_r)t|$$

$$G(t) = e^{c\bar{\alpha}_i t}$$

where ϕ represents the phase and $G(t)$ is known as the amplification factor. If the amplification factor has upper bound for all t , the numerical discretization is stable. For the equation (3.14), it is easy to see the sufficient and necessary condition for the stability is $c\bar{\alpha}_i \leq 0$.

There are many ways to construct the coefficients in the finite difference approximation (3.13) based on different criterions with which the wavenumber α is approximated by the effective numerical wavenumber $\bar{\alpha}$. Traditionally the coefficients are constructed solely based on the order of accuracy of the truncation errors in the right hand side of (3.13) or equivalently the right hand side of (3.17). Using Taylor expansion, we have

$$e^{i\alpha j\Delta x} = 1 + i\alpha j\Delta x + \frac{(i\alpha j\Delta x)^2}{2!} + \frac{(i\alpha j\Delta x)^3}{3!} + \dots \quad (3.21)$$

Substituting the above expansion into the expression of the effective numerical wavenumber (3.17), we obtain

$$\bar{\alpha} = -\frac{i}{\Delta x} \sum_{j=-N}^M \left[a_j + (i\alpha\Delta x)(a_j j) + \frac{(i\alpha\Delta x)^2}{2!}(a_j j^2) + \frac{(i\alpha\Delta x)^3}{2!}(a_j j^3) + \dots \right] \quad (3.22)$$

If we let

$$\sum_{j=-N}^M a_j = 0 \quad (3.23)$$

$$\sum_{j=-N}^M a_j j = 1 \quad (3.24)$$

$$\sum_{j=-N}^M a_j j^k = 0 \quad (3.25)$$

for $k = 2, 3, \dots, N + M$, there are $N + M + 1$ linear algebraic equations given in equations (3.23), (3.24) and (3.25) with $N + M + 1$ unknowns $a_j, j = -N, -N + 1, \dots, M$. The unique solution of the equations will determine the coefficients a_j of the finite difference approximation (3.13). Using these equations and equation (3.22) we can write effective numerical wavenumber as

$$\bar{\alpha} = \alpha + O(\alpha\Delta x)^{N+M} \quad (3.26)$$

From another point of view without employing the concept of wavenumber, we can expand u_{l+j} in the finite difference (3.13) at node l , i.e. the point $l\Delta x$, using Taylor series

as the following

$$u_{l+j} = u_l + \left(\frac{\partial u}{\partial x}\right)_l (j\Delta x) + \left(\frac{\partial^2 u}{\partial x^2}\right)_l \frac{(j\Delta x)^2}{2!} + \left(\frac{\partial^3 u}{\partial x^3}\right)_l \frac{(j\Delta x)^3}{3!} + \dots \quad (3.27)$$

Substituting the above expansion into the finite difference (3.13) and using algebraic equations given in equations (3.23), (3.24) and (3.25), we have

$$\begin{aligned} \frac{1}{\Delta x} \sum_{j=-N}^M a_j u_{l+j} &= \\ \frac{1}{\Delta x} \sum_{j=-N}^M \left(u_l a_j + \Delta x \left(\frac{\partial u}{\partial x}\right)_l (a_j j) + \frac{(\Delta x)^2}{2!} \left(\frac{\partial^2 u}{\partial x^2}\right)_l (a_j j^2) + \frac{(\Delta x)^3}{3!} \left(\frac{\partial^3 u}{\partial x^3}\right)_l (a_j j^3) + \dots \right) \\ &= \left(\frac{\partial u}{\partial x}\right)_l + O(\Delta x)^{N+M} \end{aligned}$$

where the power of $N+M$ is called the order of the truncation error. The coefficient before $(\Delta x)^{N+M}$ in the truncation error depends on the $(N+M+1)$ th order of derivative of u with respect to x . The $(N+M+1)$ th order derivative of the fundamental solution with wavenumber α contains the factor of α^{N+M+1} . Therefore, these two different view points, using and without using the wavenumber, are in fact equivalent. The one with the concept of wavenumber, however, is preferred in this study because it infers how big the wavenumber can be resolved, which is quite important in dealing with the acoustic waves.

We have discussed the finite difference scheme for which the coefficients are determined purely from the standard Taylor expansions. The above procedures show that order $M+N$ of the truncation error is the maximum order which can be achieved with $N+M+1$ stencils used in the finite difference scheme. Therefore if $\alpha\Delta x$ is small, which is true either for small α (the relative long wave), or for small Δx (using a lot of grid points per

wavelength), the finite difference determined solely with standard Taylor expansions gives the highest order of accuracy. One problem with this type of differencing, however, is that the scheme quickly becomes inaccurate for relative short wave (large α) propagations or relative coarse-grid discretizations (large Δx). As it is mentioned in the introduction, acoustic waves have high frequency and broad wavenumber which demand the schemes with less PPW. It is reasonable for the scheme to use 6 PPW, in another word the scheme should be able to resolve the waves with $\alpha\Delta x \leq \pi/3$. When $\alpha\Delta x$ is not close to 0, for example, $\alpha\Delta x$ is close to $\pi/3$ for the scheme with 6 PPW, the truncation error of the scheme obtained solely with standard Taylor expansions is no longer small. To overcome this problem, Miranker in 1971 presented a variety of difference schemes derived from constrained minimization of L_2 norms of the local truncation errors for a class of hyperbolic differential equations. Due to its complexity in solving the minimization analytically, the technique apparently went relatively unnoticed until it was recently rediscovered by many authors (Liu, 1996). This technique is used for deriving so called optimized schemes including Tam and Webb's Dispersion-Relation-Preserving (DRP) schemes in which L_2 norms of truncation errors for both wavenumber in space and the frequency in time were minimized.

Instead all the coefficients in the finite difference approximation (3.13) are determined by the Taylor expansion to achieve the maximum order of truncation error, some of them are left to be free and used to minimize L_2 norms of the truncation errors of the approximation of effective numerical wavenumber $\bar{\alpha}$ to the actual wavenumber α . To demonstrate the idea, let P be an integer and $0 < P < M + N$. Utilizing equations (3.23), (3.24) and (3.25) for only $k = 2, 3, \dots, P$, i.e. the first $P+1$ equations instead of all $M+N+1$

equations, is unable to uniquely determine all the coefficients in the finite difference schemes (3.13), leaving $M+N-P$ of coefficients free. Without the loss of generality, we assume the coefficients from a_{-N} , a_{-N+1} to a_{M-P-1} are free. From equations (3.23), (3.24) and (3.25) for $k = 2, 3, \dots, P$, we can express other coefficients as the functions of the free coefficients, which can be formally written as the following

$$a_j = a_j(a_{-N}, a_{-N+1}, \dots, a_{M-P-1}), j = M-P, M-P+1, \dots, M$$

The above functions give infinite sets of coefficients in the finite difference (3.13) so that finite difference (3.13) approximates the spatial derivative $\partial u / \partial x$ with P order of accuracy in the truncation error. In term of effective numerical wavenumber, we have

$$\bar{\alpha} = \alpha + O(\alpha \Delta x)^P.$$

P is chosen to be greater or equal to one to guarantee that the finite difference approximation has at least one order of accuracy. The free coefficients can be used to minimize the following L_2 norms of the local truncation errors introduced by the approximation of the effective numerical wavenumber $\bar{\alpha}$ to the actual wavenumber α :

$$E = \int_{-\beta_0}^{\beta_0} \left\{ \lambda [\text{Re}(\bar{\beta}) - \beta]^2 + (1 - \lambda) \left[\text{Im}(\bar{\beta}) + \exp\left(-\ln 2 \left(\frac{|\beta| - \pi}{\sigma}\right)^2\right) \right]^2 \right\} d\beta \quad (3.28)$$

where $\beta = \alpha \Delta x$ and $\bar{\beta} = \bar{\alpha} \Delta x$. Re and Im represent the real and imaginary parts of a complex number respectively. β_0 is predetermined number which gives the optimized range of wavenumbers. The parameter λ is a weighting coefficient whose value is between 0 and 1. As it is discussed before, we consider $\alpha \Delta x$ instead of α as an independent variable. The first term in the expression of E in equation (3.28) minimizes the distance between $\bar{\alpha}_r \Delta x$ and $\alpha \Delta x$ in the sense of L_2 norm. The second term instead

minimizes the distance between $\bar{\alpha}_i \Delta x$ and 0, it minimizes the distance in the sense of L_2 norm between $\bar{\alpha}_i \Delta x$ and a Gaussian function, which is almost 0 when $\alpha \Delta x$ is far from π and is decreasing to -1 when $\alpha \Delta x$ approaches to π . Remember that the wave propagating speed c in the discussion is a positive number. Therefore the second term in the expression of E , which forces the imaginary part of the effective numerical wavenumber to be negative during the minimization, guarantees the stability of the scheme as it is discussed before. The Gaussian term is chosen to allow the imaginary part of the effective numerical wavenumber to be very close to zero for the waves with wavenumber within certain scope by adjusting β_0 . The second term also allows controls over short wave or high-frequency damping by adjusting parameter σ . From the expression of the effective numerical wavenumber in equation (3.17), using $e^{i\alpha j \Delta x} = \cos(j\alpha \Delta x) + i \sin(j\alpha \Delta x)$, we can write the real part and imaginary part of $\bar{\beta}$ in the following forms:

$$\text{Re}(\bar{\beta}) = \sum_{j=-N}^M a_j \sin(j\beta)$$

$$\text{Im}(\bar{\beta}) = - \sum_{j=-N}^M a_j \cos(j\beta)$$

Note $\sin(x)$ is an odd function and $\cos(x)$ is an even function. $\text{Im}(\bar{\beta})$ has same sign for both positive and negative wavenumbers. Therefore we consider E in the following form instead of (3.28):

$$\begin{aligned} E = & \lambda \int_0^{\beta_0} \left[\sum_{j=-N}^M a_j \sin(j\beta) - \beta \right]^2 d\beta \\ & + (1 - \lambda) \int_0^{\beta_0} \left[\sum_{j=-N}^M a_j \cos(j\beta) - \exp\left(-\ln 2 \left(\frac{\beta - \pi}{\sigma}\right)^2\right) \right]^2 d\beta \end{aligned} \quad (3.29)$$

The necessary conditions that E is a minimum for all the free coefficients are

$$\frac{\partial E}{\partial a_l} = 0, l = -N, -N+1, \dots, M-P-1 \quad (3.30)$$

Directly taking the derivative of E in equation (3.29) with respect to the free coefficients a_l , we obtain

$$\begin{aligned} \frac{\partial E}{\partial a_l} &= 2\lambda \int_0^{\beta_0} \left[\sum_{j=-N}^M a_j \sin(j\beta) - \beta \right] \left[\sum_{i=-N}^M \frac{\partial a_i}{\partial a_l} \sin(i\beta) \right] d\beta \\ &+ 2(1-\lambda) \int_0^{\beta_0} \left[\sum_{j=-N}^M a_j \cos(j\beta) - \exp\left(-\ln 2 \left(\frac{\beta-\pi}{\sigma}\right)^2\right) \right] \left[\sum_{i=-N}^M \frac{\partial a_i}{\partial a_l} \cos(i\beta) \right] d\beta \\ &= 2\lambda \sum_{j=-N}^M a_j \left\{ \sum_{i=-N}^M \frac{\partial a_i}{\partial a_l} \int_0^{\beta_0} [\sin(j\beta) \sin(i\beta) - \beta \sin(i\beta)] d\beta \right\} \\ &+ 2(1-\lambda) \sum_{j=-N}^M a_j \left\{ \sum_{i=-N}^M \frac{\partial a_i}{\partial a_l} \int_0^{\beta_0} [\cos(j\beta) \cos(i\beta) - \exp\left(-\ln 2 \left(\frac{\beta-\pi}{\sigma}\right)^2\right) \cos(i\beta)] d\beta \right\} \end{aligned}$$

In the above expression for the derivative of E with respect to a_l , the integrations of $\sin(j\beta) \sin(i\beta)$, $\cos(j\beta) \cos(i\beta)$ and $\beta \sin(i\beta)$ over $[0, \beta_0]$ can be analytically calculated. Numerical integration methods, however, are needed to evaluate the integration of $\exp\left(-\ln 2 \left(\frac{\beta-\pi}{\sigma}\right)^2\right) \cos(i\beta)$ over $[0, \beta_0]$. In the real practice, the trapezoidal algorithm is used to evaluate the integration. The partial derivatives of a_i over a_l appeared in the above expression for $\partial E / \partial a_l$ can be obtained by solving the following $M+N+1$ equations for $l = -N, -N+1, \dots, M-P-1$:

$$\frac{\partial a_i}{\partial a_l} = \delta_{il} \quad \text{for } i = -N, -N+1, \dots, M-P-1 \quad (3.31)$$

and

$$\sum_{j=-N}^M j^k \frac{\partial a_j}{\partial a_l} = 0 \quad \text{for } k = 0, 1, \dots, P \quad (3.32)$$

where δ_{il} is the Kronecker delta function ($\delta_{il} = 1$ if $i=l$ and $\delta_{il} = 0$ if $i \neq l$) and equation (3.32) is from equations (3.23), (3.24) and (3.25) by taking derivatives with respect to a_l . Combining the equations (3.23), (3.24), (3.25) for $k = 2, 3, \dots, P$ with equation (3.30), we can uniquely determine the coefficients of finite difference approximation (3.13) for a given order of accuracy P and parameters β_0 , λ and σ .

If $M=N$ and $a_{-j} = -a_j$, the finite difference scheme (3.13) becomes a central difference scheme. This is because it uses same number of stencils and weights in the left and right of a node. From the expression of imaginary part of $\bar{\beta}$ derived above, for a central difference scheme we have

$$\bar{\alpha}_i \Delta x = \text{Im}(\bar{\beta}) = - \sum_{j=-N}^M a_j \cos(j\beta) = a_0 - \sum_{j=1}^M (a_j \cos(j\beta) + a_{-j} \cos(-j\beta)) = a_0$$

Equation (3.23) and $a_{-j} = -a_j$ imply that $a_0 = 0$. Therefore the imaginary part of effective numerical wavenumber $\bar{\alpha}$ for a central difference scheme is zero. For the central difference scheme, the L_2 norms of the local truncation errors E in equation (3.28) should not include the imaginary part of $\bar{\beta}$. λ and σ are no longer necessary. Although the general procedure to derive the coefficients in the finite difference scheme (3.13) still applies for the central difference scheme, slightly modifications are needed. For example, since

$$\sum_{j=-N}^M a_j j^k = \sum_{j=1}^M a_j j^k [1 - (-1)^k] = 0 \quad \text{for even } k$$

the number of free coefficients are now $M-P/2$ and P is an even number. Tam and Webb

(1993) studied and developed a fourth order accurate, 7-stencil, central finite difference scheme in space with $M = N = 3$ in their DRP method for CAA. It was obtained through minimization procedures described above for a central scheme with $P = 4$ and $\beta_0 = \pi/2$. As we discussed before, the imaginary part of effective numerical wavenumber $\bar{\alpha}_i$ introduces the error in the wave magnitude. It seems in the first appearance that central difference schemes are more accurate than non-central schemes. But in reality, because of the presence of objects, discontinuities in the flow fields, computational errors etc., the effective wavenumber corresponding to very short wavenumber may have small positive imaginary part instead of zero. As it is pointed out before, this results in instability. In fact, both the real and imaginary parts in the effective numerical wavenumbers contribute to the numerical errors. The error in magnitude should be comparable to the error in phase. Therefore, in equation (3.20), if $\bar{\alpha}_i$ is in the same order of magnitude as $\alpha - \bar{\alpha}_r$, or in another word, error introduced by $\bar{\alpha}_i$ is not dominant, non-central difference schemes with negative $\bar{\alpha}_i$ enforce the stability while keeping the competitive accuracy to the central difference schemes.

Based on the above analysis it is possible for a non-central difference scheme to make $\bar{\alpha}_r - \alpha$ and $\bar{\alpha}_i$ be almost zero for a wide range of wavenumbers, while keeping $c\bar{\alpha}_i$ negative to ensure the stability. Therefore this kind of scheme is expected to automatically damp out spurious short waves while keeping the advantage of optimized scheme of using less PPW. We studied 7-stencil of finite difference scheme (3.13) with $M=2$, $N=4$ and $P=4$. This is an upwind biased scheme, because the wave is propagating to the right ($c > 0$) and the scheme uses more stencils upwind (from the left) than downwind (from the right). If $c < 0$ i.e. the wave is propagating to the left, the upwind biased scheme uses

more stencils from the right than from the left. For example, the 7-stencil of finite difference scheme (3.13) has $M=4, N=2$ in the case of $c < 0$. The coefficients of the finite difference scheme (3.13) for $c < 0$ can be directly obtained from its counterpart for $c > 0$, if the same number of P as well as the same number of stencils are used. To see this, denote a_j^{NM} for the coefficient a_j in the finite difference scheme (3.13) with index j from $-N$ to M and a_j^{MN} for those with index j from $-M$ to N . The a_j^{NM} can be interpreted as the coefficients of the finite difference scheme which uses N stencil of points from the left and M stencil of points from the right. a_j^{MN} has the similar meaning in its convention. Using the same convention for $\bar{\beta}$, note that

$$\sum_{j=-M}^N a_j^{MN} j^k = \sum_{j=-N}^M a_{-j}^{MN} (-j)^k = (-1)^k \sum_{j=-N}^M a_{-j}^{MN} j^k \quad (3.33)$$

$$\text{Re}(\bar{\beta}^{MN}) = \sum_{j=-M}^N a_j^{MN} \sin(j\beta) = \sum_{j=-N}^M a_{-j}^{MN} \sin(-j\beta) = - \sum_{j=-N}^M a_{-j}^{MN} \sin(j\beta) \quad (3.34)$$

$$\text{Im}(\bar{\beta}^{MN}) = - \sum_{j=-M}^N a_j^{MN} \cos(j\beta) = - \sum_{j=-M}^N a_{-j}^{MN} \cos(-j\beta) = - \sum_{j=-M}^N a_{-j}^{MN} \cos(j\beta) \quad (3.35)$$

If we chose

$$a_{-j}^{MN} = -a_j^{NM}$$

we obtain

$$\sum_{j=-M}^N a_j^{MN} j^k = (-1)^{k+1} \sum_{j=-N}^M a_j^{NM} j^k$$

and

$$\text{Re}(\bar{\beta}^{MN}) = \text{Re}(\bar{\beta}^{NM})$$

$$\text{Im}(\bar{\beta}^{MN}) = -\text{Im}(\bar{\beta}^{NM})$$

Therefore the scheme with coefficient a_j^{MN} has the same order of accuracy as the scheme with coefficient a_j^{NM} . The effective numerical wave number of the scheme with coefficient a_j^{MN} is the conjugate of that of the scheme with coefficient a_j^{NM} . That opposite sign in the imaginary parts of the effective wavenumbers of these two schemes are desired to ensure the stability for the waves propagating in two contrary directions, namely positive and negative x -axis directions.

Table 1 Coefficients for the 7-stencil optimized upwind schemes

$N = 4, M = 2, c > 0$		$N = 2, M = 4, c < 0$	
a_{-4}^{42}	0.016140071346698814	a_{-2}^{24}	0.041382855555706463
a_{-3}^{42}	-0.12265083451112346	a_{-1}^{24}	-0.44077420643183318
a_{-2}^{42}	0.45448643568845881	a_0^{24}	-0.50020513450976445
a_{-1}^{42}	-0.12475721579099250	a_1^{24}	0.12475721579099250
a_0^{42}	0.50020513450976445	a_2^{24}	-0.45448643568845881
a_1^{42}	0.44077420643183318	a_3^{24}	0.12265083451112346
a_2^{42}	-0.041382855555706463	a_4^{24}	-0.016140071346698814

Table 1 gives the coefficients for 7-stencil optimized upwind finite difference scheme obtained by the above described procedures with $\beta_0 = \pi/2$, $\lambda = 0.964$ and $\sigma = 0.2675\pi$. Figure 1 compares the effective numerical wavenumbers for the optimized upwind scheme ($N=4$, $M=2$, $P=4$) with coefficients given in Table 1 to other well-known schemes. It indicates that the optimized upwind scheme has much less dissipation error than those of the standard six-order accurate upwind scheme and Tam & Webb's backward DRP scheme used for grid points near boundaries. It also indicates that the optimized upwind scheme is able to resolve the waves with as high wavenumbers as those resolved by Tam & Webb's central DRP scheme. The parameter $\beta_0 = \pi/2$, $\lambda = 0.964$ and $\sigma = 0.2675\pi$ used for determining the coefficients of the optimized upwind scheme were obtained through trial and error. During the trial, a lots of combinations of β_0 , λ and σ were used. For each combination the curves as those shown in Figure 1 were plotted and compared. The coefficients with the minimum errors based on visual evaluation were then chosen. Therefore the coefficients given in the Table 1 might not be the best choice among the schemes with $N=4$, $M=2$ and $P=4$ because of trial and error.

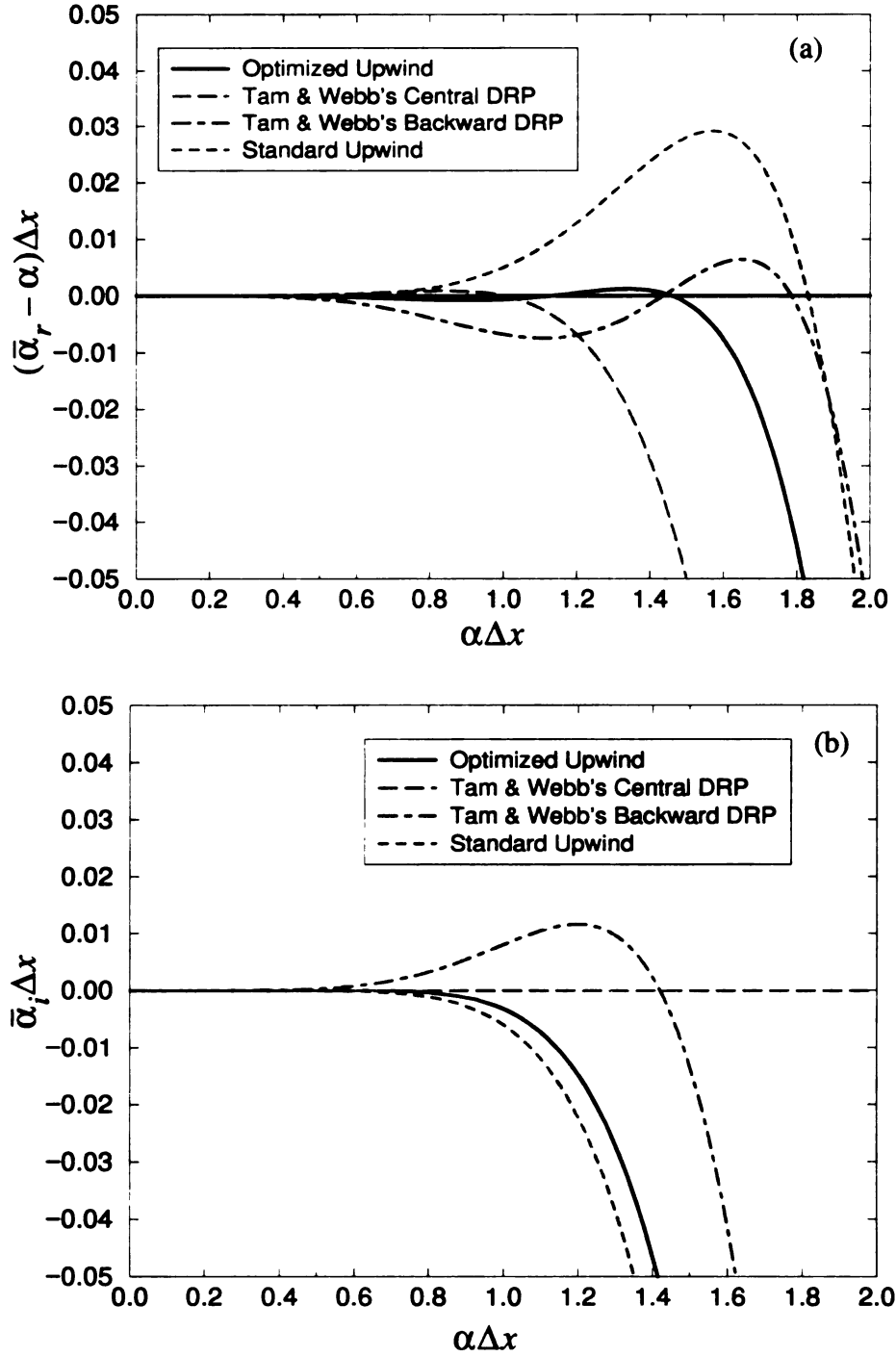


Figure 1 Real part (a) and imaginary part (b) of the effective numerical wavenumber versus actual wavenumber for 7-stencil schemes: Optimized upwind scheme ($N=4$, $M=2$, $P=4$); Tam & Webb's central DRP ($N=3$, $M=3$, $P=4$); Tam & Webb's backward DRP used near boundary ($N=4$, $M=2$, $P=4$); Standard six-order accurate upwind scheme ($N=4$, $M=2$, $P=6$)

3.3 Extension of Optimized Upwind Schemes to Acoustic Field Equations in Multi-Dimension

The acoustic field equations in general curvilinear coordinate system in three-dimension have been derived in section 2.3. Here we rewrite the acoustic field equations which are given in equation (2.27):

$$\frac{\partial \vec{q}}{\partial t} + \tilde{A}_0 \frac{\partial \vec{q}}{\partial \xi} + \tilde{B}_0 \frac{\partial \vec{q}}{\partial \eta} + \tilde{C}_0 \frac{\partial \vec{q}}{\partial \zeta} = \vec{S}$$

The Jacobian matrices \tilde{A}_0 , \tilde{B}_0 and \tilde{C}_0 can be diagonalized as

$$\tilde{A}_0 = T_\xi \Lambda_\xi T_\xi^{-1},$$

$$\tilde{B}_0 = T_\eta \Lambda_\eta T_\eta^{-1},$$

$$\tilde{C}_0 = T_\zeta \Lambda_\zeta T_\zeta^{-1}.$$

The diagonal eigenvalue matrices are given in equations (2.32), (2.33) and (2.34). T_k and T_k^{-1} with $k = \xi, \eta$ and ζ are given in equations (2.35) and (2.36). The diagonal matrices determine the directions of wave propagating. The values of the diagonal elements in the eigenvalue matrices may have different signs, which implies that the waves corresponding to different elements may travel in opposite directions. In order to apply the optimized upwind scheme which is derived from the model wave equation with a single propagating speed, we need to split the diagonal matrices into two parts. One part contains elements with only non-negative values and the other part contains elements with only non-positive values. Therefore the waves corresponding to each part can then be treated as the waves propagating along the same direction, either positive axis direction or negative axis direction. To be more specific, denote

$$\Lambda_{\xi} = \Lambda_{\xi}^{+} + \Lambda_{\xi}^{-}$$

$$\Lambda_{\eta} = \Lambda_{\eta}^{+} + \Lambda_{\eta}^{-}$$

$$\Lambda_{\zeta} = \Lambda_{\zeta}^{+} + \Lambda_{\zeta}^{-}$$

where

$$\Lambda_{\xi}^{+} = \frac{1}{2}(\Lambda_{\xi} + |\Lambda_{\xi}|) \quad \Lambda_{\xi}^{-} = \frac{1}{2}(\Lambda_{\xi} - |\Lambda_{\xi}|)$$

$$\Lambda_{\eta}^{+} = \frac{1}{2}(\Lambda_{\eta} + |\Lambda_{\eta}|) \quad \Lambda_{\eta}^{-} = \frac{1}{2}(\Lambda_{\eta} - |\Lambda_{\eta}|)$$

$$\Lambda_{\zeta}^{+} = \frac{1}{2}(\Lambda_{\zeta} + |\Lambda_{\zeta}|) \quad \Lambda_{\zeta}^{-} = \frac{1}{2}(\Lambda_{\zeta} - |\Lambda_{\zeta}|)$$

Here we adopt the convention that the absolute value of a diagonal matrix is the diagonal matrix which is resulted after each diagonal element in the matrices has been taken its absolute value. Therefore diagonal matrices Λ_k^{+} and Λ_k^{-} with $k = \xi, \eta$ and ζ contain only non-negative and non-positive elements respectively. Let

$$\tilde{A}_0^{+} = T_{\xi} \Lambda_{\xi}^{+} T_{\xi}^{-1} \quad \tilde{A}_0^{-} = T_{\xi} \Lambda_{\xi}^{-} T_{\xi}^{-1}$$

$$\tilde{B}_0^{+} = T_{\eta} \Lambda_{\eta}^{+} T_{\eta}^{-1} \quad \tilde{B}_0^{-} = T_{\eta} \Lambda_{\eta}^{-} T_{\eta}^{-1}$$

$$\tilde{C}_0^{+} = T_{\zeta} \Lambda_{\zeta}^{+} T_{\zeta}^{-1} \quad \tilde{C}_0^{-} = T_{\zeta} \Lambda_{\zeta}^{-} T_{\zeta}^{-1}$$

The expressions for matrices \tilde{A}_0^{+} , \tilde{A}_0^{-} , \tilde{B}_0^{+} , \tilde{B}_0^{-} , \tilde{C}_0^{+} and \tilde{C}_0^{-} can be obtained by substituting the corresponding diagonal matrices defined above to equation (2.38). From the properties of the Jacobian matrices, we have

$$\tilde{A}_0 = \tilde{A}_0^{+} + \tilde{A}_0^{-}$$

$$\tilde{B}_0 = \tilde{B}_0^+ + \tilde{B}_0^-$$

$$\tilde{C}_0 = \tilde{C}_0^+ + \tilde{C}_0^-$$

The acoustic field equation becomes

$$\frac{\partial}{\partial t} \vec{q} + \tilde{A}_0^+ \frac{\partial}{\partial \xi} \vec{q} + \tilde{A}_0^- \frac{\partial}{\partial \xi} \vec{q} + \tilde{B}_0^+ \frac{\partial}{\partial \eta} \vec{q} + \tilde{B}_0^- \frac{\partial}{\partial \eta} \vec{q} + \tilde{C}_0^+ \frac{\partial}{\partial \zeta} \vec{q} + \tilde{C}_0^- \frac{\partial}{\partial \zeta} \vec{q} = \vec{S} \quad (3.36)$$

We apply only 7-stencil optimized upwind schemes derived in the last section to discretize the spatial derivatives in the acoustic field equations. As it can be seen later that the procedures described here can in fact be used for any upwind schemes. Consider a grid of uniform spacing $\Delta\xi$, $\Delta\eta$ and $\Delta\zeta$ in ξ , η and ζ coordinates respectively. Denote node (i, j, k) as the grid point with curvilinear coordinates (ξ_i, η_j, ζ_k) which defines $\xi_i = i\Delta\xi$, $\eta_j = j\Delta\eta$ and $\zeta_k = k\Delta\zeta$. The cartesian coordinates of this node can be obtained from the curvilinear coordinate transform. Denote $\vec{q}_{i,j,k}$ as the acoustic variable vector \vec{q} evaluate at node (i, j, k) and at time t . Use the same convention of the subscripts i, j, k for matrices and other variables. We can then approximate the spatial derivatives in the acoustic field equation (3.36) by the optimized upwind finite difference schemes according to the wave propagating directions as the following:

$$\left(\tilde{A}_0^+ \frac{\partial}{\partial \xi} \vec{q} \right)_{i,j,k} = \frac{1}{\Delta\xi} (\tilde{A}_0^+)_{i,j,k} \sum_{l=-4}^2 a_l^{42} \vec{q}_{i+l,j,k}$$

$$\left(\tilde{A}_0^- \frac{\partial}{\partial \xi} \vec{q} \right)_{i,j,k} = \frac{1}{\Delta\xi} (\tilde{A}_0^-)_{i,j,k} \sum_{l=-2}^4 a_l^{24} \vec{q}_{i+l,j,k}$$

$$\left(\tilde{B}_0^+ \frac{\partial}{\partial \eta} \vec{q}\right)_{i,j,k} = \frac{1}{\Delta \eta} (\tilde{B}_0^+)_{i,j,k} \sum_{l=-4}^2 a_l^{42} \vec{q}_{i,j+l,k}$$

$$\left(\tilde{B}_0^- \frac{\partial}{\partial \eta} \vec{q}\right)_{i,j,k} = \frac{1}{\Delta \eta} (\tilde{B}_0^-)_{i,j,k} \sum_{l=-2}^4 a_l^{24} \vec{q}_{i,j+l,k}$$

$$\left(\tilde{C}_0^+ \frac{\partial}{\partial \xi} \vec{q}\right)_{i,j,k} = \frac{1}{\Delta \xi} (\tilde{C}_0^+)_{i,j,k} \sum_{l=-4}^2 a_l^{42} \vec{q}_{i,j,k+l}$$

$$\left(\tilde{C}_0^- \frac{\partial}{\partial \xi} \vec{q}\right)_{i,j,k} = \frac{1}{\Delta \xi} (\tilde{C}_0^-)_{i,j,k} \sum_{l=-2}^4 a_l^{24} \vec{q}_{i,j,k+l}$$

In the two-dimension, after the split techniques are applied to the Jacobian matrices, the acoustic field equation can be written as

$$\frac{\partial}{\partial t} \vec{q} + \tilde{A}_0^+ \frac{\partial}{\partial \xi} \vec{q} + \tilde{A}_0^- \frac{\partial}{\partial \xi} \vec{q} + \tilde{B}_0^+ \frac{\partial}{\partial \eta} \vec{q} + \tilde{B}_0^- \frac{\partial}{\partial \eta} \vec{q} = \vec{S} \quad (3.37)$$

The diagonal matrices Λ_k^+ and Λ_k^- with $k = \xi$ and η and the split Jacobian matrices \tilde{A}_0^+ , \tilde{A}_0^- , \tilde{B}_0^+ and \tilde{B}_0^- are defined similarly as those in three-dimension. Expressions can be obtained from the corresponding two-dimensional formulae given in section 2.3.2. For example, the expressions for \tilde{A}_0^+ , \tilde{A}_0^- , \tilde{B}_0^+ and \tilde{B}_0^- can be obtained by substituting the diagonal matrices to equation (2.48). The same discretization procedures as those in three-dimension are then applied to approximate the spatial derivatives in the two-dimensional acoustic field equation (3.37). Note that the above described procedures of extension of the optimized upwind schemes are limited to the acoustic field equation. They can be applied to any wave equations in general.

3.4 Time Discretizations

The acoustic field equation (2.27) in three-dimension reduces to a system of ordinary differential equations in time after spatial discretization, which can be written in the form:

$$\left(\frac{d\vec{q}}{dt}\right)_{i,j,k} = -\vec{R}_{i,j,k} \quad (3.38)$$

where

$$\vec{R}_{i,j,k} = \left(\tilde{A}_0^+ \frac{\partial}{\partial \xi} \vec{q} + \tilde{A}_0^- \frac{\partial}{\partial \xi} \vec{q} + \tilde{B}_0^+ \frac{\partial}{\partial \eta} \vec{q} + \tilde{B}_0^- \frac{\partial}{\partial \eta} \vec{q} + \tilde{C}_0^+ \frac{\partial}{\partial \zeta} \vec{q} + \tilde{C}_0^- \frac{\partial}{\partial \zeta} \vec{q} \right)_{i,j,k} - \vec{S}_{i,j,k} \quad (3.39)$$

with the spatial derivatives at grid node (i, j, k) replaced by the corresponding optimized upwind finite differences as described in the previous section. Similarly the acoustic field equation (2.39) in two-dimension becomes

$$\left(\frac{d\vec{q}}{dt}\right)_{i,j} = -\vec{R}_{i,j} \quad (3.40)$$

Where

$$\vec{R}_{i,j} = \left(\tilde{A}_0^+ \frac{\partial}{\partial \xi} \vec{q} + \tilde{A}_0^- \frac{\partial}{\partial \xi} \vec{q} + \tilde{B}_0^+ \frac{\partial}{\partial \eta} \vec{q} + \tilde{B}_0^- \frac{\partial}{\partial \eta} \vec{q} \right)_{i,j} - \vec{S}_{i,j} \quad (3.41)$$

with the spatial derivatives at grid node (i, j) also replaced by the corresponding optimized upwind finite differences. In order to treat the systems of ordinary differential equations (3.38) in three-dimension and (3.40) and in two-dimension together, we will drop the subscripts which denote the spatial grid nodes.

Since acoustic wave propagation problems are generally not stiff, explicit methods are appropriate. Optimized Adams-Bashforth and Rung-Kutta families for the wave propagation have been investigated by many researchers (Hardin *et al.*, 1995). Many low-storage multi-stage methods were introduced to integrate ordinary differential equations (Zigg *et al.*, 1993). The main purpose in the first part of the thesis is to develop and demonstrate the optimized upwind schemes. We therefore simply apply Tam and Webb's optimized time discretization developed in their DRP method to integrate equations (3.38) and (3.40) (Tam and Webb, 1993). Let us refer to the model wave equation (3.1). In order to advance to the next time level, Tam and Webb considered a four-level finite difference approximation to the derivative of $\partial u / \partial t$ in the following form:

$$u^{(n+1)} - u^{(n)} \approx \Delta t \sum_{l=0}^3 b_l \left(\frac{\partial u}{\partial t} \right)^{(n-l)} \quad (3.42)$$

where Δt is the time step and superscript n is an integer which denotes time level. Therefore variable with the superscript n means that the variable is evaluated at time $n\Delta t$. For example, $u^{(n)} = u(x, n\Delta t)$. Similar to the construction of a finite difference approximation to a spatial derivative, the coefficients b_l can be obtained solely through Taylor expansion. As it is argued before, the finite difference scheme obtained with solely Taylor expansion is good only when the frequency is relative low. Therefore the optimized procedure is needed. To be more specific, after the time discretization and without the spatial discretization the model wave equation (3.1) becomes a semi-discrete equation:

$$u^{(n+1)} - u^{(n)} = -\Delta t \sum_{l=0}^3 b_l c \left(\frac{\partial u}{\partial x} \right)^{(n-l)} \quad (3.43)$$

Consider also the fundamental solution with a given frequency ω instead of wavenumber α in the following form:

$$\varphi_s(x, n\Delta t) = e^{i(\alpha x - \omega n\Delta t)} \quad (3.44)$$

Substituting the above fundamental solution into equation (3.43), we have

$$e^{i(-\omega\Delta t)} - 1 = \left(-i\Delta t \sum_{l=0}^3 b_l e^{i(-\omega l\Delta t)} \right) c\alpha \quad (3.45)$$

Denote

$$\bar{\omega} = \frac{i[e^{i(-\omega\Delta t)} - 1]}{\Delta t \sum_{l=0}^3 b_l e^{i(-\omega l\Delta t)}} \quad (3.46)$$

From equation (3.45) the dispersion relation of the semi-discrete equation (3.43) is given as:

$$\bar{\omega} = c\alpha \quad (3.47)$$

Therefore the goal is to construct the coefficients b_l such that $\bar{\omega}$ is close to ω for relative large band of frequency. $\bar{\omega}$ is then called the effective numerical angular frequency. The procedures described for the optimized spatial finite difference schemes can also be applied for the temporal finite difference scheme. Tam and Webb used Taylor expansion to ensure the $\bar{\omega}$ approximates ω to order of $(\Delta t)^3$, i.e. $\bar{\omega} = \omega + O(\Delta t^3)$ and minimize the error L_2 norm E :

$$E = \int_{-0.5}^{0.5} \{ \lambda [\text{Re}(\bar{\omega}\Delta t) - \omega\Delta t]^2 + (1 - \lambda) [\text{Im}(\bar{\omega}\Delta t)]^2 \} d(\omega\Delta t) \quad (3.48)$$

They chose $\lambda = 0.36$ and obtained the coefficients $b_0 = 2.3025581$, $b_1 = -2.4910076$, $b_2 = 1.5743409$ and $b_3 = -0.38589142$.

Using Tam and Webb's temporal finite difference scheme, we can discretize the system of semi-discrete ordinary equations (3.38) in three-dimension and (3.40) in two-dimension. After dropping the subscripts for the grid node and discretizing the temporal derivatives in equations (3.40) and (3.38), we obtain the full-discrete algebraic equations in the following form:

$$\vec{q}^{(n+1)} = \vec{q}^{(n)} - \Delta t \sum_{l=0}^3 b_l \vec{R}^{(n-l)} \quad (3.49)$$

with $\vec{R}^{(n-l)}$ given by equation (3.39) in three-dimension and by equation (3.41) in two-dimension. In our computations, we let $\vec{R}^{(n-l)} = 0$ for $n \leq l$, in another word we assume that time derivatives are zero when the actual time is less than zero.

3.5 Boundary Conditions

Since the computation domain can not go to infinity, outer boundaries which enclose a finite interior domain are required. Through the outer boundary, acoustic waves are radiating from the interior domain to the outer region. There are also fluids leaving and entering the interior domain through the outer boundaries. Since the outer boundaries are chosen

far enough away from the source, flows near outer boundaries can be treated to be uniform. Therefore there are no disturbances coming into the interior domain. As it is discussed before, the disturbances consist of entropy, vorticity and acoustic waves, each having distinct wave propagation characteristics. The outer boundary conditions should be transparent to allow the disturbances to leave the outer boundaries without significant reflections. Since acoustic waves are propagating with the relative speed of sound to the fluid velocity, and the entropy and vorticity waves are propagating along with the flow, there are basically two types of outer boundary conditions, namely radiation and outflow boundary conditions. Radiation boundary condition is used only for acoustic waves radiating to the far region through the boundaries. The outflow boundary condition, however, is used for the combination of outgoing acoustic, entropy and vorticity waves. Near the surface of solid objects inside the interior computational domain wall boundary condition is needed to enforce the non-permeating flow condition. Significant progress has been made in the development of numerical boundary conditions for high order finite difference schemes on uniform Cartesian grids (Hixon *et al.*, 1995, Tam 1997, Tam *et al.*, 1996). Radiation and outflow boundary conditions proposed by Tam & Webb based on asymptotic solutions of the governing equations have been numerically shown to be very effective. They derived the radiation and outflow boundary conditions by applying Fourier-Laplace transform to the two-dimensional acoustic field equations in a uniform flow along the positive x -axis and employing sophisticated mathematical techniques of integration analysis. In this section, we derive the radiation boundary conditions through intuitive observations in both two-dimension and three-dimension. We will also discuss 7-stencil forth order one-side biased finite differences ($M+N=7$, $P=4$) used to discretize the spatial

derivatives near the wall and outer boundaries.

3.5.1 Optimized One-Side Biased Spatial Discretizations Near Boundaries

The general curvilinear coordinate transformations given in Chapter 2 are employed to map the physical domain into computational domain in which the body surface is usually transformed to a boundary of computational domain permitting easy application of surface boundary conditions. Figure 2 schematically shows mapping a two-dimensional physical domain with a wall into a computational plane. The index of grid points in η direction shown in Figure 2 starts from the minimum 1 which denotes the wall to the maximum JM which represents the outer boundary. Since only the values of variables inside the computational domain are available, one-side biased spatial finite difference schemes are needed to discretize spatial derivatives for the grid points near the boundaries.

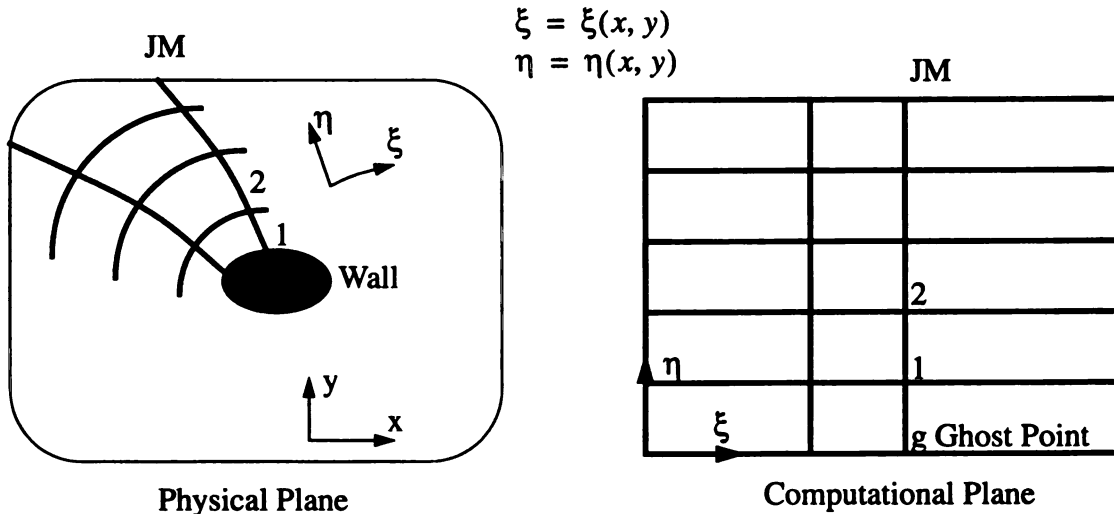


Figure 2 Schematically showing the mapping of a physical space to a computational space

Table 2 gives the coefficients a_j^{51} and a_j^{60} of 7-stencil one-side biased spatial finite difference schemes. Here the subscriptions have the same meaning as those described before. a_j^{51} was obtained by the procedure described in section 3.2 with $P = 4$ $\beta_0 = \pi/2$, $\lambda = 0.01$ and $\sigma = 0.2\pi$. a_j^{60} , however, represents standard six order accurate one-side scheme and was obtained solely with Taylor expansion. The reason for choosing the standard scheme for a_j^{60} is that we found based on visual evaluation that optimization did not make any improvement for this case. Note that $a_j^{15} = -a_{-j}^{51}$ and $a_j^{06} = -a_{-j}^{60}$.

Table 2 Coefficients for one-side biased schemes used in boundaries

$N = 5, M = 1$		$N = 6, M = 0$	
a_{-5}^{51}	-0.0283927780285557	a_{-6}^{60}	1/6
a_{-4}^{51}	0.192107686530459	a_{-5}^{60}	-6/5
a_{-3}^{51}	-0.617980095557289	a_{-4}^{60}	15/4
a_{-2}^{51}	1.28536574416235	a_{-3}^{60}	-20/3
a_{-1}^{51}	-2.14340185401956	a_{-2}^{60}	15/2
a_0^{51}	1.11244509330028	a_{-1}^{60}	-6
a_1^{51}	0.199856203612323	a_0^{60}	49/20

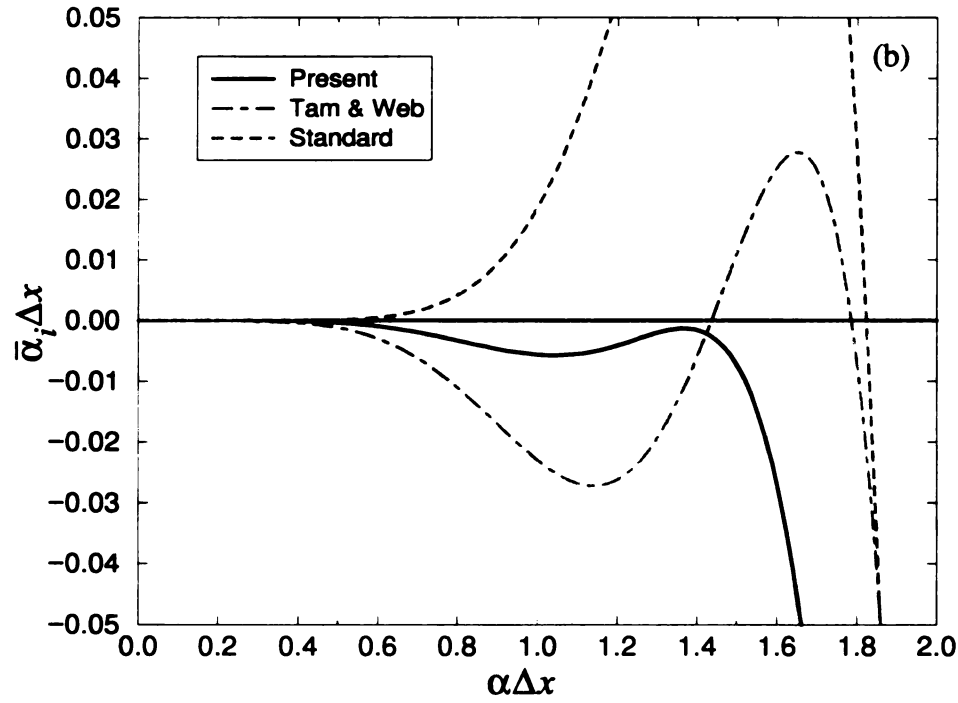
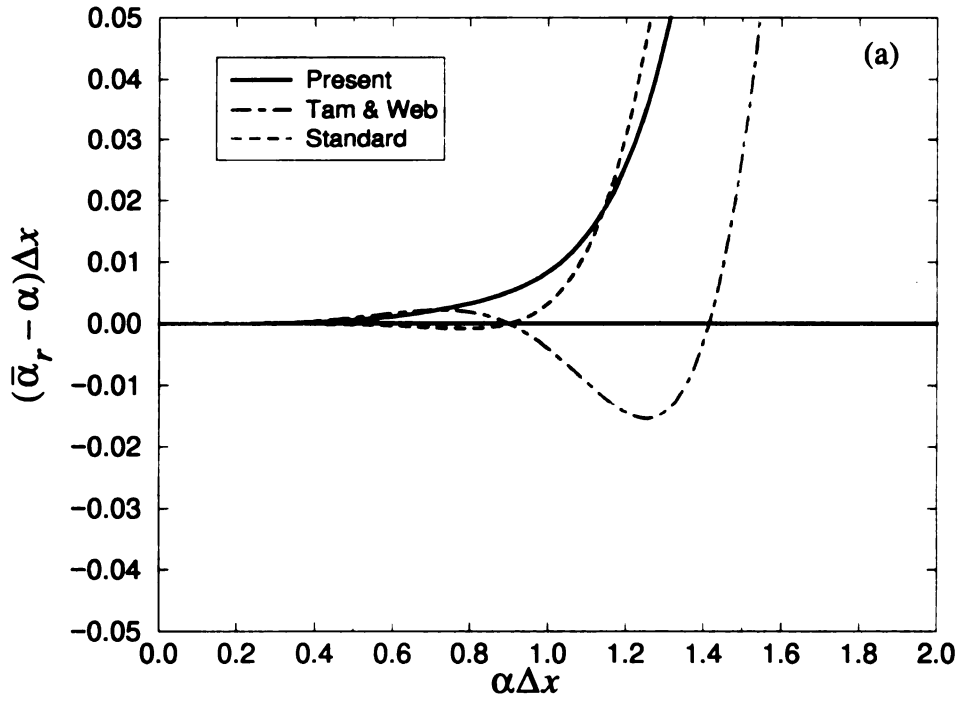


Figure 3 Effective numerical wavenumber versus wavenumber for one-side biased 7-stencil schemes: Present optimized scheme used near boundary ($N=5$, $M=1$, $P=4$); Tam & Webb's backward DRP used near boundary ($N=5$, $M=1$, $P=4$); Standard six-order accurate scheme ($N=5$, $M=1$, $P=6$)

Figure 3 compares the effective numerical wavenumbers for the present optimized scheme ($N=5$, $M=1$, $P=4$) whose coefficients are given in Table 2 with other schemes. It is shown that the standard six order accurate scheme gives the best approximation of the real part of the effective numerical wavenumber to the actual wavenumber for $\alpha\Delta x \leq 1$ among all schemes shown in the figure. Its imaginary part of the effective numerical wavenumber, however, gives the poorest approximation to the zero. As it is discussed in section 3.2, the numerical errors come from both the real and imaginary parts of the effective numerical wavenumber. Good scheme should balance the errors from both parts. Figure 3 shows that the optimized scheme is the best choice based on overall accuracy for $\alpha\Delta x \leq 1$.

3.5.2 Wall Boundary Condition

To illustrate the general ideal of imposing the wall boundary condition we consider here only in two-dimension, because it can be easily extended to three-dimension. We also assume that the curvilinear coordinates on the wall are orthogonal which is important to ensure the accurate implementation of the wall boundary condition. For non-orthogonal coordinates other approaches for implementing high order wall boundary condition should be explored. It requires extensive study for this topic alone as it is pointed out by Tam (1997). On a solid wall the normal velocities of both the mean flow and the acoustic wave are zero. The Jacobian matrix in the normal direction has only two non-zero eigenvalues. One is positive and the other is negative. It implies that only one boundary condition should be imposed on the wall based on local characteristic analysis. From the acoustic field equations, we can express the derivative of pressure disturbance in term of velocity, density and curvature only. The derivative of pressure disturbance is used to provide the

boundary condition on the wall.

Let's refer to Figure 2 in which the wall is represented by a constant η line in physical plane. We derive the derivative $\partial p / \partial \eta$ on the wall first. Denote \hat{x} and \hat{y} the unit vectors in Cartesian x -direction and y -direction respectively. $\hat{\xi}$ and $\hat{\eta}$ are the unit vectors in the ξ and η directions respectively. We have

$$\hat{\xi} = (x_{\xi} \hat{x} + y_{\xi} \hat{y}) / \sqrt{x_{\xi}^2 + y_{\xi}^2}$$

$$\hat{\eta} = (x_{\eta} \hat{x} + y_{\eta} \hat{y}) / \sqrt{x_{\eta}^2 + y_{\eta}^2}$$

Note that η axis on the wall is now in the same direction as the normal \vec{n} . On the wall we have $\vec{V} = V \hat{\xi}$. Using the orthogonality of $\hat{\xi}$ and $\hat{\eta}$, and other metric properties of the transform, on the wall we have

$$u_0 x_{\eta} + v_0 y_{\eta} = 0, \quad u x_{\eta} + v y_{\eta} = 0$$

$$u_0 \eta_x + v_0 \eta_y = 0, \quad u \eta_x + v \eta_y = 0$$

Multiply x_{η} to the second component equation and y_{η} to the third component equation in acoustic field equation (2.39). Adding them together and noticing

$$\eta_x x_{\eta} + \eta_y y_{\eta} = 1$$

we obtain

$$(u_0 \xi_x + v_0 \xi_y)(x_{\eta} u_{\xi} + y_{\eta} v_{\xi}) + \frac{1}{\rho} \frac{\partial p}{\partial \eta} = x_{\eta} s_2 + y_{\eta} s_3$$

where s_2 and s_3 are the second and the third components of the known vector \vec{S} in the right hand side of equation (2.39). Use the fact $(x_{\eta} u + y_{\eta} v)_{\xi} = 0$ and

$$x_{\eta} u_{\xi} + y_{\eta} v_{\xi} = (x_{\eta} u + y_{\eta} v)_{\xi} - u x_{\xi \eta} - v y_{\xi \eta} = -(u x_{\xi \eta} + v y_{\xi \eta})$$

Finally on the wall we have the expression for the pressure derivative,

$$\frac{\partial p}{\partial \eta} = \rho[(u_0 \xi_x + v_0 \xi_y)(u x_{\xi\eta} + v y_{\xi\eta}) + (x_\eta s_2 + y_\eta s_3)] \quad (3.50)$$

This expression can also be derived by linearizing the well known expression of $\frac{\partial p}{\partial n} = \rho V^2 / R$ and employing other facts about the transform. Here R is the curvature radius of the wall.

We are now implementing the wall condition. Again refer to Figure 2 which also shows that a level of ghost points denoted by the index g is added to the computational domain. The level of ghost points is used to impose the pressures derivative on the wall. One the wall we let

$$\left(\frac{\partial p}{\partial \eta}\right)_1 = \frac{1}{\Delta \eta} \left(\sum_{j=1}^6 a_{j-1}^{15} p_j + a_{-1}^{15} p_g \right)$$

with $\frac{\partial p}{\partial \eta}$ given in equation (3.50). We solve the above equation for the only unknown p_g and store its value in the ghost point g . For all variables except for pressure one-side biased finite difference schemes are used with index starting from 1. For example, for u at index 1, 2, 3 and 4 we respectively use

$$\left(\frac{\partial u}{\partial \eta}\right)_1 = \frac{1}{\Delta \eta} \sum_{j=1}^7 a_{j-1}^{06} u_j$$

$$\left(\frac{\partial u}{\partial \eta}\right)_2 = \frac{1}{\Delta \eta} \sum_{j=1}^7 a_{j-2}^{15} u_j$$

$$\left(\frac{\partial u}{\partial \eta}\right)_3 = \frac{1}{\Delta \eta} \sum_{j=1}^7 a_{j-3}^{24} u_j$$

$$\left(\frac{\partial u}{\partial \eta}\right)_4 = \frac{1}{\Delta \eta} \sum_{j=1}^7 a_{j-4}^{33} u_j$$

where the coefficients a_j^{33} are from Tam and Webb's central DRP scheme which is used for one level of grid points near boundaries only. For pressure, the one-side biased finite difference schemes are similarly used. The index, however, includes the ghost point g instead of starting from index 1. For example for index 2, we use

$$\left(\frac{\partial p}{\partial \eta}\right)_2 = \frac{1}{\Delta \eta} \left(\sum_{j=1}^6 a_{j-2}^{24} p_j + a_{-2}^{24} p_g \right)$$

We should note here it is not necessary to calculate $\partial p / \partial \eta$ at ghost point g which is not used in discretization of acoustic equation, and the derivative at index 1 which is already known from its expression.

3.5.3 Radiation Boundary Condition

As it is pointed out that the outer boundary is chosen far away from the source, therefore the uniform flow near outer boundary can be assumed. The behavior of the acoustic disturbance approaching outer boundary from asymptotic analysis is that it is propagating at the relative speed of sound to the flow. Refer to Figure 4 which schematically shows vorticity, entropy and acoustic waves near the outer boundary in a two-dimension uniform flow. The acoustic disturbance is approaching to the point (x, y) on the outer boundary with the speed \tilde{V} as shown in Figure 4 in two-dimension. We can describe the behaviors of the acoustic vector \vec{q} at a point on an outer boundary with distance r from the source as

$$\vec{q} = \frac{\vec{f}(r - \tilde{V}t)}{\sqrt{r}} \quad \text{and} \quad \vec{q} = \frac{\vec{f}(r - \tilde{V}t)}{r}$$

for two-dimension and three-dimension respectively (Whitham, 1974). Taking the derivative of \vec{q} with respect to time t and radius r , we have the following equations

$$\frac{\partial \vec{q}}{\partial t} + \tilde{V} \left(\frac{\partial \vec{q}}{\partial r} + \frac{1}{2r} \vec{q} \right) = 0 \quad (3.51)$$

$$\frac{\partial \vec{q}}{\partial t} + \tilde{V} \left(\frac{\partial \vec{q}}{\partial r} + \frac{1}{r} \vec{q} \right) = 0 \quad (3.52)$$

for two-dimension and three-dimension respectively.

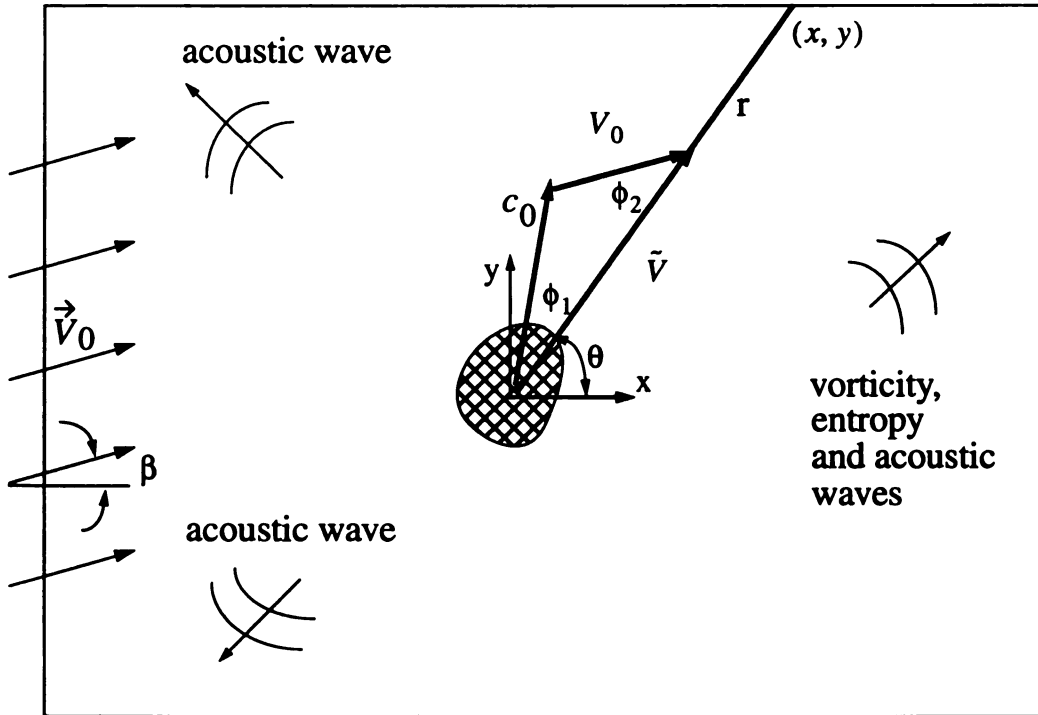


Figure 4 Schematically showing acoustic, vorticity and entropy wave sources in a uniform flow

Equations (3.51) and (3.52) are transferred to the curvilinear space and discretized with one-side biased finite difference schemes. Near the outer boundary where there are only acoustic waves radiating to far field, we solve the above equations instead of the acoustic field equations. But the speed \tilde{V} , however, must be determined first. From the triangle shown in Figure 4, it can be easily checked that

$$\tilde{V} = c_0 \cos \phi_1 + V_0 \cos \phi_2 \quad (3.53)$$

Let \hat{r} be the unit vector pointing from the source center to the point (x, y) on the outer boundary shown in Figure 4. Notice that

$$\begin{aligned} \cos \phi_2 &= \frac{(\vec{V}_0 \cdot \hat{r})}{V_0} \\ \sin \phi_1 &= \frac{V_0 \sin \phi_2}{c_0} = \frac{\sqrt{V_0^2 - (\vec{V}_0 \cdot \hat{r})^2}}{c_0} \end{aligned}$$

Therefore we have

$$\tilde{V} = \sqrt{c_0^2 - V_0^2 + (\vec{V}_0 \cdot \hat{r})^2} + (\vec{V}_0 \cdot \hat{r}) \quad (3.54)$$

In two-dimension we can write \tilde{V} in term of components of mean flow velocity and the angle θ between the vector \hat{r} and x -axis shown in Figure 4. Chose the center of source as the origin of the Cartesian coordinates, then we have

$$\hat{r} = (\cos \theta, \sin \theta)$$

Noticing that

$$\vec{V}_0 = (u_0, v_0)$$

$$V_0^2 = u_0^2 + v_0^2$$

and

$$V_0^2 - (\vec{V}_0 \cdot \hat{r})^2 = u_0^2 + v_0^2 - (u_0 \cos \theta + v_0 \sin \theta)^2 = (u_0 \sin \theta - v_0 \cos \theta)^2$$

we obtain

$$\tilde{V}(\theta) = \sqrt{c_0^2 - (u_0 \sin \theta - v_0 \cos \theta)^2} + u_0 \cos \theta + v_0 \sin \theta \quad (3.55)$$

which is the same as those obtained by Tam and Webb with Fourier-Laplace transform and integration techniques.

3.5.4 Outflow Boundary Condition

As it is discussed in chapter 2, the outgoing vorticity and entropy waves are propagating with the flow and do not have effect on the pressure disturbance. Therefore the equation (3.51) in two-dimension and equation (3.52) in three-dimension should also be applied as outflow boundary condition for the pressure disturbance. For other variables, the acoustic field equations are used. Since uniform flow can be assumed near outer boundaries, all the derivatives of mean flow variables are zero. The acoustic field equations become

$$\frac{\partial \rho}{\partial t} + (\vec{V}_0 \cdot \nabla) \rho + \rho_0 (\nabla \cdot \vec{V}) = 0 \quad (3.56)$$

$$\frac{\partial \vec{V}}{\partial t} + (\vec{V}_0 \cdot \nabla) \vec{V} + \frac{1}{\rho_0} \nabla p = 0 \quad (3.57)$$

$$\frac{\partial p}{\partial t} + (\vec{V}_0 \cdot \nabla)p + \gamma p_0(\nabla \cdot \vec{V}) = 0 \quad (3.58)$$

Combined with acoustic energy equation, the acoustic continuity equation can be written as

$$\frac{\partial \rho}{\partial t} + (\vec{V}_0 \cdot \nabla)\rho = -\frac{1}{c_0^2} \left[\frac{\partial p}{\partial t} + (\vec{V}_0 \cdot \nabla)p \right] \quad (3.59)$$

In the computation near the outflow boundaries we use the radiation boundary condition for the pressure p , acoustic continuity equation (3.59) for the density ρ , and acoustic momentum equation (3.57) for the velocity \vec{V} . These equations are also solved in curvilinear coordinates and discretized with one-side biased schemes.

4 APPLICATIONS OF OPTIMIZED UPWIND SCHEMES

To test the effectiveness of the developed 7-stencil optimized upwind scheme and the implementation of the scheme in the multi-dimension in the presence of solid objects, a sequence of direct numerical simulations have been carried out. Exact solutions which are available for some test cases are calculated to validate the numerical results. Furthermore, the standard six-order 7-stencil upwind scheme and Tam and Webb's 7-stencil central DRP scheme are applied to some test cases, and results computed with these schemes are compared with those obtained using the optimized upwind scheme. In all simulations the temporal difference scheme given in section 3.4, is used. For the simulations in which the comparisons of various schemes are made, boundary conditions, time step, and other parameters etc. are set to be the same. Therefore the only differences between the solutions with various methods should come from the spatial discretizations.

4.1 One-Dimensional Model Wave Equation

One-dimensional model wave equation (3.1) has been intensively used to validate numerical schemes. It is necessary for numerical schemes to pass the tests on one-dimensional model wave equation before they can be further applied to more complicated problems. Two pure initial condition problems are considered here. The propagating speed for both problems are normalized and set to be unit, i.e. $c=1$. The initial conditions are given as the following:

$$\text{case 1} \quad u_0(x) = \exp\left[-\ln 2 \left(\frac{x}{3}\right)^2\right]$$

$$\text{case 2} \quad u_0(x) = \begin{cases} 1 & \text{if } -50 \leq x \leq 50 \\ 0 & \text{Otherwise} \end{cases}$$

A Gaussian pulse and a step wave are released initially in the first and the second cases respectively. For the both cases the spatial step Δx and time step Δt are set to 1 and 0.1 respectively. The first case is used to test whether the schemes are able to resolve the wave with the wave length longer than $6\Delta x$ and the second one is used to test the ability of handling discontinuities. The computational boundaries are chosen far enough so that the waves do not reach the boundaries within the considered time.

Figure 5 shows the results at time 400, i.e. after 4000 time steps, computed with the optimized upwind scheme, Tam and Webb's central DRP scheme without damping and the standard six-order accurate scheme. Figure 6 shows the computational errors caused by these three schemes. The error is defined as $\text{error} = u_{\text{numerical}} - u_{\text{exact}}$. These figures demonstrate that the optimized upwind scheme has better accuracy near the peak than the standard scheme derived solely by Taylor expansion, although its order of accuracy is lower than the standard scheme. Figure 6 also indicates that the result obtained with the optimized upwind scheme is more accurate than that obtained with central DRP scheme. Oscillations in the computational error for the central DRP scheme is propagating upstream, instead of being confined near the peak as it is for the optimized upwind scheme.

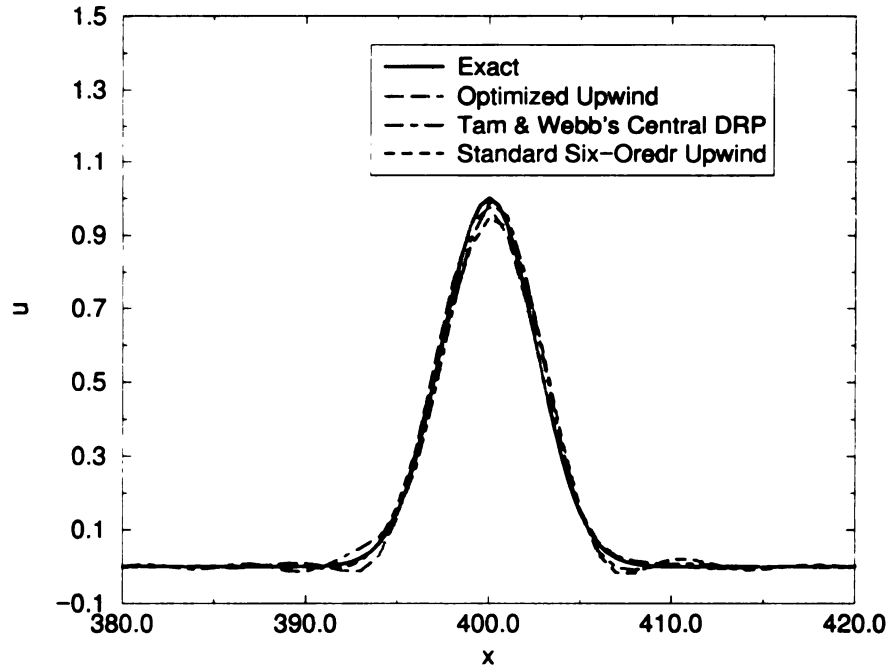


Figure 5 Comparison of exact and computed solutions at $t=400$ with different schemes for the one-dimensional modal wave equation with an initial Gaussian pulse.

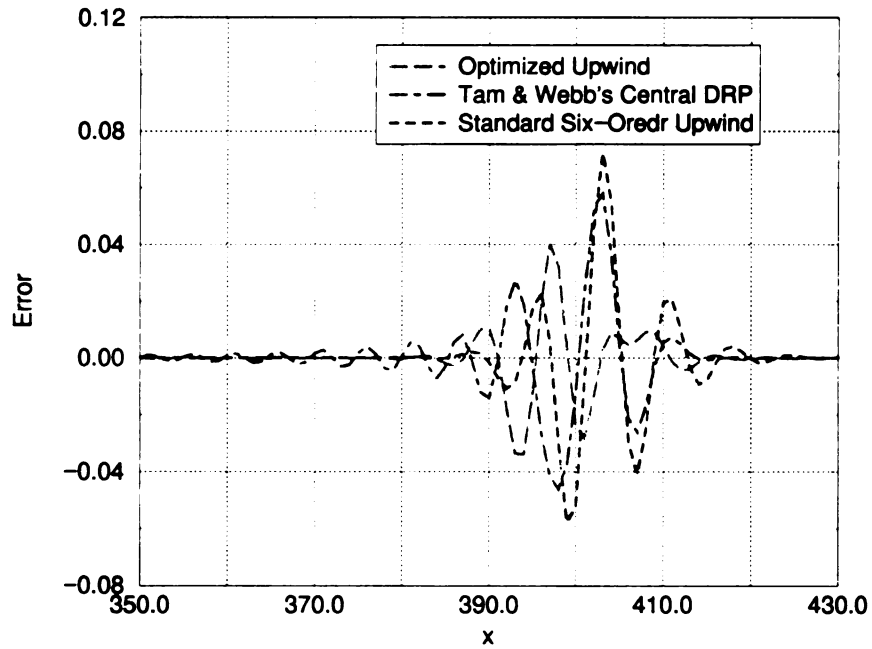


Figure 6 Comparison of computational errors by different schemes for the one-dimensional modal wave equation with a initial Gaussian pulse.

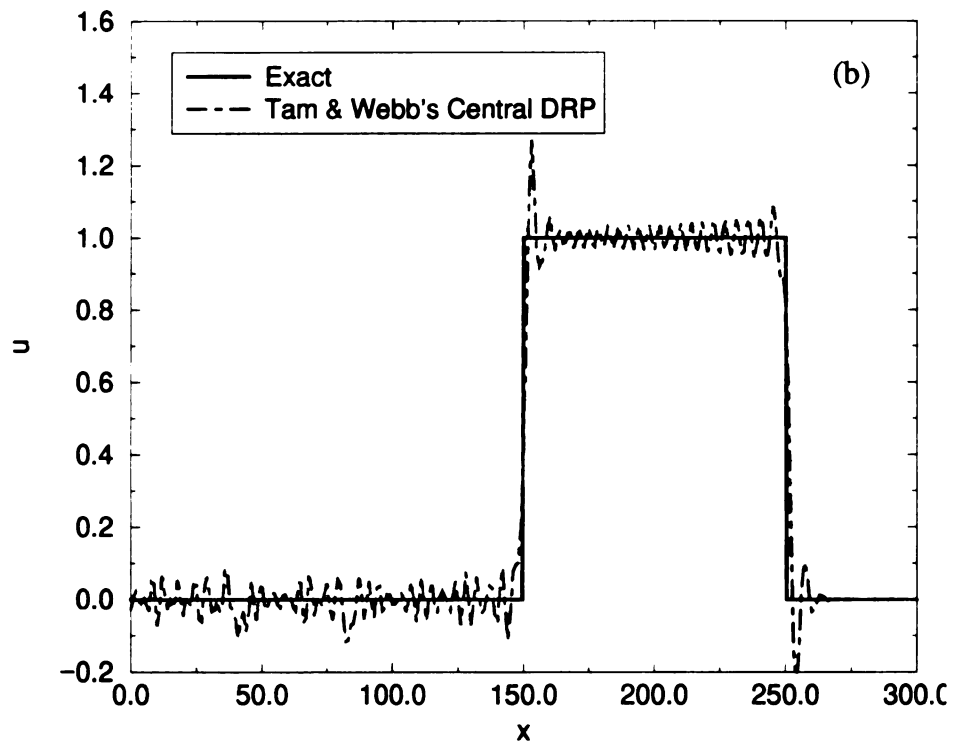
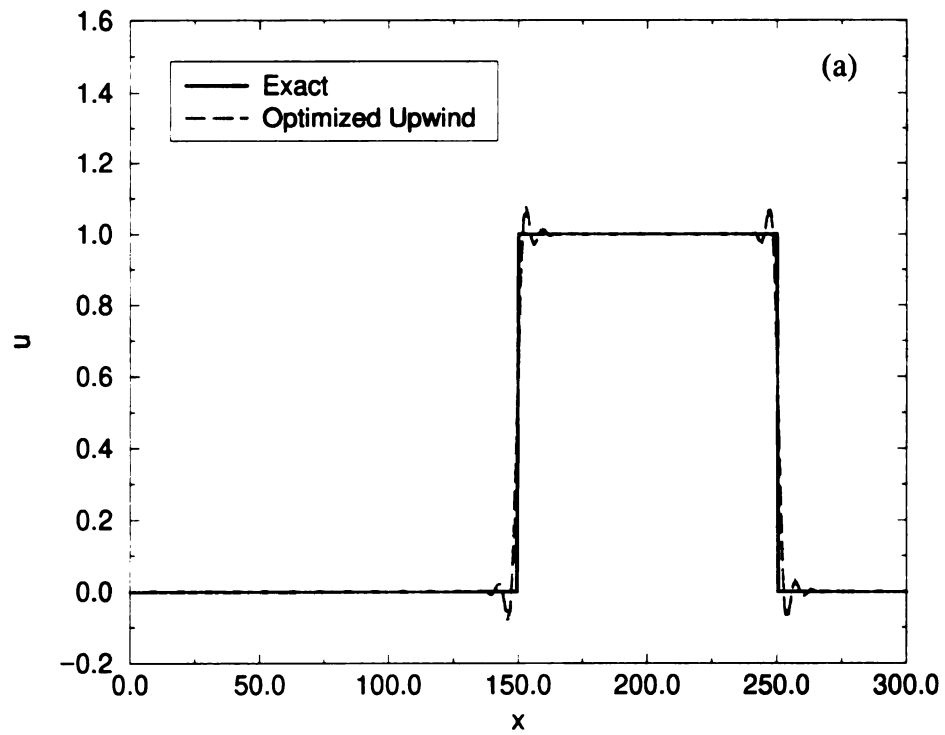


Figure 7 Comparison of exact solution and computed results at $t=200$ with (a): the optimized upwind schemes, (b): Tam and Webb's central DRP without damping, for the one-dimensional modal wave equation with an initial discontinuity

Figure 7 shows computed results at time $t=200$, i.e. after 2000 time steps, with the optimized upwind scheme and Tam and Webb's central DRP scheme without damping. As it is shown in the figure, the solution quality of Tam and Webb's central DRP scheme degrades by the presence of numerous fine scale oscillations. Fine tuned artificial dissipation term is needed to remove the oscillations. In contrast to Tam and Webb's central DRP scheme, the solution of the optimized upwind scheme confines the oscillations near the discontinuity due to the built in dissipation in the scheme.

4.2 Acoustic Radiation from an Oscillating Piston

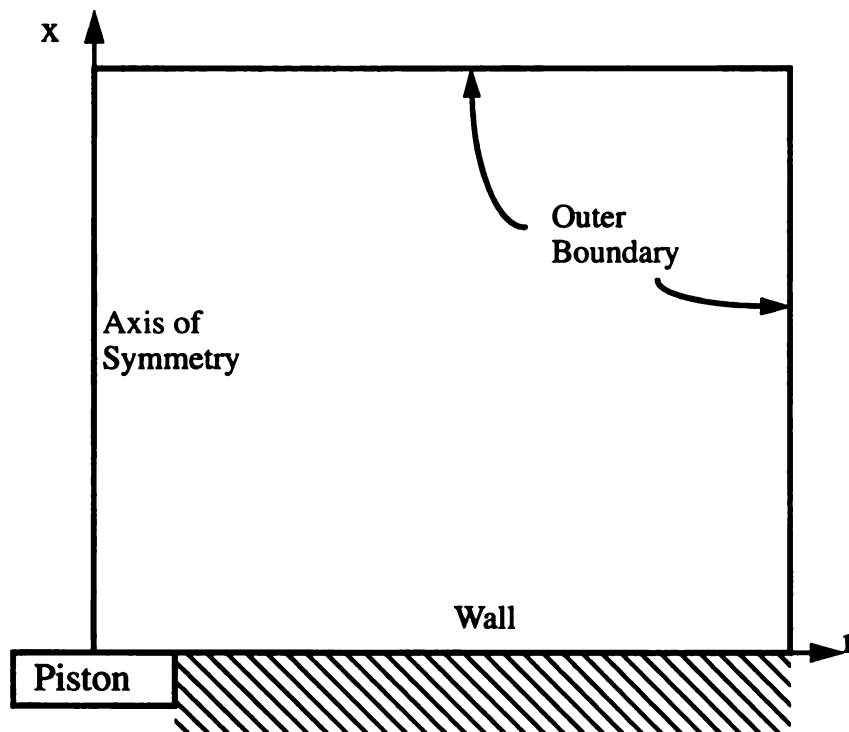


Figure 8 Schematically showing the computational domain for acoustic radiation from an oscillating piston

Acoustic radiation from an oscillating circular piston in a wall is considered here to test the behaviors of the optimized upwind scheme in multi-dimension. The radius of the piston is 10. A cylindrical coordinate system originated at the center of piston is used. The computational domain is set as $0 \leq x \leq 100$ and $0 \leq r \leq 100$ as shown in Figure 8. The governing equations for this case can be easily obtained from equations (2.16), (2.17) and (2.18), which can also be written as equation (2.24) with y replaced by r and the source term $\vec{s} = (-v/r, 0, 0, -v/r)$. Here v is the velocity component in r direction. The piston is moving up and down with the speed of

$$u = 10^{-4} \sin\left(\frac{\pi t}{5}\right)$$

where u is the velocity component in x direction. The grid space Δx and Δr are both set to 1. In the implementation of boundary conditions on the wall and in axis of symmetry, one layer of ghost cells is placed near the boundaries as they are illustrated for the solid wall boundary condition in Chapter 3. The derivatives of pressure along the directions normal to the wall and normal to axis of symmetry can be easily obtained respectively as the following: On the wall, we have

$$\frac{\partial p}{\partial x} = \begin{cases} \frac{10^{-4}\pi t}{5} \cos\left(\frac{\pi t}{5}\right) & 0 \leq r < 10 \\ \frac{10^{-4}\pi t}{10} \cos\left(\frac{\pi t}{5}\right) & r = 10 \\ 0 & r > 10 \end{cases}$$

Since there is discontinuity at $r = 10$, the derivative of pressure at $r = 10$ is set to be the average of those from the left and the right to $r = 10$. In the axis of symmetry, we have

$$\frac{\partial p}{\partial r} = 0$$

Since $r = 0$ in the axis of symmetry, the source term is singular. But $v = 0$ too in the axis of symmetry, therefore v/r can be replaced by $\frac{\partial v}{\partial r}$. Since it is an axisymmetric problem in which acoustic waves are actually propagating in three-dimension, the radiation condition derived for three-dimension instead of two-dimension should be used for the outer boundaries shown in Figure 8.

The exact solution for the pressure disturbance can be written as (Hardin *et al.*, 1995):

$$p = \text{Re} \left[\varepsilon R \omega \int_0^{\infty} \frac{1}{\sqrt{\xi^2 - \omega^2}} J_1(R\xi) J_0(r\xi) \exp(-\sqrt{\xi^2 - \omega^2} x - i\omega t) d\xi \right] \quad (4.1)$$

where Re means the real part of a complex number, $\varepsilon = 10^{-4}$, $R = 10$, $\omega = \frac{\pi}{5}$, J_0 and J_1 are Bessel functions of order 0 and 1 respectively. The evaluation of the above integration is not trivial. Note that the integrand is singular near the point $\xi = \omega$, therefore accurate analytical estimation for the integration over small interval $[\omega - \Delta\omega, \omega + \Delta\omega]$ must be made. Since a numerical computation cannot go to infinity, a finite upper bound instead of infinity is also required and should be chosen so that the error introduced by truncating the integration from the upper-bound to the infinity is within an acceptable small value. A suitable numerical integration algorithm is needed to evaluate the integration over the remaining region. Tam and Webb's DRP method with and without artificial damping are also applied to this case to compare with the optimized upwind scheme. The results shown here are obtained at $t=200$, at which the initial disturbances has propagated out of the computational domain and the pseudo steady state is reached. The pseudo steady state

means that the solution is now periodic sinusoidal wave with a cycle of the piston oscillation as its period. Figure 9 and Figure 10 show surface plot and contour plot for the pressure distribution obtained with the optimized upwind scheme at the beginning of a cycle respectively. Figure 11 show the pressure contours at the beginning of a cycle computed with Tam and Webb's central DRP without damping. For the surface plot, regions with the same pressure value are shown in the same color. For the contour plot, the lines with the same pressure value are drawn in the same color. The contours obtained by the optimized upwind scheme would have been indistinguishable from those of exact solution to an accuracy corresponding to the thickness of the contour lines, if we had plotted them in the same graph. The pressure contours obtained with the central DRP scheme without damping, however, have seriously spurious oscillations.

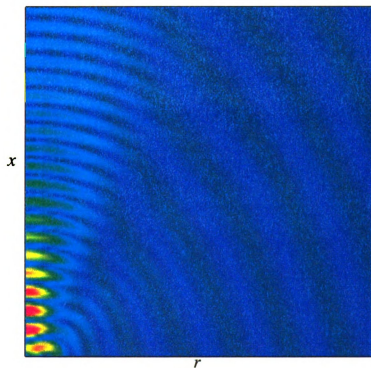


Figure 9 Pressure distribution computed with the optimized upwind scheme at the beginning of a cycle

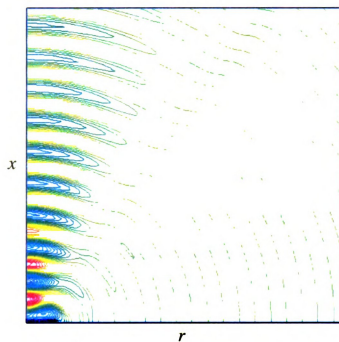


Figure 10 Pressure contours at the beginning of a cycle computed with the optimized upwind scheme

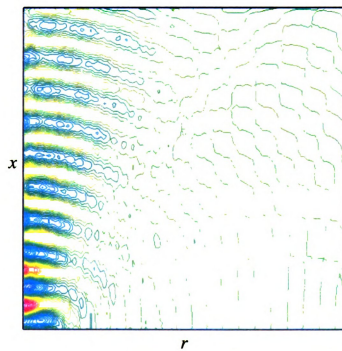


Figure 11 Pressure contours at the beginning of a cycle computed with Tam and Webb's central DRP method without damping

Figure 12 shows the comparison of pressure distributions along the axis of symmetry at the beginning of a cycle. It is shown that the pressure obtained with the optimized upwind scheme is right on top of the exact solution. This figure further validate that the results obtained with the optimized upwind scheme are identical to the exact solutions to an accuracy corresponding to the thickness of lines shown. The pressure distribution obtained with the central DRP scheme without damping, which is far away from the exact one, are also shown in Figure 12. Our computation with the central DRP without damping experienced that the numerical solutions obtained at small time were not too far off the exact solution. But the solutions are getting deteriorated as the computation time increases.

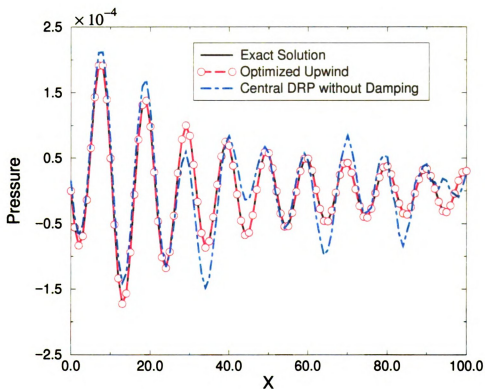


Figure 12 Comparison of pressure distributions along the axis of symmetry at the beginning of a cycle

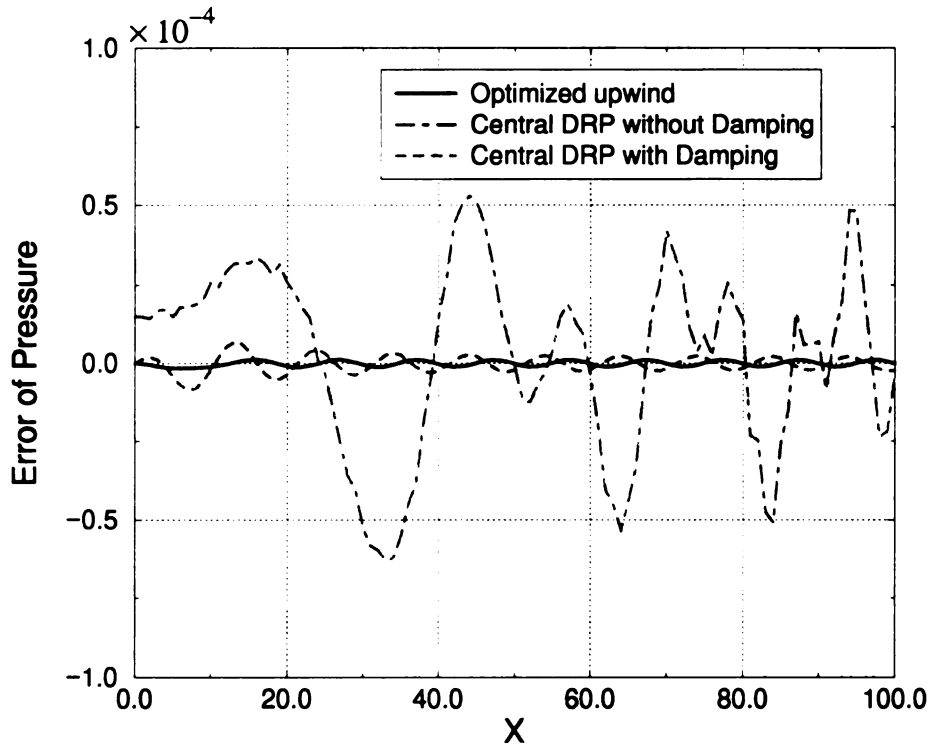


Figure 13 Comparison of computational errors for pressure along the axis of symmetry at the beginning of a circle.

The spurious oscillations caused by the central DRP method without damping can be eliminated by adding an artificial damping term. The artificial coefficients, however, need to be determined through trial and error. Fine tuning is required to get good results. Here we follow the approach of Tam *et al.* and used the same damping coefficients, i.e. an artificial mesh Reynolds number of 5, as it is described in the literature (Hardin *et al.*, 1995). With the inclusion of the artificially selected damping terms, spurious waves are effectively eliminated in the numerical solution. If we had plotted pressure contours and pressure distribution computed using the central DRP scheme with artificial damping together with those computed using the optimized upwind scheme, they would be indistinguishable to an accuracy corresponding to the thickness of lines shown. Figure 13 shows the com-

parison of computational errors for the pressure obtained with the two schemes. It demonstrates that computational error associated with the optimized upwind scheme is significantly less than that associated with the central DRP with finely tuned damping term. It demonstrates the optimized upwind scheme minimizes not only the dissipation errors but also the dissipation errors. Furthermore, the optimized upwind scheme requires less CPU time than the central DRP with damping.

4.3 Acoustic Propagation in a Two-Dimensional Uniform Flow

An acoustic, an entropy and a vorticity disturbances are initially released at different locations in a uniform mean flow. The uniform mean flow is in the direction along $x=y$ with free stream Mach number of 0.5. Figure 14 schematically shows the computational domain, boundary conditions and the locations of initial disturbances. More specifically, the initial conditions for the disturbances are given as the following:

$$\rho(x, y) = \exp\{-(\ln 2)[(x^2 + y^2)/9]\} + 0.1 \exp\{-(\ln 2)[((x - 67)^2 + (y - 67)^2)/25]\}$$

$$u(x, y) = 0.04(y - 67) \exp\{-(\ln 2)[((x - 67)^2 + (y - 67)^2)/25]\}$$

$$v(x, y) = -0.04(x - 67) \exp\{-(\ln 2)[((x - 67)^2 + (y - 67)^2)/25]\}$$

$$p(x, y) = \exp\{-(\ln 2)((x^2 + y^2)/9)\}$$

It is seen that the acoustic disturbance is released initially at the origin of the coordinate system. The acoustic disturbance is propagating at the speed of sound relative to the mean flow. The entropy and vorticity disturbances are released initially at (67, 67). They are propagating at the speed of mean flow.

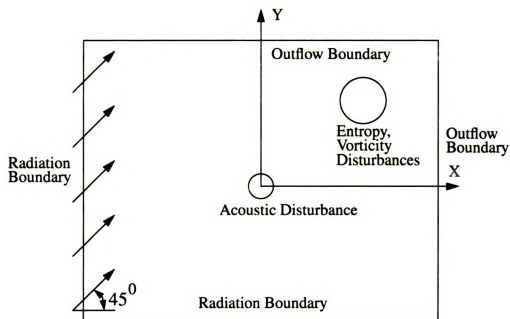


Figure 14 Schematically showing the computational domain, boundary conditions and initial disturbances for acoustic propagation in a two-dimensional uniform flow.

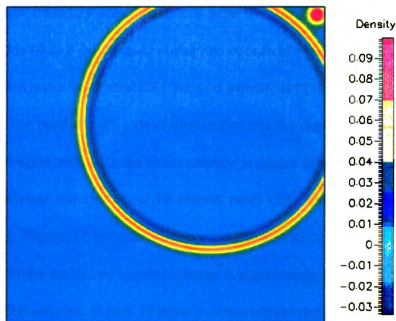


Figure 15 Density distribution computed with the optimized upwind scheme at $t=80$

The exact solution for density can be written as (Hardin *et al.*, 1995):

$$\rho = \frac{1}{2\alpha_1} \int_0^\infty \cos(\xi t) J_0 \xi \sqrt{(x - 0.5t)^2 + y^2} \xi d\xi + 0.1 \exp\{-\alpha_2[(x - 67 - 0.5t)^2 + y^2]\} \quad (4.2)$$

where $\alpha_1 = (\ln 2)/9$, $\alpha_2 = (\ln 2)/25$ and J_0 is Bessel function of order 0. It also requires numerical algorithms to evaluate the integration for the exact solution given in equation (4.2). The computational domain is set as $-100 \leq x \leq 100$ and $-100 \leq y \leq 100$. The gridding spaces Δx and Δy are both set to 1. Note that the radii of the disturbances in the expressions of initial conditions are chosen to test the ability of schemes to resolve the waves with 6 PPW. Figure 15 shows the surface plot for the density distribution computed with the optimized upwind scheme at time 80, where the acoustic disturbance partly propagates out computational domain, catches up and interacts with the entropy and the vorticity disturbances. No visible reflections near the boundaries have been observed, which implies the outflow boundary conditions work quite well for this case. The density wavefront along the line of $x = y$ computed using the optimized upwind scheme is compared with that computed using the central DRP method without damping, and the exact solution (see Figure 16). The solutions are almost identical except the density obtained by the central DRP doesn't agree well with the exact solution at center of acoustic wave. The optimized upwind scheme requires about 10 percent more CPU time than the central DRP without damping. Figure 17 compares the computational errors of above schemes. The error associated to the optimized upwind scheme is significantly less than that associated to the central DRP scheme. Figure 17 clearly demonstrates the advantage of optimized upwind scheme over the central DRP scheme.

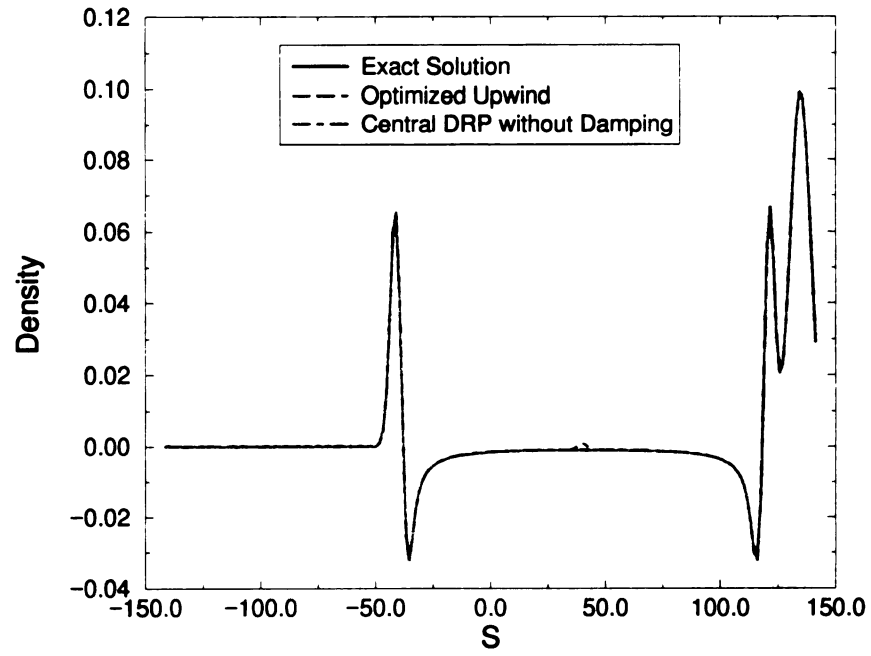


Figure 16 The comparison of density distributions along the line $y = x$ at $t = 80$.

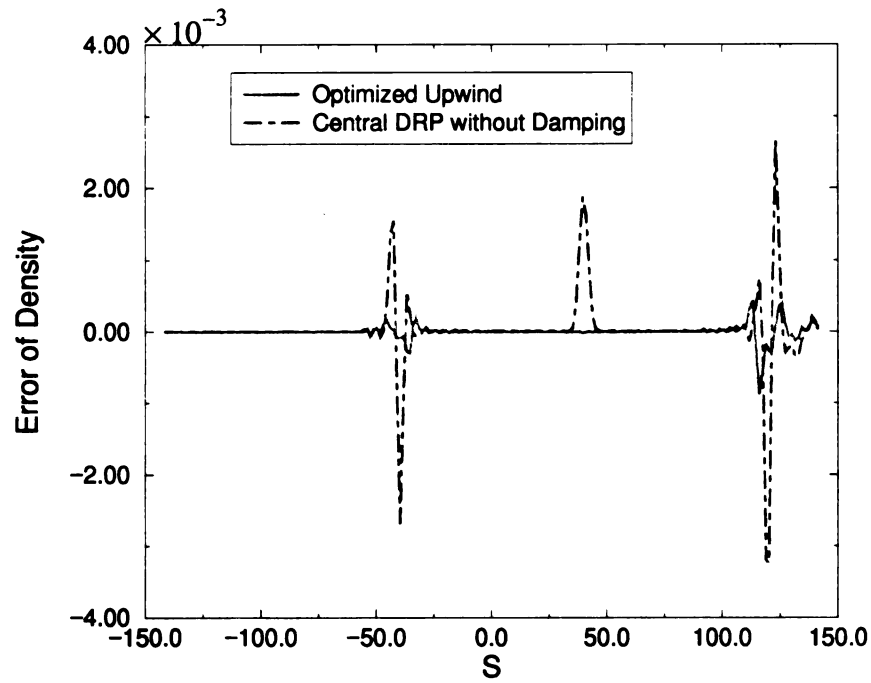


Figure 17 The comparison of computational errors for density along the line $y = x$ at $t = 80$

4.4 Acoustic Reflections

4.4.1 Reflection of an Acoustic Pulse off a Straight Wall in a Two-Dimensional Uniform Flow

Let's refer to Figure 14. The Mach number of the mean flow is 0.5. But the angle of attack is zero degree. The computational domain is now set as $-100 \leq x \leq 100$ and $0 \leq y \leq 200$. The lower boundary is set to be a straight wall instead of a radiation boundary. The initial conditions for the disturbances are now set as $u=v=0$ and

$$p(x, y) = p(x, y) = \exp\{-(\ln 2)[(x^2 + (y - 25)^2)/25]\}$$

In another word, only acoustic disturbance is released initially at $(0, 25)$. The exact solution can be obtained by superposing the two mirror imaged solutions of acoustic propagating in a uniform flow without a wall with two acoustic disturbances initially released at $(0, 25)$ and $(0, -25)$.

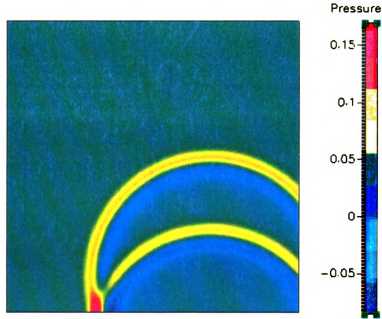


Figure 18 Pressure distribution computed with the optimized upwind scheme at $t=80$

Figure 18 shows the surface plot for the pressure distribution computed with the optimized upwind scheme at time $t = 80$, where the acoustic disturbance hit the wall, incident and reflected waves propagate downstream and move out of the computational domain. Figure 19 and Figure 20 show the comparison of computational errors for the pressure at $t = 80$, along the wall and the line with $x=0$ respectively. These figures also clearly demonstrate the advantage of the optimized upwind scheme over the central DRP scheme. Figure 19 indicates that large computational errors encountered downstream near the lower right corner of the computational domain. These errors are caused by the interaction of the wall and outflow boundary conditions. Further study on accurately imposing boundary conditions at the corner of computational domain is needed to reduce the computational error.

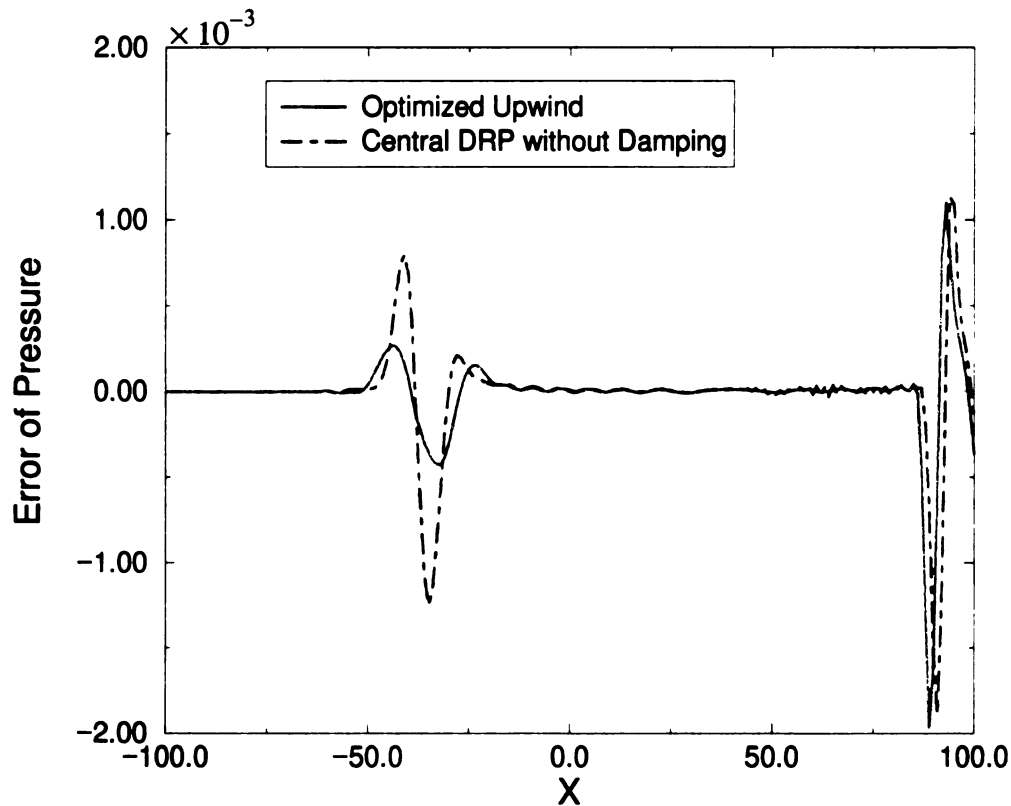


Figure 19 The comparison of computational errors for pressure along the wall at $t = 80$

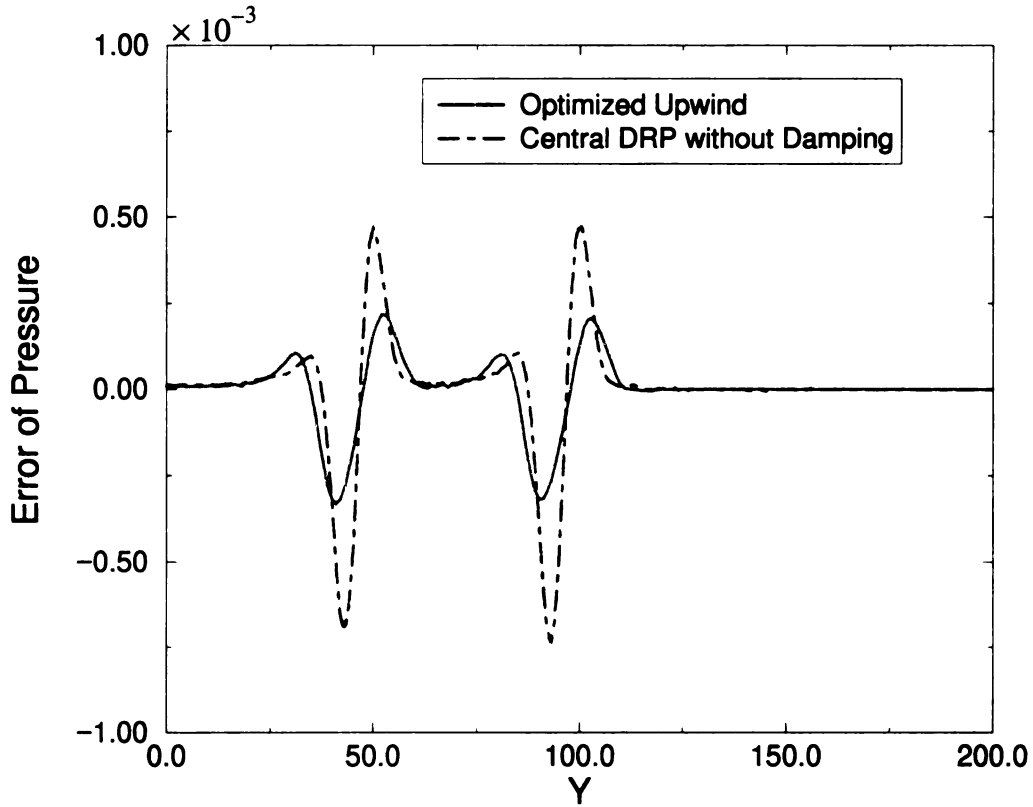


Figure 20 The comparison of computational errors for pressure along the line $x=0$ at $t=80$

4.4.2 Scattering of an Acoustic Pulse off a Cylinder

Unlike the previous applications which are limited to Cartesian coordinates system with straight boundaries, this example is used to study the behaviors of the optimized upwind scheme in the presence of a curved object. Figure 21 shows the diagram of noise source, computational domain and boundaries. The noise source is located at 4 cylinder diameters away from the origin in the x -axis. A uniform flow is assumed in the z -direction which is pointing out of the paper. Therefore a two-dimensional still flow can be assumed in the x and y plane. This example can be associated to the physical problem of finding the

sound field generated by a propeller scattered off by the fuselage of an aircraft. The fuselage is idealized as a circular cylinder, and the noise source is given at a specified location. Since the problem is symmetric about x -axis, the computations are conducted only for the upper half plane. Computational domain is chosen as a semi-circular region which is bounded by an outer semi-circle, the cylinder wall, and symmetric lines. The meshes are generated by the circumferential and radial lines. The polar coordinate systems is used to transfer the acoustic field equation in the Cartesian system as it is described in Chapter 2.

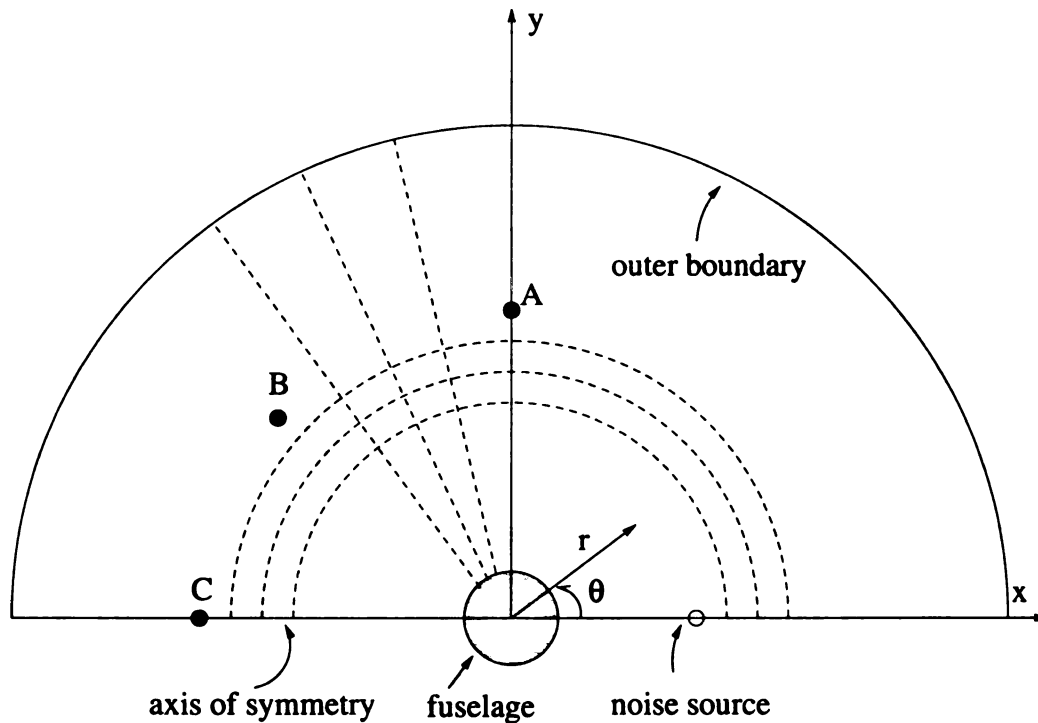


Figure 21 Schematic diagram showing the computational domain and boundaries of acoustic scattering problem

Two cases are considered. In the first case a pressure pulse is initially released and given by

$$p(x, y) = \exp\{-(\ln 2)[(x - 4)^2 + y^2]/0.04]\}$$

In the second case a noise source is added to the acoustic energy equation. The right hand side in equation (2.18) is replaced by the following periodic source term

$$p(x, y) = \exp\{-(\ln 2)[(x - 4)^2 + y^2]/0.04]\} \sin(8\pi t)$$

Wall and outer boundaries are treated by the procedures described in section 3.5. For grid points near the symmetry lines, we have

$$u(x, y) = u(x, -y), \quad v(x, y) = -v(x, -y), \quad p(x, y) = p(x, -y)$$

Since there are only acoustic waves in this case, the density and pressure are identical. A grid system of 200×180 points with $\Delta r = 0.0375D$ and $\Delta\theta = 1^\circ$ is used for the simulation in the first case, where D is the diameter of the cylinder. Time step is chosen as 0.001. Figure 22 shows the surface plot for the pressure distribution at $t = 7$ for the first case. Figure 23 shows the pressure as a function of time for three different locations A, B and C. These figures clearly show the incident wave, reflection wave and the effect of wall on the incident wave. A grid system of 400×360 points with $\Delta r = 0.025D$ and $\Delta\theta = 0.5^\circ$ is used for the simulation in the second case. Time step is chosen as 0.0005. Figure 24 shows the scattered pressure wave patterns at $t = 40$, in which the effect of the cylinder on the scattered sound is clearly demonstrated. Figure 25 gives the computed directivity function $D(\theta) = \overline{r p^2}$ at $r = 9$. The computed results are obtained by marching time to $t = 60$ at which a pseudo steady state is achieved. Since we do not have the exact solutions, the accuracy of the numerical results are unable to be evaluated. Our results qualitatively agree well with those reported in the literatures (Kim *et al.*, 1997, Tam *et al.*, 1997). To obtain high quality results with Tam and Webb's central DRP methods for this problem, artificial damping with different damping coefficients for different region is required as it is pointed out by Tam *et al* (1997).

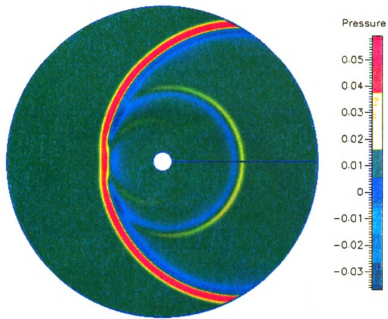


Figure 22 Pressure distribution computed with the optimized upwind scheme at $t = 7$ for the first case in which an acoustic pulse is released initially.

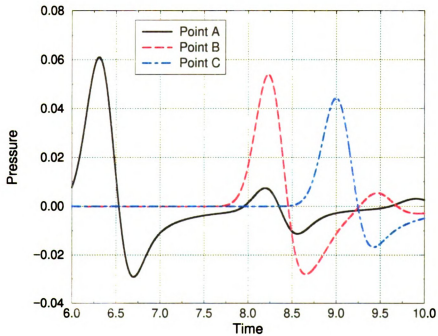


Figure 23 Time history of pressure fluctuation at points A ($r = 5$, $\theta = 90^\circ$), B ($r = 5$, $\theta = 135^\circ$) and C ($r = 5$, $\theta = 180^\circ$) as indicated in Figure 21.

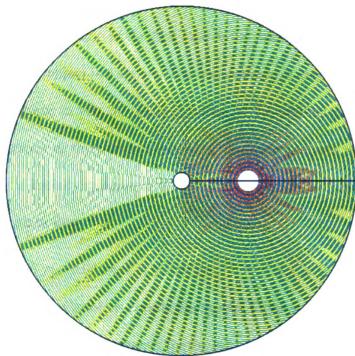


Figure 24 Pressure wave pattern at $t = 40$ simulated by the optimized upwind scheme

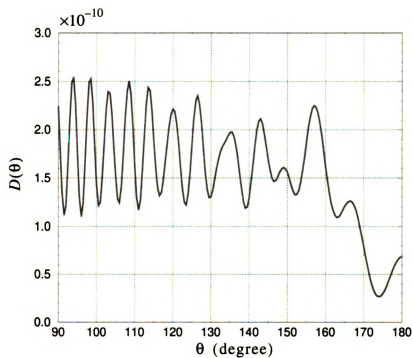


Figure 25 Directivity of radiated sound computed by the optimized upwind scheme

4.4.3 Reflection of an Acoustic Pulse off a Sphere

This problem is almost same as the first case in the scattering of acoustic waves off a cylinder except that the object is a sphere. The computation is carried out with the spherical coordinate transform to test the generalization of the optimized upwind scheme to acoustic field equations in three-dimensional curvilinear coordinate system. A pressure pulse given below is initially released at 2 sphere diameters away from the center of the sphere without the mean flow

$$p(x, y) = -0.01 \exp\{-(\ln 2)[(x-2)^2 + y^2 + z^2]/0.25^2]\}$$

Since the transform of the Cartesian coordinate system to the spherical coordinate system has singularity at poles, special treatments for the grid points near the poles are needed for the numerical stability. Let (r, θ, φ) be the spherical coordinated system, the transform can be written

$$\begin{aligned} x &= r \sin \theta \cos \varphi \\ y &= r \sin \theta \sin \varphi \\ z &= r \cos \theta \end{aligned}$$

The three-dimensional acoustic field equation (2.27) without source term becomes:

$$\begin{aligned} \frac{\partial}{\partial t} \vec{q} + (A_0 \sin \theta \cos \varphi + B_0 \sin \theta \sin \varphi + C_0 \cos \theta) \frac{\partial}{\partial r} \vec{q} \\ + \frac{1}{r} (A_0 \cos \theta \cos \varphi + B_0 \cos \theta \sin \varphi - C_0 \sin \theta) \frac{\partial}{\partial \theta} \vec{q} \\ + \frac{1}{r \sin \theta} (-A_0 \sin \varphi + B_0 \cos \varphi) \frac{\partial}{\partial \varphi} \vec{q} = 0 \end{aligned} \quad (4.3)$$

Therefore for grid points at the north pole where $\theta = 0$, the above equation is not suitable because the denominator in the last term in left hand side is 0. For the north pole, we go back to use the equation (2.20) in Cartesian coordinate system. The derivatives are evalu-

ated by the following:

$$\frac{\partial \vec{q}}{\partial x} = \frac{1}{r} \frac{\partial \vec{q}}{\partial \theta} \Big|_{\varphi=0}, \quad \frac{\partial \vec{q}}{\partial y} = \frac{1}{r} \frac{\partial \vec{q}}{\partial \theta} \Big|_{\varphi=\pi/2} \quad \text{and} \quad \frac{\partial \vec{q}}{\partial z} = \frac{\partial \vec{q}}{\partial r}$$

where the subscripts denote the directions or planes which are used to evaluate the derivatives. Since the grids are screwed near the north pole, it impose very strict limit on the time step. In the calculation, the values of acoustic variables in first three levels of grid points near the north pole are obtained by third-order accurate interpolations of the values at the pole and the values at the fourth and fifth level of grid points surrounding the pole. By using the properties of symmetry, only the region bounded by $0 \leq \theta \leq \pi/2$ and $0 \leq \varphi \leq \pi$ is needed for the simulation. A grid system of $75 \times 45 \times 60$ points with $\Delta r = 7D/30$, $\Delta \theta = 2^\circ$ and $\Delta \varphi = 3^\circ$ is used. Time step is chosen as 0.001. To run this case in SGI INDY R5000 up to $t = 2.5$, it requires about 11 CPU hours. To accurately evaluate some properties like the pressure history at different points or the directivity for a periodic source with the frequency given in the scattering of waves off a cylinder, grid system of points at least double as many as the points presently used in each direction is needed. Taking into account of the smaller time step required for finer grid, it will need at least about 176 CPU hours, or a week in SGI INDY R5000 for a decent result. Therefore simulating the real life three-dimensional acoustic problems requires the use of super computer. Figure 26 and Figure 27 show the surface plots of pressure patterns on the surface of the sphere and various planes of $x=0$, $y=0$ and $z=0$ at $t=2.5$ computed by the optimized upwind scheme. They clearly demonstrate the radiation waves, reflected waves and the interaction of waves and the sphere. There are not noticeable differences in the wave patterns near the north pole, which validate the treatments for the grid points near the pole.

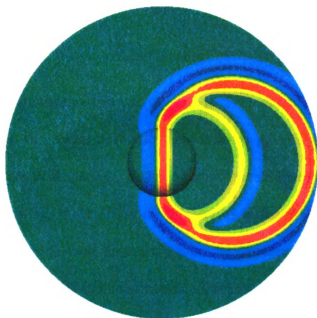


Figure 26 Pressure patterns on the surface of the sphere and the plane of $z = 0$ at $t = 2.5$.

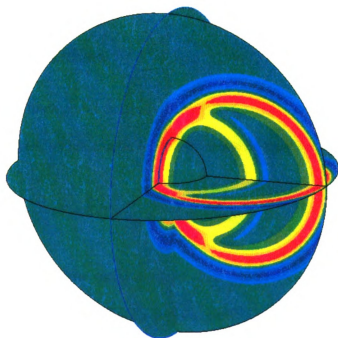


Figure 27 Pressure patterns on the surface of the sphere and the planes of $x=0$, $y=0$ and $z=0$ at $t=2.5$

5 FINITE DIFFERENCE VERSUS FINITE VOLUME DISCRETIZATIONS

Two discretization approaches are widely used in CFD, namely finite difference and finite volume schemes. In a finite difference approach the governing equations are first transformed from the physical space (x, y, z) to a computational space in the general curvilinear coordinate system (ξ, η, ζ) . Then the derivatives in the governing equations are approximated and discretized with finite differences in the computational domain. In a finite volume approach, the grid cells are treated as control volumes, and the governing equations are integrated directly in the control volumes to yield the discretized equations. It can be shown that with proper interpretation of metric terms in a finite difference, the finite difference scheme is identical to a finite volume scheme.

5.1 Navier-Stokes Equations

In this study the three-dimensional unsteady Navier-Stokes equations in Cartesian coordinate system are employed, which can be written in conservation form as the following:

$$\frac{\partial \vec{Q}}{\partial t} + \frac{\partial}{\partial x}(\vec{E} - \vec{E}_v) + \frac{\partial}{\partial y}(\vec{F} - \vec{F}_v) + \frac{\partial}{\partial z}(\vec{G} - \vec{G}_v) = 0 \quad (5.1)$$

where \vec{Q} is the conservative flow variable vector, \vec{E} , \vec{F} and \vec{G} are the inviscid flux vectors in x , y and z directions respectively. \vec{E}_v , \vec{F}_v and \vec{G}_v are viscous flux vectors corresponding to x , y and z directions respectively. In detail, we have

$$\vec{Q} = \begin{Bmatrix} \rho \\ \rho u \\ \rho v \\ \rho w \\ \rho e_t \end{Bmatrix}, \vec{E} = \begin{Bmatrix} \rho u \\ \rho u^2 + p \\ \rho uv \\ \rho uw \\ \rho u \left(e_t + \frac{p}{\rho} \right) \end{Bmatrix}, \vec{F} = \begin{Bmatrix} \rho v \\ \rho uv \\ \rho v^2 + p \\ \rho vw \\ \rho v \left(e_t + \frac{p}{\rho} \right) \end{Bmatrix}, \vec{G} = \begin{Bmatrix} \rho w \\ \rho uw \\ \rho vw \\ \rho w^2 + p \\ \rho w \left(e_t + \frac{p}{\rho} \right) \end{Bmatrix} \quad (5.2)$$

and

$$\vec{E}_v = \begin{Bmatrix} 0 \\ \tau_{xx} \\ \tau_{xy} \\ \tau_{xz} \\ u\tau_{xx} + v\tau_{xy} + w\tau_{xz} - \kappa \frac{\partial T}{\partial x} \end{Bmatrix} \quad (5.3)$$

$$\vec{F}_v = \begin{Bmatrix} 0 \\ \tau_{yx} \\ \tau_{yy} \\ \tau_{yz} \\ u\tau_{yx} + v\tau_{yy} + w\tau_{yz} - \kappa \frac{\partial T}{\partial y} \end{Bmatrix} \quad (5.4)$$

$$\vec{G}_v = \begin{Bmatrix} 0 \\ \tau_{zx} \\ \tau_{zy} \\ \tau_{zz} \\ u\tau_{zx} + v\tau_{zy} + w\tau_{zz} - \kappa \frac{\partial T}{\partial z} \end{Bmatrix} \quad (5.5)$$

where the symbols used here for flow variables have the same meanings as those used in acoustic field equations. The new notations e_t and κ represent the total energy per unit mass and the thermal conductivity. The total energy can be obtained from the expression of $e_t = e + 0.5(u^2 + v^2 + w^2)$. The relations of viscous stresses to the rates of strain, the velocity gradients, are given as the following:

$$\begin{aligned}\tau_{xx} &= -\frac{2}{3}\mu(u_x + v_y + w_z) + 2\mu u_x \\ \tau_{yy} &= -\frac{2}{3}\mu(u_x + v_y + w_z) + 2\mu v_y \\ \tau_{zz} &= -\frac{2}{3}\mu(u_x + v_y + w_z) + 2\mu w_z \\ \tau_{xy} &= \tau_{yx} = \mu(u_y + v_x) \\ \tau_{zx} &= \tau_{xz} = \mu(u_z + w_x) \\ \tau_{yz} &= \tau_{zy} = \mu(v_z + w_y)\end{aligned}$$

Where μ is the dynamic viscosity.

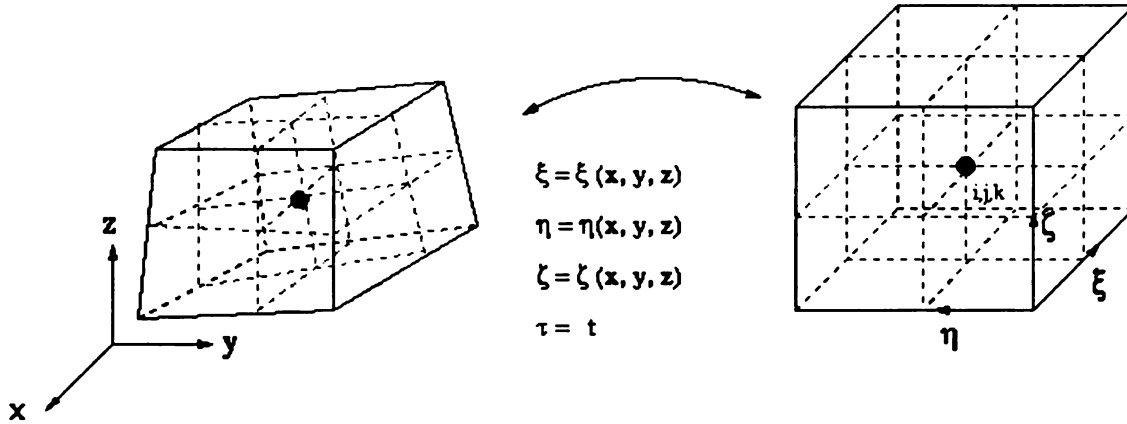


Figure 28 Coordinate transformation and the grid cell around grid point (i, j, k)

The Navier-Stokes equations can be transformed from the physical space (x, y, z, t) to curvilinear space (ξ, η, ζ, τ) shown in Figure 28 and written as the following:

$$\frac{\partial}{\partial \tau} \tilde{Q} + \frac{\partial}{\partial \xi} (\tilde{E} - \tilde{E}_v) + \frac{\partial}{\partial \eta} (\tilde{F} - \tilde{F}_v) + \frac{\partial}{\partial \zeta} (\tilde{G} - \tilde{G}_v) = 0 \quad (5.6)$$

where $\tilde{Q} = J^{-1} \vec{Q}$. Inviscid and viscous flux vectors in the curvilinear coordinates are

$$\tilde{E} = J^{-1} (\vec{E} \xi_x + \vec{F} \xi_y + \vec{G} \xi_z) \quad (5.7)$$

$$\tilde{F} = J^{-1} (\vec{E} \eta_x + \vec{F} \eta_y + \vec{G} \eta_z) \quad (5.8)$$

$$\tilde{G} = J^{-1} (\vec{E} \zeta_x + \vec{F} \zeta_y + \vec{G} \zeta_z) \quad (5.9)$$

$$\tilde{E}_v = J^{-1} (\vec{E}_v \xi_x + \vec{F}_v \xi_y + \vec{G}_v \xi_z) \quad (5.10)$$

$$\tilde{F}_v = J^{-1} (\vec{E}_v \eta_x + \vec{F}_v \eta_y + \vec{G}_v \eta_z) \quad (5.11)$$

$$\tilde{G}_v = J^{-1} (\vec{E}_v \zeta_x + \vec{F}_v \zeta_y + \vec{G}_v \zeta_z) \quad (5.12)$$

Note that the conservation form of Navier-Stokes in the Cartesian coordinates system is preserved after the coordinate transformation. In another word, equation (5.6) is in the conservation form in the general curvilinear coordinate system. J is the determinant of Jacobian matrix of the coordinate transform. In this study only stationary grids are considered. Therefore ξ , η and ζ are functions of x , y and z only. They are not function of time t . The reciprocal of the determinant of the Jacobian matrix of the coordinate transform can be explicitly written as:

$$J^{-1} = x_\xi y_\eta z_\zeta + x_\zeta y_\xi z_\eta + x_\eta y_\zeta z_\xi - x_\xi y_\zeta z_\eta - x_\eta y_\xi z_\zeta - x_\zeta y_\eta z_\xi \quad (5.13)$$

Let \tilde{A} , \tilde{B} and \tilde{C} be the three Jacobian matrices of \tilde{E} , \tilde{F} and \tilde{G} with respect to \tilde{Q} , i.e.,

$$\tilde{A} = \frac{\partial \tilde{E}}{\partial \tilde{Q}} \quad \tilde{B} = \frac{\partial \tilde{F}}{\partial \tilde{Q}} \quad \tilde{C} = \frac{\partial \tilde{G}}{\partial \tilde{Q}} \quad (5.14)$$

Then they can be diagonalized as

$$\tilde{A} = \tilde{T}_\xi \tilde{\Lambda}_\xi \tilde{T}_\xi^{-1} \quad \tilde{B} = \tilde{T}_\eta \tilde{\Lambda}_\eta \tilde{T}_\eta^{-1} \quad \tilde{C} = \tilde{T}_\zeta \tilde{\Lambda}_\zeta \tilde{T}_\zeta^{-1} \quad (5.15)$$

where $\tilde{\Lambda}_\xi$, $\tilde{\Lambda}_\eta$ and $\tilde{\Lambda}_\zeta$ are the diagonal eigenvalue matrices which are the same as those for the acoustic field equations. \tilde{T}_ξ , \tilde{T}_η and \tilde{T}_ζ are the corresponding eigenvector matrices. We should note that \tilde{A} , \tilde{B} , \tilde{C} and \tilde{T}_ξ , \tilde{T}_η , \tilde{T}_ζ are different from those for the acoustic field equations. In the acoustic field equations, we do not consider the conservation forms which are necessary for the computation of the mean flow when the discontinuities like shock wave appear. The detailed formulae of the matrices \tilde{A} , \tilde{B} , \tilde{C} and \tilde{T}_ξ , \tilde{T}_η , \tilde{T}_ζ for the conservative Navier-Stokes equations in the general curvilinear coordinate system can be found in the literatures (Pulliam *et al.*, 1980, Warming *et al.*, 1975, 1978).

5.2 Finite Difference Versus Finite Volume Discretizations

Finite difference approach starts from the differential equation (5.6) and seeks the numerical approximations to the derivatives appearing in the equation. The optimized upwind schemes developed in the study on CAA belong to this approach. For example, the partial derivative in the ξ direction at grid point (i, j, k) can be discretized by a finite difference with up to second order accuracy and written as the following:

$$\frac{\partial}{\partial \xi}(\tilde{E} - \tilde{E}_v) \equiv (\tilde{\tilde{E}} - \tilde{\tilde{E}}_v)_{i+1/2, j, k} - (\tilde{\tilde{E}} - \tilde{\tilde{E}}_v)_{i-1/2, j, k} \quad (5.16)$$

where $\tilde{\tilde{E}}$ and $\tilde{\tilde{E}}_v$ are the finite difference approximations to \tilde{E} and \tilde{E}_v at surface $(i+1/2, j, k)$ respectively. Without loss of the generality we have assumed that the grid sizes $\Delta\xi$, $\Delta\eta$ and $\Delta\zeta$ in the computational domain are all set to 1.

A cell-centered finite volume approach starts from the following integral equation

$$\int_{V_{i,j,k}} \frac{\partial}{\partial t} \vec{Q} dV + \int_S \{n_x(\vec{E} - \vec{E}_v) + n_y(\vec{F} - \vec{F}_v) + n_z(\vec{G} - \vec{G}_v)\} dS = 0 \quad (5.17)$$

where $V_{i,j,k}$ is volume of grid cell with index (i, j, k) and $\vec{n} = (n_x, n_y, n_z)$ is the outward normal vector at the cell surface S . The surface S of cell (i, j, k) shown in Figure 28 is composed of six faces in i, j and k directions, with two faces in each direction. Equation (5.17) can be derived by integrating equation (5.1) over grid cell (i, j, k) or directly from the Navier-Stokes equations in the integral form. Finite volume approach seeks the numerical approximations to the integrations over the cell surfaces. For example, for cell (i, j, k) shown in Figure 28, the integration on surface $(i+1/2, j, k)$ is approximated by

$$\begin{aligned} & \int_S \{n_x(\vec{E} - \vec{E}_v) + n_y(\vec{F} - \vec{F}_v) + n_z(\vec{G} - \vec{G}_v)\} dS \\ & \equiv \{S[n_x(\bar{E} - \bar{E}_v) + n_y(\bar{F} - \bar{F}_v) + n_z(\bar{G} - \bar{G}_v)]\}_{i+1/2, j, k} \end{aligned} \quad (5.18)$$

where \bar{E} and \bar{E}_v are the numerical approximations to \vec{E} and \vec{E}_v at the surface respectively. Similarly \bar{F}, \bar{F}_v and \bar{G}, \bar{G}_v are the approximations to \vec{F}, \vec{F}_v and \vec{G}, \vec{G}_v at the same surface respectively. S in the right hand side of the above equation is the area of the surface.

Refer to Figure 28 and consider the cell surface between the grid points (i, j, k) and $(i+1, j, k)$. In the finite difference approach, the metric terms can be evaluated in the following way,

$$J_{i,j,k}^{-1} = V_{i,j,k} \quad (5.19)$$

$$(J^{-1}\xi_x)_{i+1/2,j,k} = (Sn_x)_{i+1/2,j,k} \quad (5.20)$$

$$(J^{-1}\xi_y)_{i+1/2,j,k} = (Sn_y)_{i+1/2,j,k} \quad (5.21)$$

$$(J^{-1}\xi_z)_{i+1/2,j,k} = (Sn_z)_{i+1/2,j,k} \quad (5.22)$$

Substituting above metrics into equation (5.16), we get

$$(\tilde{E} - \tilde{E}_v)_{i+1/2,j,k} = \{S[n_x(\bar{E} - \bar{E}_v) + n_y(\bar{F} - \bar{F}_v) + n_z(\bar{G} - \bar{G}_v)]\}_{i+1/2,j,k} \quad (5.23)$$

which is the same as the finite volume discretization at the cell surface given in the equation (5.18). For the finite difference approximation at surfaces in other directions, we can similarly show that the finite difference approximation is equivalent to the finite volume approximation provided the grid metrics in the surfaces are evaluated in a way similar to equations (5.19) to (5.22). If the cell shown in Figure 28 is defined as a control volume for grid points (i, j, k) and metric terms are evaluated by formulae given in equations (5.19) to (5.22), then the finite difference approach is identical to a finite volume approach. Although OVERFLOW is a finite difference based code, the metric terms are calculated in a pseudo-finite volume manner. If the control volume for the metric terms around each

finite difference grid point are unambiguously defined in OVERFLOW, the finite difference method in OVERFLOW can be viewed as the same as a cell-centered finite volume method on the control volume mesh. The fully conservative Chimera, which was developed originally based on finite volume scheme, can then be naturally applied to the finite difference scheme and implemented in the OVERFLOW.

5.3 Finite Difference Grid and Finite Volume Grid

As it is mentioned before, the OVERFLOW is a finite difference based code. Therefore the computational grid is interpreted as a finite difference grid. To implement conservative Chimera in the OVERFLOW, the control volume for each finite difference grid point needs to be defined unambiguously and relevant metric terms should be calculated based on the defined volume. Since the information on the patch interfaces and other relevant information between the overlapped grids are needed, an independent module called the Zonal Interface Generator (ZIG) is developed by Wang in CFDRC. The ZIG is also based on a finite volume grid. Therefore another grid, namely the finite volume grid corresponding to the finite difference grid, is required.

In the implementation the given input grid system which is generated by some other codes, for example, CFD-GEOM from CFDRC, is treated as a finite volume grid. The enhanced finite difference grid is then computed as the mutual grid. It is formed by simply connecting all the centroids of control volumes, boundary face centers and the corners. Figure 29 schematically shows the concept in the two-dimensional sense. In such a approach, all the geometric quantities are computed based on the given original finite volume grid which guarantees the accurate representation of geometry configuration. Thus

the given original finite volume grid is input to the conservative interface generator (ZIG) to generate patch interfaces and calculates the relevant information for the conservative Chimera. This grid is also used by OVERFLOW with the conservative Chimera when determining cell volumes, cell face areas and other relevant metric terms. The enhanced finite difference grid is directly input to the OVERFLOW to allocate dynamic memory and to apply boundary conditions.

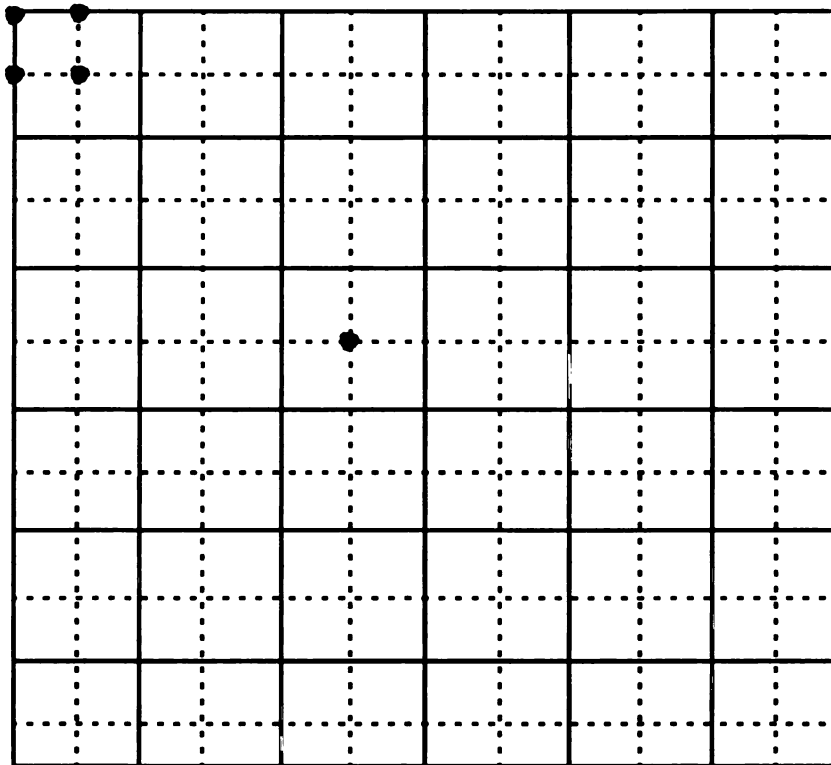


Figure 29 Schematically showing finite volume grid (solid line) and mutual finite difference grid (dash line)

6 IMPLEMENTATION OF CONSERVATIVE CHIMERA IN OVERFLOW

6.1 Review of the Chimera Approach

As it is described in section 1.2 on the background of the Chimera, there are many blocks in the computational domain. The grids in the neighboring zones are overlapped and the information for variable values in the neighboring zones is needed to exchange. Figure 30 schematically shows overlapped grids in two neighboring zones in two-dimensional sense. As it is shown in the figure, the boundary of one grid intersects with the interior cells of the other grid. They are usually referred as the minor and major grids as it is indicated in Figure 30. A grid can be a minor grid of several major grids. Reversely, a grid can be a major grid of several minor grids. The boundaries of the minor grids which cut into the interior cells of major grids usually form the patch interfaces.

In the traditional Chimera approach, for each cell near the patch interfaces in the minor grid, the interior cells in the major grid surrounding the cell in the minor grid near the patch interfaces are first located. The values of flow variables in the cell in the minor grid are obtained by the interpolation of the values of flow variables in the surrounding cells in the major grid. The values in the cell *R* in the minor grid in Figure 30, for example, may be obtained from the values in cells enclosed by the rectangle indicated by the thick lines in the major grid through the interpolation. The required number of surrounding cells depends on the required accuracy of the interpolation. The fluxes flowing into the minor grid through the patch interfaces may not be in the same amount as those flowing out of

are cut from regular cell faces 1-2 and 2-3 by the patch interfaces are referred as cut faces. The cell surfaces for the cell in the minor grid near the patch interface are also cut into smaller faces by the cut cells in the major grid. For cell R in the minor grid in Figure 30, for example, its cell surface labeled with $a-d$ is divided into smaller faces $a-b$, $b-c$ and $c-d$ which are referred as the smallest faces. With the finite volume approach the net fluxes through a cell are the sum of numerical fluxes through cell faces. Therefore in order to preserve the conservation globally, the amount of the fluxes flowing into the minor grid and flowing out of the major grid through the patch interfaces must be the same. Wang *et al* (1994) proposed to let the contributions of the fluxes on the smallest faces to the major grid and minor grid be exactly the same. Refer to the smallest face $b-c$, we add the amount of fluxes on the smallest face to the net fluxes of its left cell L and subtract the same amount of fluxes from the net fluxes of its right cell R . The remaining problem is how to numerically evaluate the fluxes on the smallest faces and cut faces with the desired accuracy which is usually of second order in CFD.

6.2 Numerical Fluxes through the Patch Interface

Since the enhanced finite difference grid is constructed based on the given finite volume grid, a control volume for each finite difference grid point is precisely defined. The metric terms for each finite difference grid point are calculated based on the control volume for that point, which are calculated exactly in the way shown in section 5.2. In the major grid, the cut face areas in each cut cell and each hole cell are assigned to zero first. Then the actual cut face areas and the actual volume in the each cut cell are updated using the information generated by the module of ZIG. From equation (5.18) for the finite vol-

ume approach or equation (5.23) for finite difference approach with the grid metrics computed as those illustrated in section 5.2, the amount of fluxes in cell surfaces are proportional to the areas of the surfaces. Therefore the correct amount of fluxes through the cut faces in each cut cell is automatically calculated in the OVERFLOW, and the fluxes through hole cell faces are zero because of zero face area assigned at the beginning. For the cut cell L in the major grid shown in Figure 30, for example, the fluxes through the cell face $1-2$ is equivalent to the fluxes through the cut face $1-b$. Thus the total fluxes out of this cell calculated in the OVERFLOW, the sum of the fluxes through four cell faces $1-2$, $2-3$, $3-4$ and $4-1$, are just the sum of fluxes through cut faces $1-b$, $c-3$ and normal faces $3-4$, $4-1$. In the minor grid, the areas of the cell faces corresponding to the patch boundary, the face $a-d$ in the cell R shown in Figure 30, for example, are also set to zero at beginning. The total net fluxes out of the cell R obtained in the OVERFLOW are the total fluxes through $a-f$, $f-e$ and $e-d$.

Therefore the remaining work to correctly compute the net fluxes out the cut cell L is to evaluate the numerical fluxes out of the cut cell through the smallest face $b-c$. The remaining work to correctly compute the net fluxes out the cell R is to evaluate the numerical fluxes out of the cut cell through cell face $a-d$ which consist of the fluxes out the cell R through the smallest faces $a-b$, $b-c$ and $c-d$. To achieve flux conservation for the overlapping Chimera grids, the same amount of fluxes across each smallest face with different signs are added to the total net fluxes for the cells sharing this face in both the major and the minor grids. Refer to the smallest face $b-c$, let $\tilde{\mathcal{F}}_{bc}$ be the numerical fluxes through the smallest face $b-c$ with the face normal pointing to the cell R as it is shown in Figure 30. $\tilde{\mathcal{F}}_{bc}$ is added to the net fluxes of cut cell L computed from the OVERFLOW and $-\tilde{\mathcal{F}}_{bc}$ is

added to the net fluxes of cell R computed from the OVERFLOW. Therefore to implement the fully conservative chimera, the remaining work is to evaluate the numerical fluxes on all smallest faces like $b-c$. The computation of the fluxes through each smallest face is done separately in the implementation of the fully conservative Chimera in OVERFLOW.

Consider the smallest face $b-c$ shown in Figure 30. Let \vec{Q}_L be the variable vector at the center of cut cell L and \vec{Q}_R be the variable vector at the center of the right cell R . Then the inviscid fluxes through the smallest face $b-c$ is determined by Roe's Riemann solver (Roe, 1983). To be more specific, denote

$$\tilde{\mathcal{F}}(\vec{Q}_L, \vec{n}) = S[n_x \vec{E}(\vec{Q}_L) + n_y \vec{F}(\vec{Q}_L) + n_z \vec{G}(\vec{Q}_L)] \quad (6.1)$$

$$\tilde{\mathcal{F}}(\vec{Q}_R, \vec{n}) = S[n_x \vec{E}(\vec{Q}_R) + n_y \vec{F}(\vec{Q}_R) + n_z \vec{G}(\vec{Q}_R)] \quad (6.2)$$

$$\mathcal{A}(\vec{Q}_a, \vec{n}) = S[n_x A(\vec{Q}_a) + n_y B(\vec{Q}_a) + n_z C(\vec{Q}_a)] \quad (6.3)$$

where S is the area of the smallest face $b-c$ (the arc length in two-dimension), \vec{Q}_a is the Roe's average of \vec{Q}_L and \vec{Q}_R , Jacobian matrices of the fluxes A , B and C are

$$A = \frac{\partial \vec{E}}{\partial \vec{Q}} \quad B = \frac{\partial \vec{F}}{\partial \vec{Q}} \quad C = \frac{\partial \vec{G}}{\partial \vec{Q}}$$

The inviscid fluxes through the smallest face $b-c$ are approximated by the following

$$\int_S \{n_x \vec{E} + n_y \vec{F} + n_z \vec{G}\} dS \approx \tilde{\mathcal{F}}_{bc} = \frac{1}{2} [\mathcal{F}(\vec{Q}_L, \vec{n}) + \mathcal{F}(\vec{Q}_R, \vec{n}) - |\mathcal{A}(\vec{Q}_a, \vec{n})| (\vec{Q}_R - \vec{Q}_L)] \quad (6.4)$$

where $|A| = T|\Lambda|T^{-1}$ with T the eigenvector matrix, Λ the diagonal eigenvalue matrix.

The convention for the absolute value of a diagonal matrix is the same as it is defined for

the acoustic field equations.

Refer to Figure 30 again. To calculate the viscous fluxes through the smallest face $b-c$, the following integral is evaluated

$$\int_S \{n_x \vec{E}_v + n_y \vec{F}_v + n_z \vec{G}_v\} dS \cong S[n_x \bar{E}_v + n_y \bar{F}_v + n_z \bar{G}_v] \quad (6.5)$$

Viscous fluxes \vec{E}_v , \vec{F}_v and \vec{G}_v consist of laminar and turbulent eddy viscosities, flow variables and velocity and temperature gradients ∇u , ∇v , ∇w and ∇T . All quantities on the smallest face $b-c$ in the viscous fluxes except for the velocity and temperature gradients are calculated as the average of the quantities in the cut cell L and the cell R . The key to evaluate the viscous fluxes through face $b-c$ is to find the gradients of u , v , w and T on that face. The thin layer approximation is used in calculating the flow gradients on face $b-c$. More specifically, under such an approximation, we have

$$(\nabla u)_{bc} = \frac{\partial u}{\partial n} \hat{n} \quad (6.6a)$$

$$(\nabla v)_{bc} = \frac{\partial v}{\partial n} \hat{n} \quad (6.6b)$$

$$(\nabla w)_{bc} = \frac{\partial w}{\partial n} \hat{n} \quad (6.6c)$$

$$(\nabla T)_{bc} = \frac{\partial T}{\partial n} \hat{n} \quad (6.6d)$$

In another word, we assume that the flow variables do not change along the surfaces. This approximation is usually applied in evaluating the gradients on surface when the schemes

up to second order are employed. Let us only consider velocity u in x -direction to illustrate the procedure of evaluating the gradients. Neglect second order and higher order terms in the Taylor expansion, we have

$$(u_R - u_L) \cong (\nabla u)_{bc} \cdot (\vec{r}_R - \vec{r}_L) \quad (6.7)$$

Where $\vec{r}_L = (x_L, y_L, z_L)$ and $\vec{r}_R = (x_R, y_R, z_R)$ are the position vectors in the cell centers of the cut cell L and the cell R respectively. u_L and u_R are values of u evaluated at the cell center of the cut cell L and the cell R respectively, which are both available at the current time stage. Substituting equation (6.6a) into equation (6.7), we obtain

$$\frac{\partial u}{\partial n} = \frac{u_R - u_L}{\vec{n} \cdot (\vec{r}_R - \vec{r}_L)} \quad (6.8)$$

Substituting equation (6.8) back into equation (6.6a), we get the gradient of u on face b - c as the following

$$(\nabla u)_{bc} = \frac{(u_R - u_L)\vec{n}}{\vec{n} \cdot (\vec{r}_R - \vec{r}_L)} \quad (6.9)$$

∇v , ∇w and ∇T can be evaluated in the same way.

Since the cell cutting in the ZIG is arbitrary, the direction of $\vec{r}_R - \vec{r}_L$ may be far away from the direction \vec{n} . The angle between \vec{n} and $\vec{r}_R - \vec{r}_L$ may even be greater than 90 degree, i.e. $\vec{n} \cdot (\vec{r}_R - \vec{r}_L)$ is negative in some extreme cases. Then the velocity gradients derived in equation (6.9) can produce large errors. In these cases we assume that the velocity gradients are in the direction of $(\vec{r}_R - \vec{r}_L)$, i.e. the assumption in equation (6.6a) is

replaced by

$$(\nabla u)_{bc} = |(\nabla u)_{bc}| \frac{(\vec{r}_R - \vec{r}_L)}{|\vec{r}_R - \vec{r}_L|} \quad (6.10)$$

Repeating the procedures of deriving the gradients, we now have

$$(\nabla u)_{bc} = \frac{(u_L - u_R)(\vec{r}_R - \vec{r}_L)}{|\vec{r}_R - \vec{r}_L|^2} \quad \text{if} \quad \vec{n} \cdot (\vec{r}_R - \vec{r}_L) \leq 0 \quad (6.11)$$

This special treatment is found to be necessary for boosting the stability and work very satisfactorily in the tests which are shown in next chapter.

6.3 Implicit Treatment of the Patch Interface

Since a finite difference scheme can be identical to a finite volume scheme, in this section we are using the finite difference approach to illustrate the implicit treatment of the patch interface for convenience. After the spatial derivatives are approximated by the finite differences, equation (5.6) in grid point (i, j, k) becomes

$$\left(\frac{\partial}{\partial t} \tilde{Q} \right)_{i,j,k} = -\vec{R}_{i,j,k} \quad (6.12)$$

where the right hand side of the above equation can be formally written as

$$\begin{aligned} \vec{R}_{i,j,k} = & (\vec{E} - \vec{E}_v)_{i+1/2,j,k} - (\vec{E} - \vec{E}_v)_{i-1/2,j,k} \\ & + (\vec{F} - \vec{F}_v)_{i+1/2,j,k} - (\vec{F} - \vec{F}_v)_{i-1/2,j,k} \\ & + (\vec{G} - \vec{G}_v)_{i+1/2,j,k} - (\vec{G} - \vec{G}_v)_{i-1/2,j,k} \end{aligned} \quad (6.13)$$

The notations associated to the fluxes in the ξ direction are the same as they are defined in section 5.2. The notations associated to the fluxes in the other directions are defined similarly. $\tilde{\tilde{F}}$ and $\tilde{\tilde{F}}_v$ are the finite difference approximation to \tilde{F} and \tilde{F}_v respectively. $\tilde{\tilde{G}}$ and $\tilde{\tilde{G}}_v$ are the finite difference approximation to \tilde{G} and \tilde{G}_v respectively. From now on, whenever the meanings are clear, we will omit the subscripts and superscripts for simplicity. Since only the steady flow is interesting in this study, considering first order accurate backward finite difference for the time derivative in equation (6.12). we obtain

$$\tilde{Q}^{n+1} - \tilde{Q}^n = -\Delta t \vec{R}^{n+1} = -\Delta t \vec{R}^n - \Delta t (\vec{R}^{n+1} - \vec{R}^n) \quad (6.14)$$

Now utilizing

$$\vec{R}^{n+1} - \vec{R}^n = \vec{R}(\tilde{Q}^{n+1}) - \vec{R}(\tilde{Q}^n) \approx \left. \frac{\partial \vec{R}}{\partial \tilde{Q}} \right|_{\tilde{Q}^n} (\tilde{Q}^{n+1} - \tilde{Q}^n) \quad (6.15)$$

we have

$$\left(I + \Delta t \frac{\partial \vec{R}}{\partial \tilde{Q}} \right) \Delta \tilde{Q} = -\Delta t \vec{R}^n \quad (6.16)$$

where I is the identity matrix and $\Delta \tilde{Q} = \tilde{Q}^{n+1} - \tilde{Q}^n$. Since only steady flow is considered, the left hand side of above equation is not necessary to be high order accurate. As it is seen that $\Delta \tilde{Q}$ approaches to zero as the flow approaches to the steady state. Therefore the left hand side (LHS) vanishes when the steady state reaches. The important thing is to find an approximation matrix to $\partial \vec{R} / \partial \tilde{Q}$ so that the resulted linear algebraic equation

(6.16) can be easily solved while the matrix greatly boosts the stability and convergence rate. One method implemented in the OVERFLOW is to use the central difference for \vec{R} in the left hand side of equation (6.16) to get the approximation matrix. Let us consider inviscid flows here for easy illustration, notice that

$$\tilde{E}(\tilde{Q}^{n+1}) - \tilde{E}(\tilde{Q}^n) \approx \left. \frac{\partial \tilde{E}}{\partial \tilde{Q}} \right|_{\tilde{Q}^n} \Delta \tilde{Q} = \tilde{A}^n \Delta \tilde{Q} \quad (6.17a)$$

$$\tilde{F}(\tilde{Q}^{n+1}) - \tilde{F}(\tilde{Q}^n) \approx \left. \frac{\partial \tilde{F}}{\partial \tilde{Q}} \right|_{\tilde{Q}^n} \Delta \tilde{Q} = \tilde{B}^n \Delta \tilde{Q} \quad (6.17b)$$

$$\tilde{G}(\tilde{Q}^{n+1}) - \tilde{G}(\tilde{Q}^n) \approx \left. \frac{\partial \tilde{G}}{\partial \tilde{Q}} \right|_{\tilde{Q}^n} \Delta \tilde{Q} = \tilde{C}^n \Delta \tilde{Q} \quad (6.17c)$$

We have

$$[I + \Delta t(\delta_\xi \tilde{A}^n + \delta_\eta \tilde{B}^n + \delta_\zeta \tilde{C}^n)] \Delta \tilde{Q} = -\Delta t \vec{R}^n \quad (6.18)$$

where δ_ξ , δ_η and δ_ζ are the central difference operators in ξ , η and ζ directions respectively. More specifically, the results of the operation of the central difference operator δ_ξ in ξ direction on $\tilde{A} \Delta \tilde{Q}$ at grid point (i, j, k) can be written as

$$\delta_\xi(\tilde{A} \Delta \tilde{Q}) = \frac{1}{2}[\tilde{A}_{i+1/2, j, k} \Delta \tilde{Q}_{i+1, j, k} - \tilde{A}_{i-1/2, j, k} \Delta \tilde{Q}_{i+1, j, k}] \quad (6.19)$$

Where $\tilde{A}_{i+1/2, j, k}$ is \tilde{A} evaluated at $\tilde{Q}_{i+1/2, j, k}$ which is some kind of average of $\tilde{Q}_{i, j, k}$ and $\tilde{Q}_{i+1, j, k}$ at the surface $(i+1/2, j, k)$. The linear system of algebraic equation (6.18), however, is not easy to solve. It involves 3 grid points in each of ξ , η and ζ directions.

Combining all grid points together, we need to solve linear system of 7-band diagonal block matrices. Each block is a 5×5 matrix in three-dimension and a 4×4 matrix in two-dimension. It will require huge amount of computational time. The splitting technique is used to reduce to computational work in solving the linear system. Equation (6.18) is split as

$$(I + \Delta t \delta_\xi \tilde{A}^n)(I + \Delta t \delta_\eta \tilde{B}^n)(I + \Delta t \delta_\zeta \tilde{C}^n) \Delta \tilde{Q} = -\Delta t \vec{R}^n \quad (6.20)$$

The above equation requires solving the linear algebraic system of tri-diagonal block matrix in each direction, which greatly reduced the computational work. Using the properties of Jacobian matrices in equation (5.15), we can approximately write equation (6.20) as

$$\tilde{T}_\xi(I + \Delta t \delta_\xi \tilde{\Lambda}_\xi) \tilde{T}_\xi^{-1} \tilde{T}_\eta(I + \Delta t \delta_\eta \tilde{\Lambda}_\eta) \tilde{T}_\eta^{-1} \tilde{T}_\zeta(I + \Delta t \delta_\zeta \tilde{\Lambda}_\zeta) \tilde{T}_\zeta^{-1} \Delta \tilde{Q} = -\Delta t \vec{R}^n \quad (6.21)$$

Now the each block is only a diagonal matrix instead of a 5×5 or a 4×4 matrix. As a matter a fact, it requires to solve tri-diagonal system of equations in each direction which can be easily and effectively solved by the special algorithm developed for tri-diagonal system of equations. If the viscosity terms are considered and smoothing terms for stability are added, then equation (6.21) is replaced by (Pulliam *et al.*, 1980)

$$\begin{aligned} & \tilde{T}_\xi(I + \Delta t \delta_\xi \tilde{\Lambda}_\xi + \text{VIS}_\xi + \text{SMO}_\xi) \tilde{T}_\xi^{-1} \tilde{T}_\eta \\ & (I + \Delta t \delta_\eta \tilde{\Lambda}_\eta + \text{VIS}_\eta + \text{SMO}_\eta) \tilde{T}_\eta^{-1} \tilde{T}_\zeta^n \\ & (I + \Delta t \delta_\zeta \tilde{\Lambda}_\zeta + \text{VIS}_\zeta + \text{SMO}_\zeta) \tilde{T}_\zeta^{-1} \Delta \tilde{Q} = -\Delta t \vec{R}^n \end{aligned} \quad (6.22)$$

This is so called the diagonal approximate factorization algorithm implemented in the

OVERFLOW as one method to march the solution to steady state. The viscous terms and the smoothing terms can be respectively written as

$$\text{VIS}_\xi = \Delta t \nabla_\xi \Delta_\xi (\mu_L + \mu_T) (\xi_x^2 + \xi_y^2 + \xi_z^2) I \quad (6.23)$$

$$\text{SMO}_\xi = \Delta t [-\nabla_\xi \Delta_\xi \epsilon_2 + (\nabla_\xi \Delta_\xi)^2 \epsilon_4] I \quad (6.24)$$

Where μ_L and μ_T are the laminar viscosity and turbulence eddy viscosity, Δ_ξ and ∇_ξ are forward and backward-difference operators, e.g.

$$\Delta_\xi \tilde{Q}_{i,j,k} = \tilde{Q}_{i+1,j,k} - \tilde{Q}_{i,j,k}$$

$$\nabla_\xi \tilde{Q}_{i,j,k} = \tilde{Q}_{i,j,k} - \tilde{Q}_{i-1,j,k}$$

ϵ_2 and ϵ_4 are the second order and the fourth order dissipation coefficients. The second order dissipation coefficient is proportional to the maximum of absolute eigenvalues. We should note here that $\Delta\xi$, $\Delta\eta$ and $\Delta\zeta$ have been set to 1 for convenience.

Without any special treatment in OVERFLOW, flux Jacobians on the smallest faces are not included in the LHS implicit operator, although the flux Jacobians on cut faces are actually calculated correctly. Since the cutting in the zonal interface generator (ZIG) is arbitrary, the LHS contributions from the patch interface may be dominant compared to those on the cut faces for certain cut cells. The neglect of these dominant contributions can cause severe convergence problems in some extreme cases. Since the central difference of the inviscid flux Jacobian $\delta\tilde{\Lambda}$ does not contribute to the diagonal matrix, only the Jacobian contributions of the smallest face due to the viscous terms and the smoothing terms need to consider.

Refer to the Figure 30 again. Consider cell L and the smallest face $b-c$. The three com-

ponents n_ξ , n_η and n_ζ of face normal \vec{n} in the curvilinear coordinates ξ , η and ζ are calculated, i.e $\vec{n} = (n_\xi, n_\eta, n_\zeta)$. Then by analogy to equations (6.23) and (6.24) for viscosity contribution and smoothing terms for a normal cell, and noticing that grid metrics in equations (5.19) to (5.22), the contributions of the flux Jacobians of smallest face b - c due to the viscous term and smoothing term to cell L in the direction ξ are calculated respectively as the following:

$$(\text{VIS}_\xi)_{bc} = \frac{\Delta t(\mu_L + \mu_T)_L S_{bc}^2}{\rho_L V_L^2} \cdot n_\xi I \quad (6.25)$$

$$(\text{SMO}_\xi)_{bc} = \frac{\Delta t(|u_L n_x + v_L n_y + w_L n_z| + c_L) S_{bc}}{2 V_L} \cdot n_\xi I \quad (6.26)$$

where c is the speed of sound, V is the cell volume, S_{bc} is the area of the smallest face b - c . The subscript L means that the values of the variable are evaluated at the center of cut cell L . $(\text{VIS}_\xi)_{bc}$ and $(\text{SMO}_\xi)_{bc}$ are added respectively to VIS_ξ and SMO_ξ in the LHS of the diagonal approximate-factorization algorithm (6.22) in the OVERFLOW for cell L . Note that there are no finite difference operators in the expressions $(\text{VIS}_\xi)_{bc}$ and $(\text{SMO}_\xi)_{bc}$, which means that these two expressions are only added to the diagonal matrix in the LHS of the implicit operator. The contributions of the smallest face b - c in other directions to cell L and the contributions to cell R are similarly evaluated and added.

7 VALIDATION OF THE FULLY CONSERVATIVE CHIMERA IN OVERFLOW

The purpose of the validation cases is to verify the basic implementation of the conservative Chimera in OVERFLOW including mutual grid systems, inviscid and viscous numerical fluxes through the patch interface, special treatment in evaluating velocity gradients at the patch interface and implicit treatment of the patch interface. When the data generated by the ZIG is read in by the OVERFLOW, the test of free stream preservation is used for error checking. All cases presented here passed this test.

7.1 Transonic Flow Through a Channel with a 10% Bump

This case has been widely used in the literature to test compressible flow solver in capturing shock waves. It is selected in this study to validate the implementation of the conservative Chimera in the OVERFLOW. The width of the channel is equal to the length of the bump and the channel length is three times as long as the length of the bump. For the inlet Mach number 0.675, a shock wave is generated over the bump. Two-zonal overlapped grids as shown in the Figure 31 are used in the testing. This two dimensional case is actually run three-dimensionally on purpose to test the inviscid implementation of conservative Chimera in OVERFLOW. In the OVERFLOW two-dimensional flow is run three-dimensionally with no flow in z -direction and grid points in that direction are set to be minimum required by OVERFLOW.

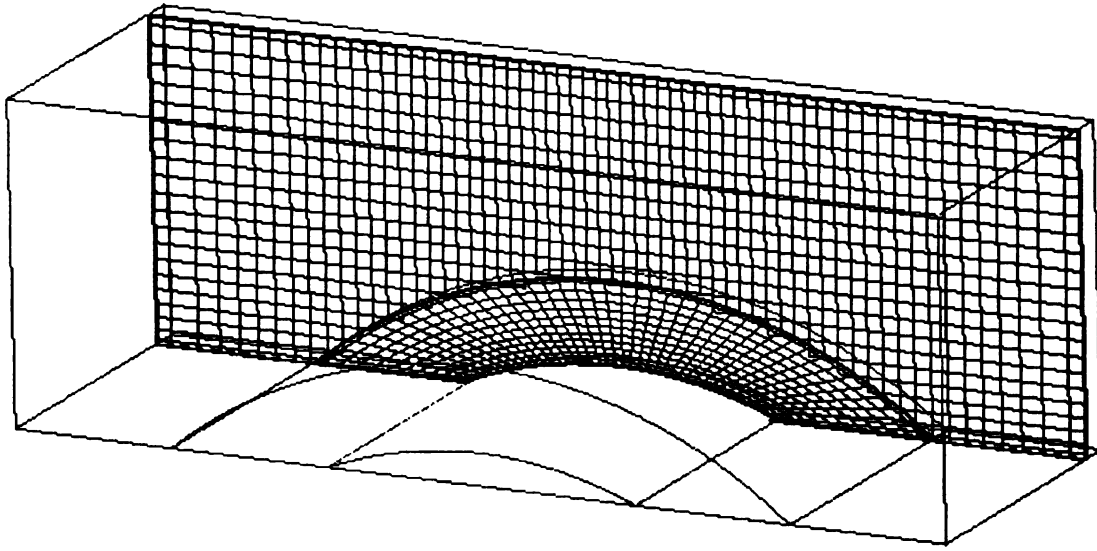


Figure 31 Two-zonal overlapped grid system for the transonic flow over a 10% bump

Figure 32 shows pressure contours in one section computed by OVERFLOW with the conservative Chimera. The contours across the patch interface appear smooth and the shock wave are captured well. OVERFLOW with the original Chimera is also run for this case. All the conditions such as the CFL number, smoothing coefficients, etc., are set to be the same as those in the run with the conservative Chimera. Figure 33 shows the pressure contours computed by OVERFLOW with the original Chimera. The pressure contours in the Figure 32 and Figure 33 agree well with each other. The comparison of the pressure distributions on the lower wall of the channel computed with the conservative Chimera and the original Chimera is displayed in Figure 34. The pressure distributions also agree well with each other in general, although the pressure with the conservative Chimera has better minimum values. Figure 35 shows the convergence histories for the both runs. Due to the appearance of the irregular cut cells near the patch boundaries and the resultant

smaller local time steps, the convergence rate with the conservative Chimera is a little slower than that with the original Chimera.

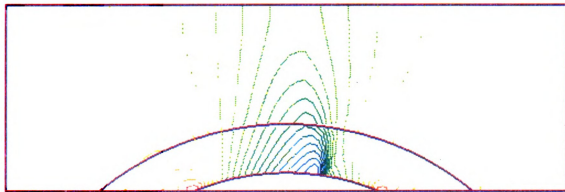


Figure 32 Pressure contours computed using OVERFLOW with the conservative Chimera

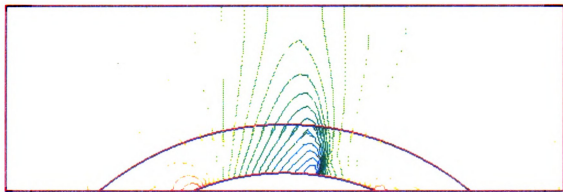


Figure 33 Pressure contours computed using OVERFLOW with the original Chimera

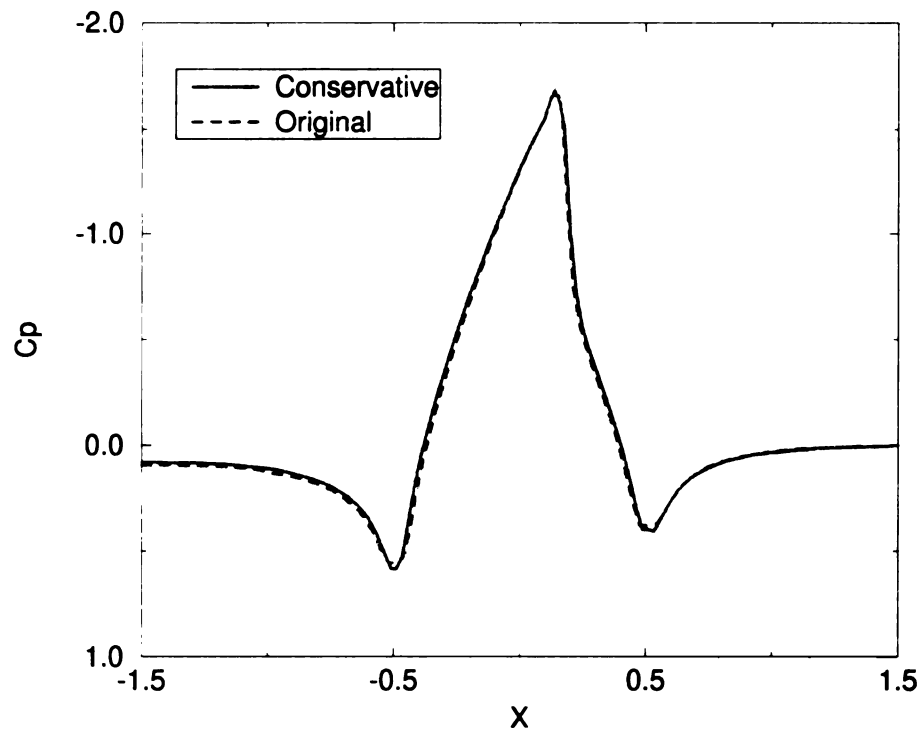


Figure 34 Comparison of pressure coefficients profiles on lower wall of the channel

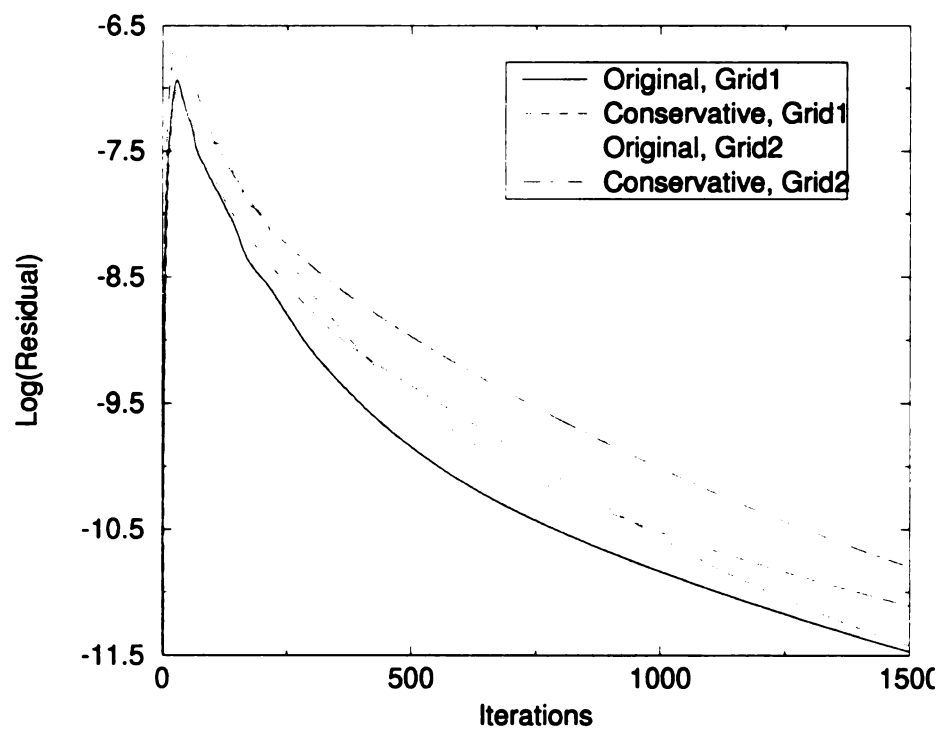


Figure 35 Comparison of convergence histories in using OVERFLOW with the conservative Chimera and the original Chimera

Local grid refinement is used to increase the resolution of the shock wave. An extra zone and grid associated to the zone which refined the major grid are automatically generated in the ZIG based on user specifications for the location of grid refinement and the refinement factors. Figure 36 shows the computational grids after the local refinement. The ZIG also computes the interface patch information required for the conservative Chimera in the OVERFLOW. Figure 37 shows the pressure contours in one section obtained by OVERFLOW with the local refinement. Compared with the pressure contours in Figure 32, the contours shown in Figure 37 display an improved shock wave in the refinement zone.

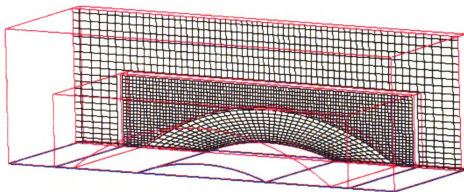


Figure 36 Grids after local refinement for the simulation of flow over a bump by OVERFLOW with the conservative Chimera

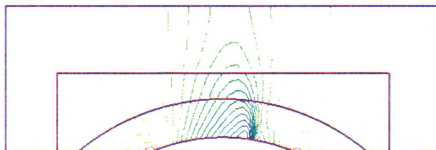


Figure 37 Pressure contours computed by OVERFLOW with the conservative Chimera and with local grid refinement

7.2 Laminar and Turbulent Boundary Layers over a Flat Plane

The flat plane boundary layer problem is used to validate the implementation of viscous fluxes on the patch interface of the conservative Chimera in OVERFLOW. Figure 38 shows the two-grid system used in the testing, namely the major grid and the minor grid. The major grid is the one filling the whole flow field over the flat plane, which is plot in black. The minor grid is the one contained in the major grid shown in red lines in the figure. The lower boundary of the minor grid is constructed such that it extends well into the boundary layer of the flat plate. Hence the patch interface will be within the boundary layer. Since the velocity changes rapidly inside the boundary layer, the correct evaluation of velocity gradients, e.g. $\frac{\partial u}{\partial y}$, is very important. Therefore this case is a good test for the method illustrated in the sections 6.2 and 6.3. Our objective is to observe the smooth variation of streamwise velocity u in boundary layer across the patch interfaces.

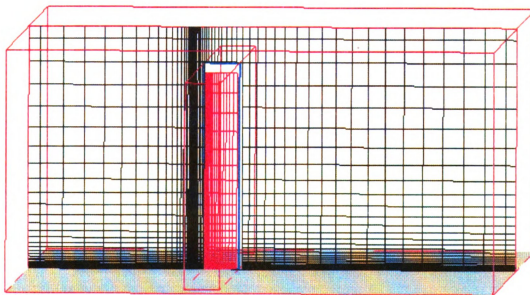


Figure 38 Grids for the study of boundary layer growth over a flat plane

Free stream Mach number is 0.2 and free stream Reynolds number is 10^6 . OVERFLOW with conservative Chimera is run for both laminar flow and turbulent flow with Baldwin-Lomax turbulence model. The boundary conditions for the first several levels of the grid points on the plane from the inlet are set to inviscid adiabatic walls. Figure 39 and Figure 40 show the velocity component in the free stream direction near the region where the boundary layer enter the minor grid for turbulent and the laminar flows respectively. There are gaps between the major and the minor grids shown in the figures because cut cells in the major grid are not drawn in the post processing. As it can be seen, the variation is smooth and the solution is identical to the single grid solution before the patch interface. Figure 41 and Figure 42 shows similar contours near the region where the boundary layer crosses the patch interface for the turbulent and laminar flows, from the minor to the major grid this time. Again, the solution variation across the interface is predicted correctly.

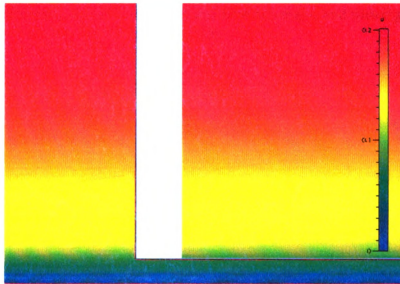


Figure 39 Velocity distributions cross interfaces between major and minor grids inside the turbulent boundary layer over a flat plane

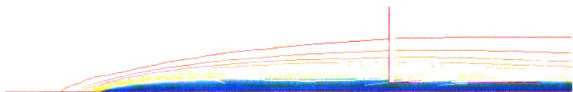


Figure 40 Velocity contours cross interfaces between major and minor grids inside the laminar boundary layer over a flat plane

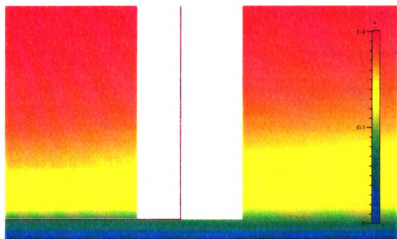


Figure 41 Velocity contours cross interfaces between major and minor grids inside the turbulent boundary layer over a flat plane

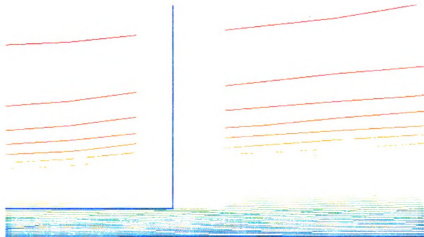


Figure 42 Velocity contours cross interfaces between major and minor grids inside the laminar boundary layer over a flat plane

7.3 Grid Refinement Study with Turbulent Flow over a Two-Element Airfoil

It is well known that non-conservative numerical discretizations will introduce errors, especially in the presence of discontinuity. Wang (1995) compared the computed solutions using conservative and non-conservative Chimera and clearly demonstrated the superiority of the conservative scheme in the presence of discontinuities. Here the case of subsonic turbulent flow over a two-element airfoil is used to demonstrate that the conservative interface scheme also has advantages over the non-conservative counterpart even without the presence of a discontinuity. In this demonstration case three progressively refined grids, namely coarse grid, medium grid and fine grid were used to study the variation of loading on the surfaces of the airfoils. The two-dimensional grids around the main airfoil and the rear airfoil were generated separately. To use the OVERFLOW for the simulation of two-dimensional problems, three planes in the spanwise direction are needed for the original Chimera, which is constructed by stacking two-dimensional grids in the spanwise direction. This three-dimensional grid is also the finite volume grid for the conservative Chimera. Then the enhanced finite difference grid which has one more plane in the spanwise direction are needed and generated by a preprocessor for the conservative Chimera. The coarse grid used in this study is shown in Figure 43. The Chimera holes for the conservative and the original Chimera are displayed in Figure 44 and Figure 45 respectively. It is seen the interfaces are generated such that the shear layer of the main airfoil stays within the same grid. This is done in the ZIG by specifying the first grid line around the airfoil as a solid wall instead of C-cut interface. The the ZIG automatically backs off the patch interface from the solid wall.

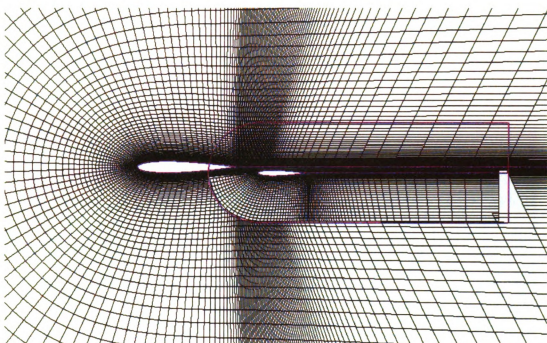


Figure 43 The coarse grid for the turbulent flow over the two-element airfoil

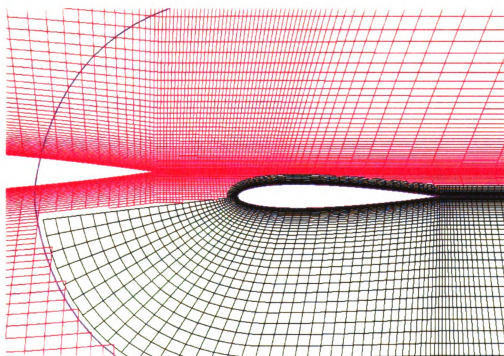


Figure 44 Patch interface for the conservative Chimera in the coarse grid

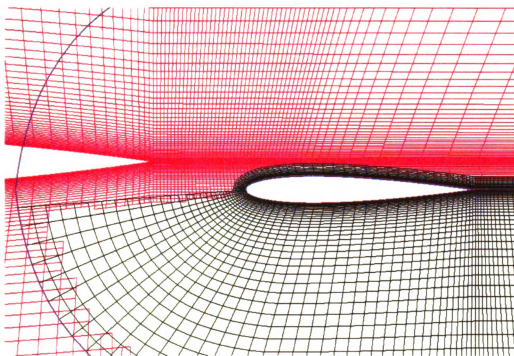


Figure 45 Holes cut for the original Chimera in the coarse grid

Flow conditions are set as the following: free stream Mach number 0.4, angle of attack 2.26° and free stream Reynolds number based on free stream velocity and main airfoil chord length 0.9×10^7 . Baldwin-Lomax boundary layer model is used in the direction normal to the surfaces of the airfoils and the Baldwin-Lomax shear layer model is used in the direction normal to the C-cuts. In the other two directions, inviscid flow is assumed. OVERFLOW with both the conservative Chimera and the original Chimera are run for this case. All the conditions, such as CFL number, time steps, numerical methods and smoothing coefficients etc., for both runs of OVERFLOW with the conservative and the original Chimera are set to be exactly same. The CPU time for each time step with the conservative Chimera is about twice as much as that with the original Chimera. This is because four planes in the spanwise direction are supplied for the conservative Chimera, while only

three planes are needed for the original Chimera. In two-dimensional simulation, flows on the first and the last planes in spanwise direction are not computed. Therefore for the original Chimera in two-dimensional simulation, only flows on one plane are actually computed. For the conservative Chimera, flows on two planes are computed, and additional calculations and memory units are required for the fluxes on the patch interfaces.

Figure 46 and Figure 47 show the Mach contours around the two-element airfoil simulated by OVEFFLOW with the conservative Chimera and the original Chimera in the fine grid respectively. Figure 48 and Figure 49 show the pressure contours with the conservative and the original Chimera in the fine grid. The fine grid around the main airfoil is of dimension 482×162 and the fine grid for the rear airfoil has 242×62 grid points, which is about twice in each direction as fine as the coarse grid shown in Figure 43. On this fine grid Mach and pressure contours obtained with different Chimera treatment are shown to agree well with each other. The contour lines are seen to smoothly cross the patch interfaces. The boundary layers growing along the airfoils and the interaction of the shear layers in the wake of the front airfoil and the flow along the rear airfoil are clearly shown. Figure 50 shows the convergence histories. It is shown the convergence rates with different Chimera approaches are about same. Figure 51 shows the comparison of pressure distributions along the two-element airfoil obtained with the conservative and original Chimera on three different grids. Figure 52 shows the comparison on just the rear airfoil. It is shown that the C_p profile obtained with the conservative Chimera on the fine grid agrees well with that obtained with original Chimera on the same grid. On the coarser grids (coarse grid and medium grid) the conservative Chimera, however, yielded significantly better results than the original Chimera.

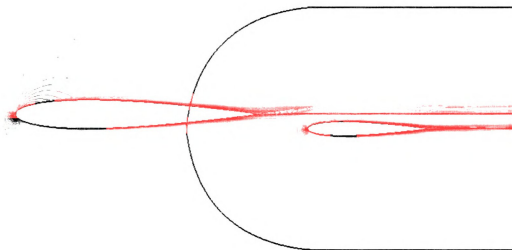


Figure 46 Mach contours around two-element airfoil computed by OVERFLOW with the conservative Chimera

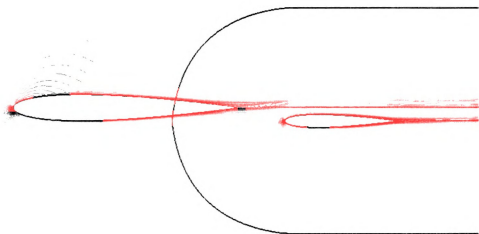


Figure 47 Mach contours around two-element airfoil computed by OVERFLOW with the original Chimera

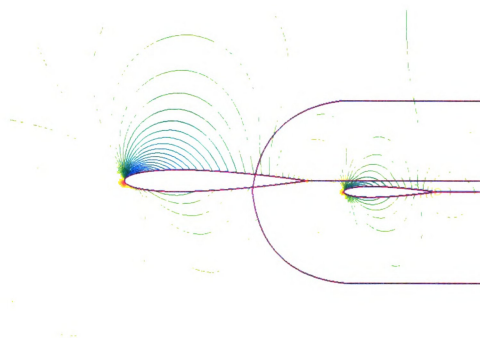


Figure 48 Pressure contours around two-element airfoil computed by OVERFLOW with the conservative Chimera

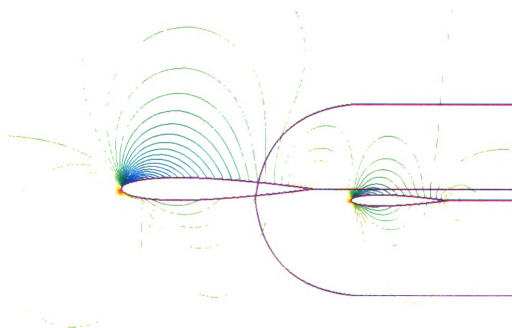


Figure 49 Pressure contours around two-element airfoil computed by OVERFLOW with the original Chimera

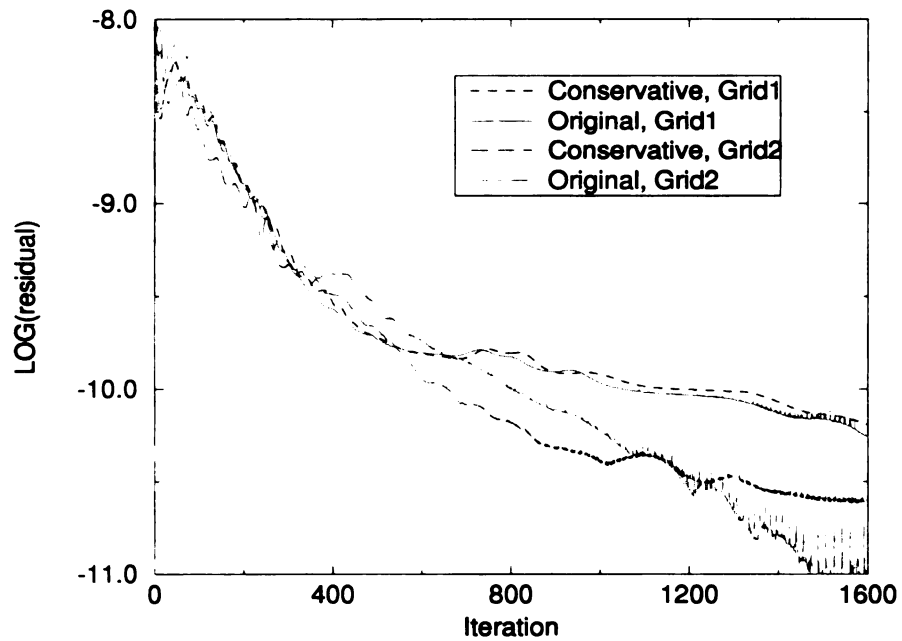


Figure 50 Convergence histories for OVERFLOW with conservative Chimera and original Chimera in the fine grids

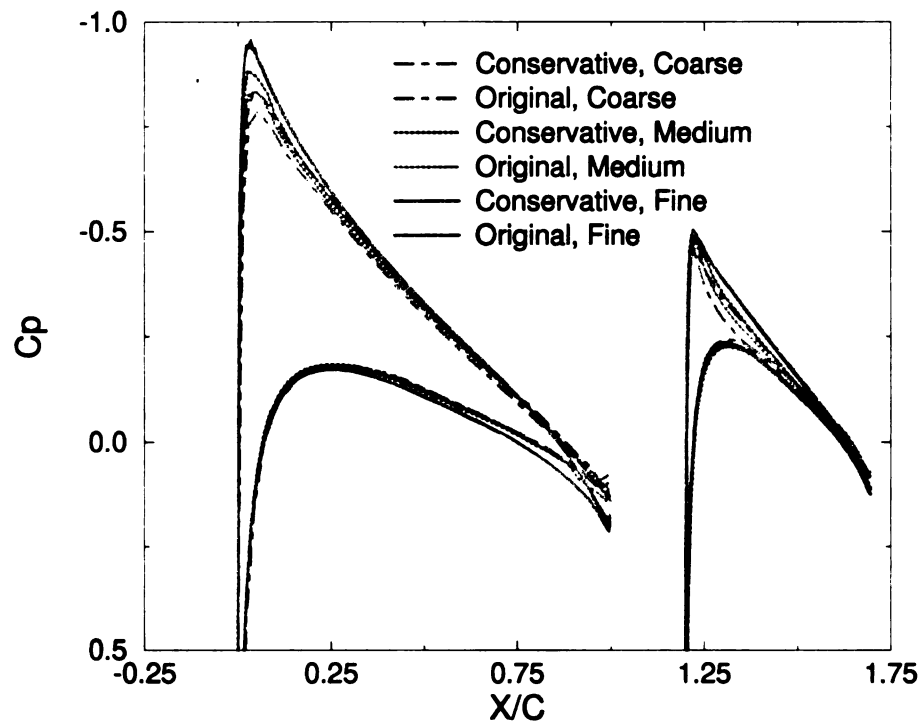


Figure 51 Pressure distributions along the airfoil computed by OVERFLOW with the original and the conservative Chimera in different levels of grids

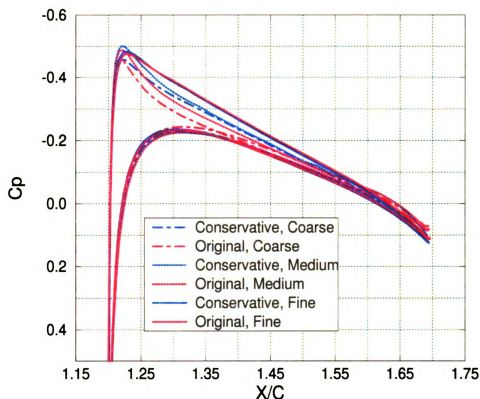


Figure 52 Pressure distributions along the rear airfoil computed by OVERFLOW with the original and the conservative Chimera in different levels of grids

7.4 Turbulent Flow over a Three-Element Airfoil

The case of flow over three-element airfoil has been under extensive studied both numerically (Soetrismo *et al.*, 1994) and experimentally (Valarezo *et al.*, 1991). Three spanwise planes for the original Chimera and four spanwise planes for the enhanced finite difference grids for the conservative Chimera need to be supplied to OVERFLOW. Four different grids, namely coarse grid, medium grid, fine grid and the finest grid, were used for the study of the flow over the three-element airfoil with OVERFLOW. The outer boundary of the main element grid is about ten chord length away from the airfoil. Figure

53 shows part of the medium grid around the airfoil and the patch interfaces and holes generated in the ZIG. Note that the interface between the main element grid and the front element grid backs off to avoid the solid wall of the main element. The finest grids for the main, front and rear elements have dimensions 475 by 160, 481 by 77 and 457 by 79 respectively, which are about twice as fine in each grid direction as those shown in Figure 53. The fine grids are of dimension 360 by 65, 269 by 57 and 297 by 49 for the three elements respectively. Flow conditions were set as the following: free stream Mach number $M_{\infty} = 0.2$, free stream angle of attack $\alpha = 8.2^{\circ}$ and Reynolds number based on free stream velocity and main airfoil chord length $Re = 0.9 \times 10^7$. The Baldwin-Lomax turbulence model is used in the same way as in the two-element airfoil case. The run is stopped after the pressure coefficients around airfoil do not change for 500 time steps.

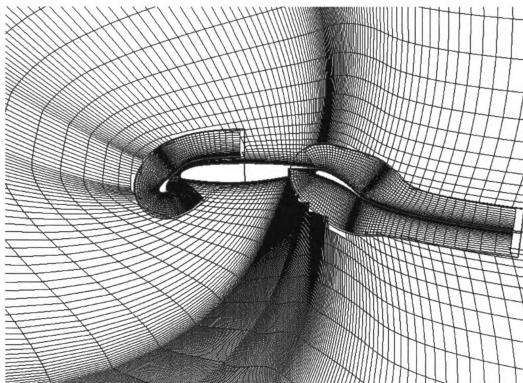


Figure 53 Medium grids and patch interfaces for the thee-element airfoil

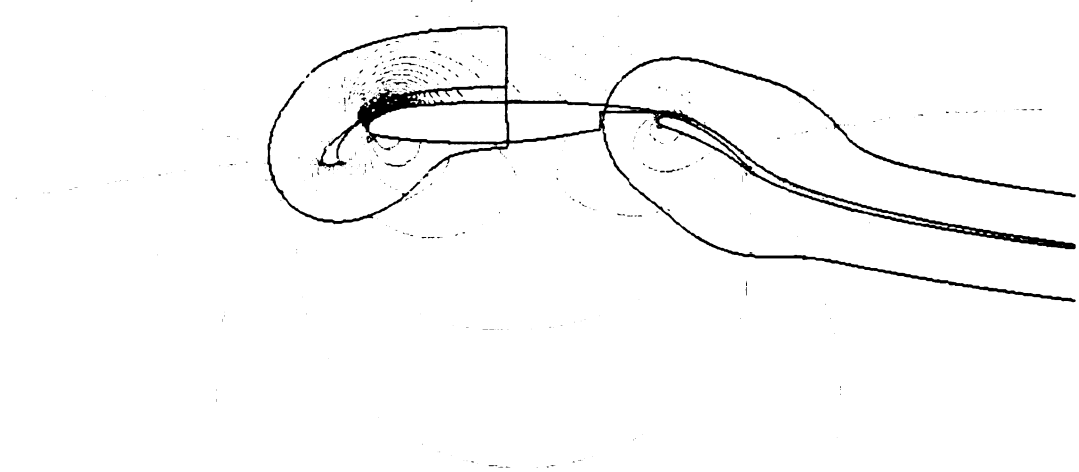


Figure 54 Pressure contours around the three-element airfoil computed using OVERFLOW with the conservative Chimera on the finest grid

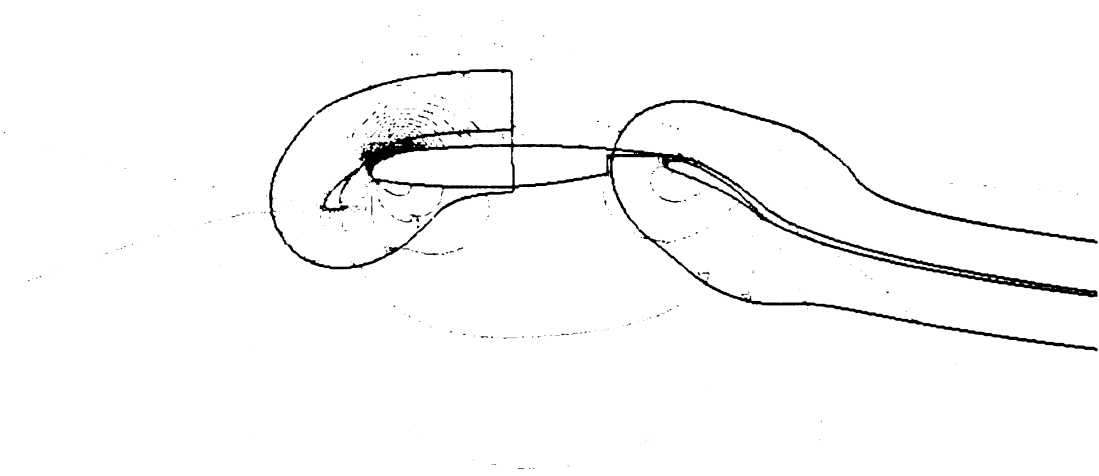


Figure 55 Pressure contours around the three-element airfoil computed using OVERFLOW with the original Chimera on the finest grid

Figure 54 and Figure 55 show the pressure contours around the airfoil simulated with OVERFLOW on the finest grid. It is observed that the contour patterns shown in Figure 54 and Figure 55 obtained with different methods are similar. Figure 56 and Figure 57 show the distribution of the pressure coefficients along the airfoil surface computed with the different grids by different methods compared to experimental data. It is shown that the results are significantly improved when the grid resolution increases from the coarse grid to the medium grid. The results for the finest grid and the fine grid are, however, almost same. This shows that the finest grid is fine enough for this demonstration case, at least for the methods and turbulent model used in this case. The comparison of the pressure distributions along the airfoil surfaces computed with the conservative and the original Chimera is displayed in Figure 58. Note that the peak values in the pressure profiles computed with the original Chimera are better than those with the conservative Chimera. On the other hand the conservative Chimera yields better predictions near the stagnation points, especially for the front element. In general, the Conservative Chimera gave similar solutions as the Original Chimera. OVERFLOW with the conservative Chimera and the original Chimera is also run for the inviscid flow over this three-element airfoil with same free Mach number on the fine grid. Figure 59 shows the comparison of pressure coefficients along the airfoils for the inviscid flow with the experimental data. It is shown that the pressure profiles obtained with both Chimera treatments are almost same. Comparing Figure 59 with Figure 56 and Figure 57, it is obvious that the results of the inviscid flow agree better with experimental data. The discrepancy between the experimental data and the numerical solutions on the finest grid may imply that the Baldwin-Lomax turbulent model is not good enough for turbulent flows over the three-element airfoil.

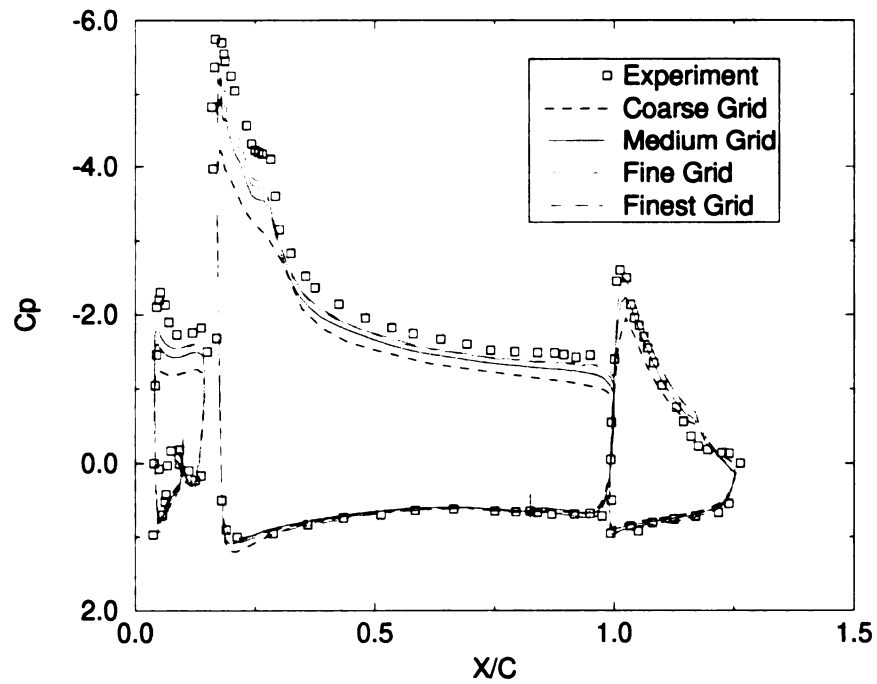


Figure 56 Pressure distributions along airfoil surfaces computed using OVERFLOW with the original Chimera

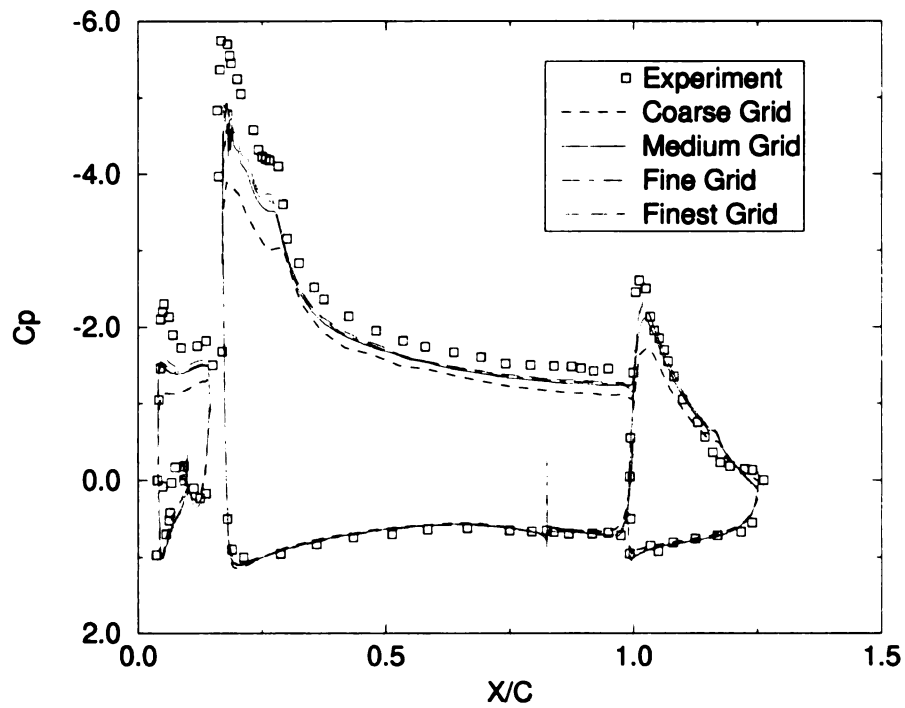


Figure 57 Pressure distributions along airfoil surfaces computed using OVERFLOW with the conservative Chimera

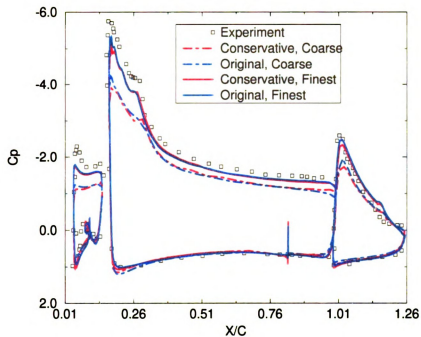


Figure 58 Comparison of pressure distributions along the airfoil surfaces computed using OVERFLOW with the conservative and the original Chimera

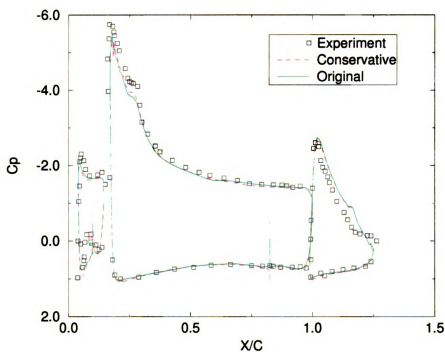


Figure 59 Comparison of pressure distributions for the inviscid flow along the airfoil surfaces computed with OVERFLOW.

7.5 Summary

Tests with inviscid, laminar and turbulent flows with different geometries have validated the implementation of the fully conservative Chimera in OVERFLOW. The results obtained with the conservative Chimera and the original Chimera approaches for most cases are similar. For the turbulent flow over the two-element airfoil the pressure distributions along the rear element obtained with the two Chimera approaches in the fine grid are almost identical. If the results in the fine grid is assumed to be close enough to the actual solution, the pressure distributions along the rear element obtained with the conservative Chimera approach in the coarser grids (coarse and medium grids) are much closer to the actual solution than those with the original Chimera approach. But for the turbulent flow over then three-element airfoil the peak values in the pressure profiles computed with the original Chimera are better than those with the conservative Chimera. Therefore for the smooth flow we may conclude the following: In general the conservative Chimera and the original Chimera yield similar results. The conservative Chimera may make a difference as compared to the original Chimera for some cases in relatively coarse grids.

In the testing of the conservative Chimera with the turbulent flow over the three-element airfoil we found that the computation can not process without the special treatment in evaluating velocity gradients at the patch interfaces. The implicit treatment of the patch interface are found to be necessary to boost the stability and accelerate the convergence rates for all the validation cases. Due to the appearance of the irregular cut cells near the patch boundaries, without the implicit treatment of the patch interface the convergence rate with the conservative Chimera approach is slow and not competitive to that with the original Chimera approach.

8 DEMONSTRATION OF THE FULLY CONSERVATIVE CHIMERA IN OVERFLOW

The purpose of the demonstration cases is to show the capability of the conservative Chimera in tackling more complicate flow problems. Since there are not experimental data available for the demonstration cases, the results obtained with the conservative Chimera can only be qualitatively evaluated based on the visual images of surface and contour plots.

8.1 Hypersonic Flow Around a Launch Rocket

This case contains seven grid components: one main rocket and six smaller boosters. Only half of the flow field was calculated because of symmetry. The four zone mesh in the half field is shown in Figure 60. For the main rocket 81 grids is distributed in the stream wise direction, 39 grids in the direction normal to the body surface and 61 in the circumferential direction. Each booster's grid is of dimension $31 \times 9 \times 21$. The outer boundaries of the boosters' grids are used as the patch interfaces. The free stream Mach number is 6 and the angle of attack is set to 2.5° . Figure 61 shows the Mach contours on the surfaces of the main rocket and the boosters as well as the Mach contours on the last across stream-wise plane in the main grid domains. Figure 62 displays a close-up view of Figure 61 on the region around the boosters. The effects of the presence of the boosters can be clearly seen on the surface of the rocket. These figures also show the intricate shock wave patterns resulted as the flow moves over the configuration. In particular the shock patterns from the smaller boosters, and their reflection off the surface of the main booster are well captured.

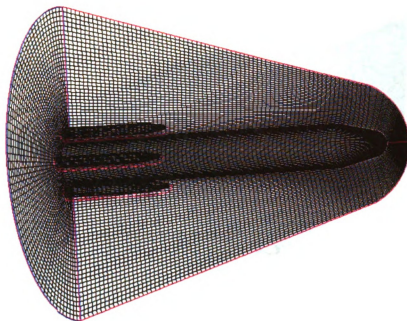


Figure 60 Four zone Chimera grid for hypersonic flow around a launch rocket

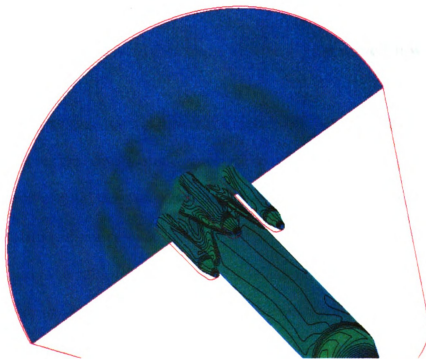


Figure 61 Mach distributions on the surfaces of the rocket and the boosters and on the last cross-streamwise plane computed using OVERFLOW with the conservative Chimera

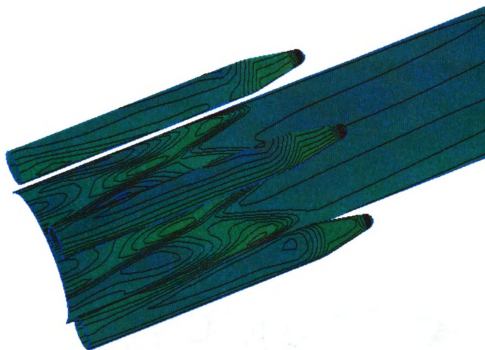


Figure 62 Mach contours on the surfaces of the rocket and the boosters

8.2 Demonstration of Local Refinement with Hypersonic Flow Around a Launch Rocket

The case of hypersonic inviscid flow over a rocket with six boosters has been shown in the last subsection. This case is used again to demonstrate the capability of local refinement implemented in the ZIG. The grids without local refinement is shown in Figure 60. A region in the main grid, which encloses the grid of the middle booster as shown in the Figure 63, is chosen to be refined. The factors of the refinement in all three grid directions are set to 2. Then the grid in this region is automatically generated in the ZIG by locally refining the main rocket grid by the given factor in each direction. Let the grid of the rocket and grids of three boosters be zone 1, 2, 3 and 4 respectively, and the grid in the refined region be zone 5. Then there are patch interfaces between zone 1 and zone 5, interfaces between

zone 1 and zone 2, interfaces between zone 1 and zone 4, and interfaces between zone 5 and zone 3. The grids of zone 2 and zone 4 share the major grid of zone 1. The grid in zone 5 is the minor grid for the interfaces between zone 1 and zone 5, as well as the major grid for the interfaces between zone 3 and zone 5.

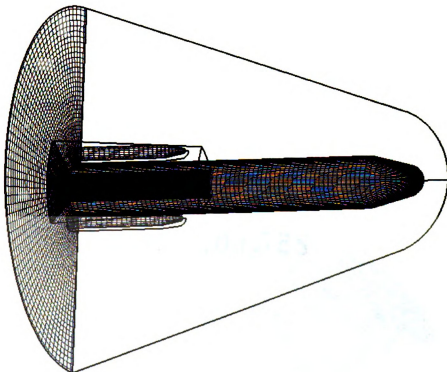


Figure 63 Grids around the rocket and the boosters with local refinement

The flow conditions are set to the same as those in the case without local refinement. Both OVERFLOW and CFD-FASTRAN from CFDRC with conservative Chimera are run for this case. Figure 64 shows the Mach contours on the surfaces of the main rocket and the boosters, as well as the Mach contours on the last cross-streamwise plane of the main grid. Figure 65 shows the density distributions on the surfaces in the region around the boosters. These results are simulated by OVERFLOW with the conservative Chimera. It

can be seen that the shock waves inside the local refinement zone are significantly sharper than those outside. The reflection of the shock waves of boosters off the surface of the main rocket are well captured. The figures also show that flow variables are smooth across the patch interfaces and intricate shock wave patterns that result as the flow moves over the boosters are resolved well. Comparison of the results with local refinement shown in Figure 64 and Figure 65 and the results without local refinement shown in the Figure 61 and Figure 62 confirms the improvement with local refinement. The Mach contours on the surfaces of the rocket and a cross-section plane simulated with CFD-FASTRAN are shown in the Figure 66 and Figure 67. The improvements of the contour resolutions by the local refinement are also clearly seen in these figures.

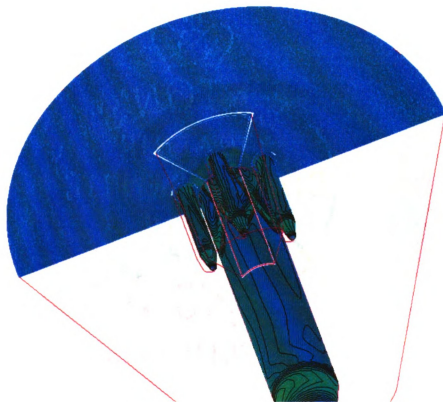


Figure 64 Mach contours on the body surfaces and on the last cross stream plane simulated with OVERFLOW with the conservative Chimera

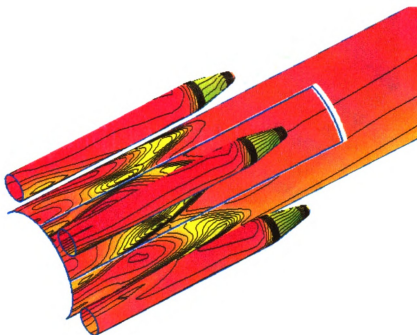


Figure 65 Density contours on the body surfaces computed with OVERFLOW with the conservative Chimera

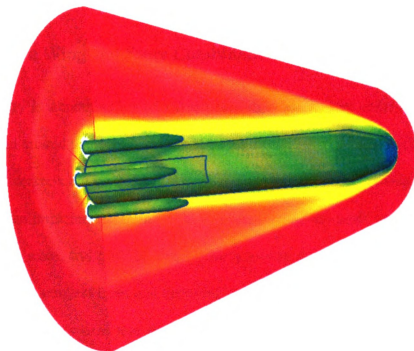


Figure 66 Mach distributions on the body surfaces and some sections simulated with CFD-FASTRAN with local grid refinement

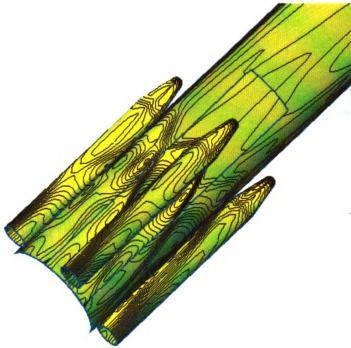


Figure 67 Mach contours on the body surfaces simulated with CFD-FASTRAN with local grid refinement

8.3 Flow over a Wing and Store Combination

The geometry is a combination of a symmetric wing and a store under the wing. The physical domain around the store is chosen to be big enough so that the outer boundary of the store grid intersects the wing. This is done on purpose to test the automatic interface backoff algorithm implemented in the ZIG. Figure 68 shows the grids on the surfaces of the wing and the store, and grids on two across spanwise sections. Figure 69 shows the patch interface, the smallest faces and the holes cut automatically by the ZIG with different viewing angles. It is seen that the smallest faces have arbitrary shapes, which are shown in the different colors in Figure 69. The patch interfaces consist of all the smallest faces, which are pushed back from the wing to avoid the wing as shown in the figure.

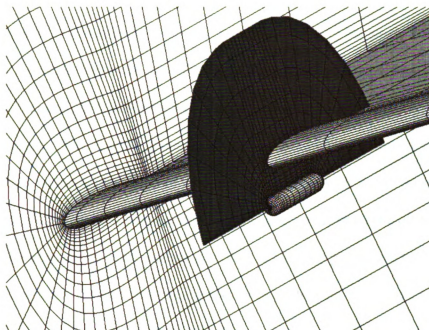


Figure 68 Grids and the configuration of the wing-store combination

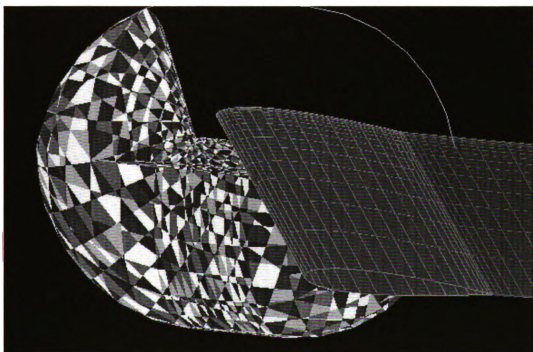


Figure 69 Patch interfaces, smallest faces and holes cut by the ZIG

The free stream Mach number is 0.5 and the angle of attack is set to zero. A symmetric Boundary condition was applied to the end of the wing close to the store. The other end of the wing is extended far away from the store, simple extrapolation was applied to the boundary at that end. OVERFLOW with the conservative Chimera was used to simulate the inviscid steady flow over the geometry. Figure 70 and Figure 71 show the pressure and Mach contours on the surfaces of the wing and the store as well as the pressure contours on one across spanwise section respectively. The effects of the presence of the store can be seen from the contours on that section. Contours across the patch interfaces are smooth. Figure 72 shows the convergence histories for both grids. This case once again validates the inviscid implementation of conservative Chimera in the OVERFLOW and demonstration the ability of the Chimera handling complex geometries.

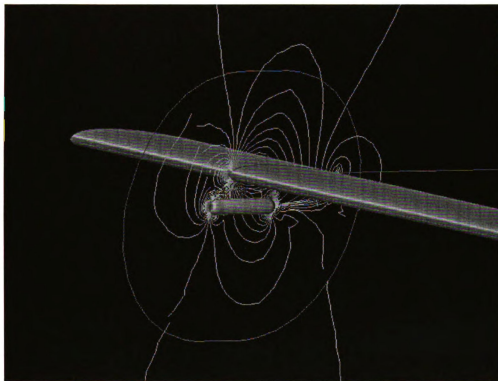


Figure 70 Pressure contours on the surfaces of the wing and the store and on one spanwise section computed using OVERFLOW with the conservative Chimera

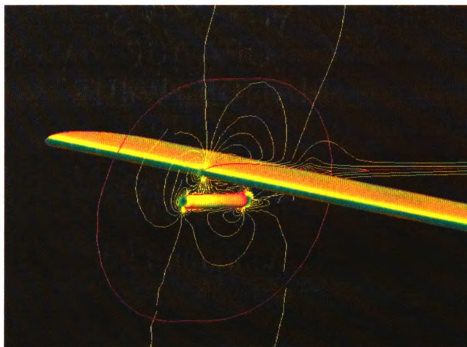


Figure 71 Mach contours on the surfaces of the wing and the store and on a spanwise section computed using OVERFLOW with the conservative Chimera

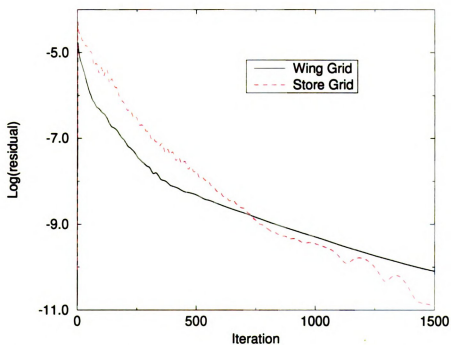


Figure 72 Residual history for the simulation of flow over wing and store combination by OVERFLOW with conservative chimera

8.4 Transonic Flow Around a Combination of Wing and Missiles

The geometry in this demonstration case is a combination of an extended delta wing and two missiles under the wing. There are four fins on the surface of each missile. Figure 73 shows the geometry including the shadows of the fins. Figure 74 shows surface grids, one section of grids around the wing and the outer boundaries of the two missile grids. Note that the physical domains around the missiles are set to be big enough to intersect the wing. The grid around the wing has 137 points in the streamwise direction, 39 points in the spanwise direction and 31 points in the cross streamwise direction. The grid of each missile is of the dimension $50 \times 19 \times 69$, with 50 points in the streamwise direction, 19 points in the direction normal to the body surface and 69 points in the circumferential direction. Figure 75 shows the outer boundaries of the missiles after the cutting in the ZIG, which are parts of the patch interfaces between the missile grids and the grid around the wing. It is seen the patch interfaces are backed off from the surface of the wing to avoid the wing.

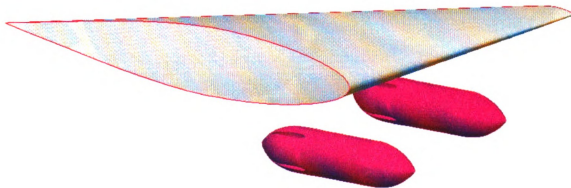


Figure 73 Configuration of the combination of wing and two missiles

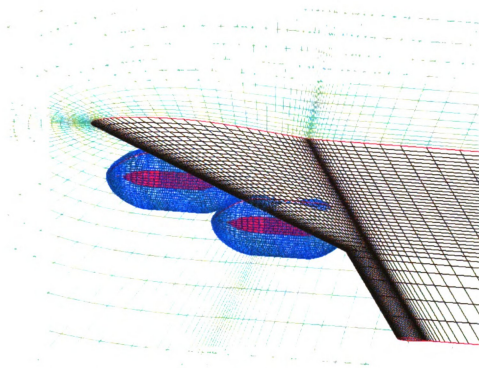


Figure 74 Grids for the combination of wing and two missiles

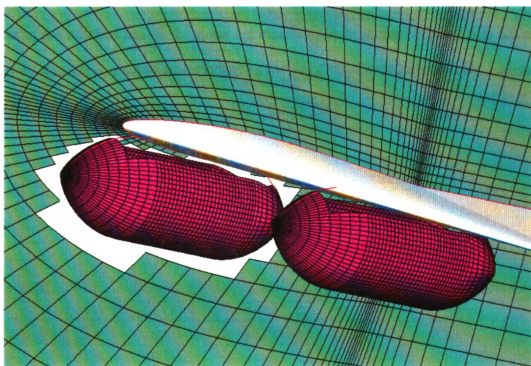


Figure 75 Holes automatically cut in the ZIG

The free stream Mach number is 0.8 and the angle of attack is set to zero. Both CFD-FASTRAN and OVERFLOW with conservative Chimera are run to simulate the flow over the combination of the delta wing and two missiles. The boundary condition at both ends of the delta wing set to be symmetric. The fins on each missile are set to be blockages for CFD-FASTRAN, and CFD-FASTRAN can automatically treat the boundaries of the fins as walls. In OVERFLOW, however, solid wall boundary conditions must be specified in the input file for the five surfaces of each fin on the missiles. For each missile, twenty boundary conditions for four fins, and five more boundary conditions for the missile grid are needed to set up the problem. Figure 76 and Figure 77 show pressure contours on two cross sections and the pressure distributions on the surfaces simulated by OVERFLOW and CFD-FASTRAN with the conservative Chimera respectively. Figure 78 and Figure 79 display the pressure distributions on the surfaces and two cutting planes simulated by OVERFLOW and CFD-FASTRAN with the conservative Chimera respectively. The effects of the missiles fins on the flows are clearly seen from these figures. It is observed that the solutions computed with OVERFLOW and CFD-FASTRAN are quite similar to each other as they are expected.

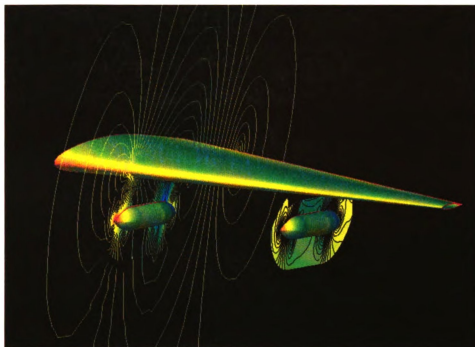


Figure 76 Pressure contours on the surfaces and two streamwise sections simulated using OVEFLOW with the conservative Chimera

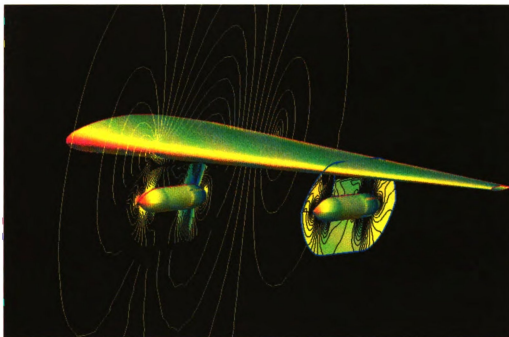


Figure 77 Pressure contours on the surfaces and two streamwise sections simulated using CFD-FASTRAN with the conservative Chimera

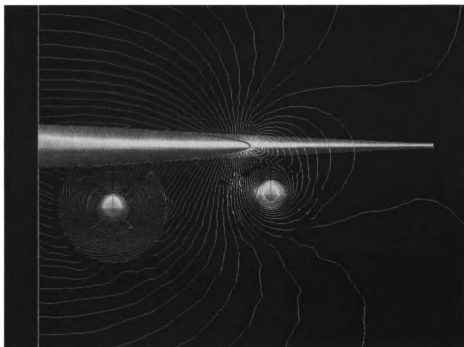


Figure 78 Pressure contours on the surfaces and two spanwise sections simulated using OVEFLOW with the conservative Chimera

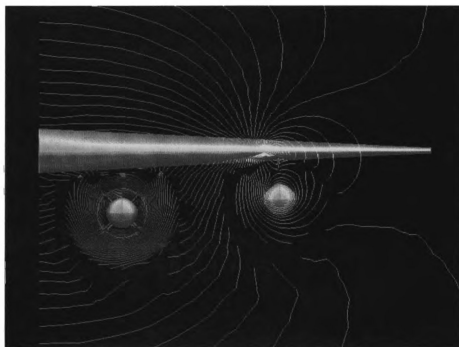


Figure 79 Pressure contours on the surfaces and two spanwise sections simulated using CFD-FASTRAN with the conservative Chimera

9 CONCLUSIONS

9.1 Summary

A computational methodology has been developed in the first part of the thesis for the simulations of acoustic radiation, propagation and reflection. The developed methodology has high order of accuracy, uses less grid points per wave length comparing to standard high order numerical methods, and automatically damps out spurious short waves. Furthermore, the methodology can be applied to acoustic problems in the presence of objects with curved geometries. To achieve these results, high order accurate optimized upwind schemes, which are applied to discretize spatial derivatives on interior grid points, have been developed. High order accurate optimized one-side biased schemes, which are only applied to discretize the spatial derivatives on grid points near computational boundaries, have also been constructed. The developed schemes are combined with a time difference scheme to fully discretize acoustic field equations in multi-dimension in arbitrary curvilinear coordinates. Numerical boundary conditions were investigated and intuitively illustrated. Applications of the developed methodology to a sequence of one-dimensional and multi-dimensional acoustic problems are performed. The numerical results have validated the developed methodology, demonstrated advantages of the methodology, and showed that the objectives of the methodology has been achieved. More specifically, the conclusions and work done in the first part of the thesis are summarized as the following:

A method of constructing a class of high order, optimized, upwind, finite difference schemes for discretizing spatial derivatives based on the analysis on the model wave equa-

tion has been developed. An fourth order accurate, 7-stencil, optimized, upwind scheme has been actually constructed based on the developed method. The comparison of the effective numerical wavenumbers of different schemes shows that the 7-stencil optimized upwind scheme has built in dissipation so that it can automatically damps out spurious short wave. It has much less dissipation error than those of the standard six-order accurate upwind scheme and backward spatial schemes developed in Tam & Webb's DRP method. It is able to resolve the waves with as high wavenumbers as those resolved by Tam & Webb's central DRP. The tests of a initial Gaussian pulse and a initial step wave on the model wave equation have validated the advantages of the optimized upwind scheme.

Acoustic field equations in different forms and in generalized curvilinear coordinate systems are derived for integrity. The Jacobian matrices and their corresponding eigenvalues and eigenvectors associated to the field equations are also derived. It is illustrated that disturbance waves can be decomposed as entropy waves, vorticity waves and acoustic waves. Acoustic waves are treated differently in the matrix splitting techniques according to their propagating directions. Matrices similar to arbitrary diagonal matrices through similarity transformations of eigenvectors matrices are derived. The correct forms of these matrices are important in the matrix splitting techniques and convenient for the future applications. The numerical tests of the multi-dimensional problems have validated the correct derivations of the matrices.

The optimized upwind schemes have been extended to acoustic field equations in multi-dimension in generalized curvilinear coordinates with the matrix splitting techniques. High order one-side biased optimized schemes used for grid points near the computational boundaries have also been developed. The boundary conditions for curved wall

are developed. Radiation and outflow boundary conditions in the far field are intuitively illustrated. The boundary conditions are implemented with one-side biased optimized schemes. The optimized upwind scheme together with the one-side biased optimized schemes and the DRP temporal difference scheme gives an numerical methodology for the computational aeroacoustics. With the extension of the optimized upwind schemes to multi-dimension and the derived boundary conditions, the methodology can then be applied to accurately solve the acoustic problems in the presence of objects with curved geometries.

A sequence of direct numerical simulations on one-dimensional and multi-dimensional acoustic problems have been carried out to test the effectiveness of the developed methodology for CAA. Differences between numerical results obtained with the optimized upwind scheme, central DRP methods, standard six-order accurate upwind schemes, and analytical results are compared for many cases. In comparisons, the best effort was made to ensure that all other factors remains the same. These factors include the computational grid, the time step, etc. The tests show that the developed optimized upwind scheme automatically damps out the spurious short waves, without the need of filters or explicit dissipation terms. The tests show the optimized upwind scheme provides more accurate solutions than the central DRP methods for all the simulations with the exact solutions available. Central DRP methods without adding damping term cause spurious oscillations in some cases. Adding dissipation can eliminate the seriously spurious oscillations of numerical results. The test of the acoustic radiation from a oscillating piston clearly demonstrates that computational error associated with the optimized upwind scheme is significantly less than that associated with the central DRP with finely tuned

damping term. The optimized upwind scheme minimizes not only the dissipation errors but also the dissipation errors, while retaining the numerical stability. The developed methodology have been applied to the scatterings of acoustic pulses off a cylinder and a sphere. The curvilinear transforms are employed to test the extension and implementation of the methodology for acoustic field equations in multi-dimension in generalized curvilinear coordinates. Although there are no direct comparisons available for these simulations, the obtained wave patterns have validated the extension and implementation of the methodology. The numerical results demonstrated that the developed methodology has the ability to handle the curved walls and can be applied to acoustic problems when more complex geometries involved. This will be discussed more in detail in the suggestions for future work. The objective of investigating, developing and applying optimized upwind schemes for CAA has been achieved in the first part of the thesis.

The second part of the thesis deals with a fully conservative Chimera methodology. The fully conservative Chimera was developed originally based on finite volume approach. A finite difference scheme, however, is shown to be identical to a finite volume scheme with proper definition of control volumes and matrices. The fully conservative Chimera has been successfully extended to finite difference numerical scheme for viscous flows including turbulent models and successfully implemented into NASA's widely used code OVERFLOW. In the implementation the Roe's numerical fluxes are employed to the inviscid fluxes across the patch interfaces. The thin layer approximation is used in the calculating of viscous fluxes in the patch interfaces. The implementation also includes implicit treatment of the patch interfaces.

Tests on several inviscid, viscous laminar and turbulent, exterior flows over objects

with complex geometries were performed to validate the implementations and demonstrate the conservative Chimera methodology. Numerical tests indicate that implicit treatment of the patch interface is extremely important to the stability of the overall time-marching procedure. Due to the appearance of very irregular cut cells with potentially diminishing volumes and time steps, the time-marching procedure is found to be quite unstable without the implicit treatment. With the implicit treatment the stability of the numerical scheme with the conservative Chimera is competitive to that of the original Chimera.

The implementation of the fully conservative Chimera into the OVERFLOW allows the errors in the traditional Chimera approach due to non-conservative data interpolations to be evaluated through direct comparisons. A grid refinement study with a subsonic two-element airfoil flow case shows that the conservative Chimera makes a difference as compared to the original Chimera even for flows without discontinuities. The difference, however, diminishes with global grid refinement for smooth flows.

9.2 Suggestions to Future Work

For the numerical consideration, the time marching scheme which may be more suitable than the DRP time difference scheme for the developed optimized upwind scheme should be investigated and developed. The effective numerical wavenumber or frequency of full numerical discretizations by both the spatial and temporal schemes should be considered together, because the numerical errors attributes to both schemes. Treating the spatial and temporal schemes separately can not accurately reflect global effects of the numerical errors caused by the approximations of the effective numerical wavenumber or

frequency to the actual wavenumber or frequency. The errors of numerical schemes on the acoustic field equations in multi-dimension should be analyzed to better understand the effects of the matrix splitting techniques on numerical accuracy and stability. Furthermore the numerical errors caused by the boundary conditions are still not clear and need to be analyzed. The test case on the reflection of an acoustic pulse off a straight wall in a two-dimensional uniform flow clearly show the errors caused by the boundary conditions.

For the application consideration, grid generation for complicate geometries requires the most of man power. Furthermore there is not easy way to accurate evaluated the matrices of a given grid. Body-fitted grid systems near arbitrary objects and uniform Cartesian grid system in the farfield with Chimera grid technology can be an effective way to handle the complex geometries. The optimized upwind scheme combined with a finite volume discretization approach should be investigated and developed. The optimized upwind scheme with the finite volume discretization approach combining with the chimera technology will provide an effective way for simulating acoustic problems when the objects with very complicate geometries are involved. The mean flows can be obtained by recent commercial CFD software. The proposed methodology can then be used to solve the acoustic field equations with the given mean flows. For example, we may use CFDRC's geometrical modeling/grid generation package, CFD-GEOM for grid generation, CFDRC's flow solver, CFD-FASTRAN for the simulation of mean flows, a CAA module with proposed methodology to predict aeroacoustic waves, and CFDRC's post-processing package CFD-VIEW for field visualization. This will result in a computational environment which would present the opportunities to investigate sound generating mechanisms, directivity, spectral features and the propagation of the sound to the far field.

REFERENCE

REFERENCE

- [1]. Ahmad, J., and Duque, E.P.N., "Helicopter Rotor Blade Computation in Unsteady Flows Using Moving Embedded Grids," AIAA 94-1922, 1994.
- [2]. Anderson, D. A., Tannehill J. C. and Pletcher, R. H., "Computational Fluid Mechanics and Heat Transfer," Taylor & Francis, 1984.
- [3]. Barth, T.J., "Higher Order Solution of the Euler Equations on Unstructured Grids Using Quadratic Reconstruction," AIAA Paper 90-0013, 1990.
- [4]. Benek, J.A., Buning, P.G. and Steger, J.L. "A 3D Chimera Grid Embedding Technique," AIAA Paper 85-1523, 1995.
- [5]. Benek, J.A., Steger, J.L. and Dougherty, F.C., "A Flexible Grid Embedding Technique with application to the Euler Equations," AIAA Paper 83-1944, 1983.
- [6]. Berger, M.J., "On Conservation at Grid Interfaces," SIAM Journal of Numerical Analysis, vol. 24, 1987.
- [7]. Blanco, M. and Zingg D.W., "Fast Newton-Krylov Method for Unstructured Grids," AIAA Journal, vol. 36, No.4, 1998.
- [8]. Buning, P.G and Chan, W.M., "OVERFLOW/F3D User's Manual," NASA Ames Research Center, Moffett Field, California, February, 1991.
- [9]. CFD Research Corporation, "CFD-FASTRAN User's manual," CFDRC Report GR-93-2, 1993.
- [10]. CFD Research Corporation, "CFD-GEOM User's manual, Interactive Geometric Modeling and Grid Generation Software," Feb., 1998.
- [11]. CFD Research Corporation, "CFD-VIEW User's manual, 3-D Computer Graphics and Animation Software," Feb., 1998.
- [12]. Chakravarthy, S.R. and Osher, S., "A New Class of High accuracy TVD Schemes and Their Applications," Journal of Computational Physics, vol. 68, pp. 151-179, 1987.
- [13]. Chen, R.F., and Zhuang, M., "Application of Dispersion-Relation-Preserving Scheme to the Computation of Acoustic Scattering in Benchmark Problems." in ICASE/LaRC 2nd workshop on benchmark problems in Computational Aeroacoustics, Tallahassee, FL., Nov., 1996,

- [14]. Davis, D.L. and Thompson, H.D.L., "The Impact of Computational Zonal Interfacing on Calculated Scramjet Performance," AIAA Paper 92-0390, 1992.
- [15]. Duque, E.P.N., Biswas, R., and Strawn, R.C., "A Solution Adaptive Structured/Unstructured Overset Grid Flow Solver with application to Helicopter Rotor Flows," AIAA Paper 95-1766, 1995.
- [16]. Duque, E.P.N., and Strawn, R.C., "An Overset Grid Navier-Stokes Kirchhoff-Surface Method for Rotorcraft aeroacoustic Predictions," AIAA 96-0152, Jan. 1996.
- [17]. Eberhardt, S. and Baganoff, D., "Overset Grids in Compressible Flow," AIAA Paper 85-1542, 1985.
- [18]. Eversman, W., "Theoretical Models for Duct Acoustic Propagation and Radiation," in *Aeroacoustics of Flight Vehicles: Theory and Practice*, ed. H.H. Hubbard, NASA RP-1258, Chapter 13, 1991.
- [19]. Farassat, F., "The Kirchhoff Formulas for Moving Surfaces in Aeroacoustics-The subsonic and Supersonic Cases," NASA Technical Memorandum 110285, 1996.
- [20]. Hardin, J.C., Ristorcelli, J.R., and Tam, C.K.W., ICASE/LaRC workshop on Benchmark Problems in Computational Aeroacoustics. NASA CP 3300, May 1995.
- [21]. Harten, A., Engquist, A., Osher, S. and Chakravarthy, S., "Uniformly High-Order Accuracy Essentially Non-Oscillatory Schemes III," *Journal Computational Physics*, vol. 71, pp. 231-323, 1987.
- [22]. Hixon, R., "Evaluation of a High-Accuracy MacCormack-Type Scheme Using Benchmark Problems," NASA Contractor Report 202324, ICOMP-97-03, 1997.
- [23]. Hixon, D.R., Shih, S., and Mankbadi, R.R., "Evaluation of Boundary Conditions for Computational Aeroacoustics," *AIAA Journal*, vol. 33, pp. 2006-2012, 1995.
- [24]. Kim, C., Roe, P.L. and Thomas, J.P., "Accurate Schemes for Advection and Aeroacoustics," AIAA Paper 97-2091, 1997.
- [25]. Launder, B.E. and Spalding, D.B., "The Numerical Computation of Turbulent Flows," *Computer Methods in Applied Mechanics and Engineering*, vol.3, pp. 269-289, 1974.
- [26]. Lax, P.L., "Hyperbolic Systems of Conservation Laws and the Mathematical Theory of Shock Waves," SIAM, Philadelphia, 1972.
- [27]. Lele, S.K., "Compact Finite Difference Schemes with Spectral-Like Resolution," *Journal Computational Physics*, vol. 103, pp. 16-42, 1992.

- [28]. Li, Y., "Wavenumber-Extended High-Order Upwind-Biased Finite Difference Schemes for Convective Scalar Transport," *Journal of Computational Physics*, vol. 13, pp. 235-255, 1997.
- [29]. Lighthill, M.J., "On Sound Generated Aerodynamically I. General Theory," *Proc. Roy. Soc. A*, vol. 211, pp. 564, 1952.
- [30]. Lim, T.B., Sankar, L.N., and Hariharan, N., "A Technique for the Prediction of propeller Induced Acoustic Loads on Aircraft Structures," *AIAA Paper 93-4340*, 1993.
- [31]. Lin, S.Y., and Chin, Y. S., "Comparison of Higher Resolution Euler Schemes for Aeroacoustics Computations," *AIAA Journal*, vol. 33, No. 2, pp 237-245, 1995.
- [32]. Lin, S.Y., and Chen, Y.F., "Numerical Study of MUSCL Schemes for Computational Aeroacoustics," *AIAA Paper 97-0023*, 1997.
- [33]. Liu, Y, "Fourier Analysis of Numerical Algorithms for the Maxwell Equations," *Journal of Computational Physics*, vol. 124, pp.396-416, 1996.
- [34]. Lockard, D.P., Brentner, K.S., and Atkins, H.L., "High-Accuracy Algorithms for Computational Aeroacoustics," *AIAA Journal*, vol. 33, No. 2, pp. 246-251, 1995.
- [35]. Mavriplis, D.J., "Unstructured Mesh generation and adaptivity," *ICASE Report NO. 95-26*, 1995.
- [36]. Meakin, R.L., "A New Method for Establishing Intergrid Communication Among Systems of Overset Grids," *AIAA paper 91-1586-CP*, 1991.
- [37]. Mecham, M. and Mckenna, J.T., "Cost, Not Size, To Drive Success of Super-jumbo," *Aviation Week and Space Technology*, Nov. 21, 1994.
- [38]. Moon, Y.J., and Liou, M.S., "Conservative treatment of Boundary Interfaces for Overlaid Multi-Level Grid Adaptions," *AIAA Paper 89-1980-CP*, 1989.
- [39]. Motsinger, R.E. and Kraft, R.E., "Design and Performance of Duct acoustic Treatment," in *Aeroacoustics of Flight Vehicles: Theory and Practice*, ed. H.H. Hubbard, NASA RP-1258, Chapter 14, Aug. 1991.
- [40]. Parks, S.J., Buning, P.G., Steger, J.L. and Chan, W.M., "Collar Grids for Intersecting geometric Components within the Chimera Overlapped Grid Scheme," *AIAA Paper 91-1587-CP*, 1991.
- [41]. Pulliam, T.H. and Steger, J.L., "Implicit Finite-Difference Simulations of Three-Dimensional Compressible Flow," *AIAA Journal*, vol. 18, No. 2, pp159, 1980.
- [42]. Roe, P.L., "Approximate Riemann Solver, Parameter Vectors and Difference

- Schemes,” *Journal of Computational Physics*, vol. 43, pp. 357, 1983.
- [43]. Rogers, S.E. and Pulliam, T.H., “Accuracy Enhancements for Overset Grids Using a Defect Correction approach,” *AIAA Paper 94-0523*, 1994.
 - [44]. Rogers, S.E., Wiltberger, N.L., and Kwak, D., “Efficient Simulation of Incompressible Viscous Flow over Single and Multi-Element Airfoils,” *AIAA Paper 92-0405*, 1992.
 - [45]. Sankar, L.N., Reddy, N.N., and Hariharan, N., “A Third Order Upwind Scheme for Aeroacoustic Applications,” *AIAA Paper 93-0149*, 1993.
 - [46]. Soetrismo, M., Imlay, S.T. and Roberts, D.W., “A Zonal Implicit Procedure for Hybrid Structured-Unstructured Grids,” *AIAA Paper 94-0645*, 1994.
 - [47]. Steger, J.L., Dougherty, F.C. and Benek, J.A., “A Chimera Grid Scheme,” *ASME Mini-Symposium on Advances in Grid Generation*, Houston, Texas, June, 1983.
 - [48]. Steger, J.L., Dougherty, F.C. and Benek, J.A., “A Chimera Grid Scheme,” *Advances in Grid Generation*, K.N. Ghia eds., *ASME FED*, vol. 5, 1985.
 - [49]. Strawn, R.C., Oliker, L., and Biswas, R., “New Computational Methods for the Prediction and Analysis of Helicopter Noise,” *AIAA Paper 96-1696*, 1996.
 - [50]. Tam, C.K.W., “Advances in Numerical Boundary Conditions for Computational Aeroacoustics,” *AIAA Paper 97-1774*, 1997.
 - [51]. Tam, C.K.W., “Computational Aeroacoustics: Issues and Methods,” *AIAA Journal*, vol. 33, No. 10, pp. 1788-1796, 1995.
 - [52]. Tam, C.K.W., and Dong, Z., “Wall Boundary Conditions for High-Order Finite-Difference Schemes in Computational Aeroacoustics,” *Theoretical and Computational Fluid Dynamics*, vol. 6, pp. 303-322, 1996.
 - [53]. Tam, C.K.W., Kurbatskii, K.A. and Fang, J., “Numerical Boundary Conditions for Compositional Aeroacoustics Benchmark Problems,” in *Proceedings of the Second Computational Aeroacoustics Workshop on Benchmark Problems*, ed. Tam, C.K.W. and Hardin, J.C., 1997.
 - [54]. Tam, C.K.W., and Webb, J.C., “Dispersion-Relation-Preserving Finite difference Schemes for Computational Acoustics,” *Journal Computational Physics*, vol. 107, No. 2, pp. 262-281, 1993.
 - [55]. Tam, C.K.W., Webb, J.C., and Dong, Z., “A Study of the Short Wave Components in Computational Acoustics,” *Journal Computational Acoustics*, vol. 1, No. 1, pp 1-30, 1993.

- [56]. Tatsumi, S., Martinell, L., and Jameson, A., "Flux-Limited Schemes for the Compressible Navier-Stokes Equations," AIAA Journal, vol. 33, No. 2, 1995.
- [57]. Tidriri, M.D., "Krylov Methods for Compressible Flows," ICASE report No. 95-48, 1995.
- [58]. Venkatakrishnan, V. "Implicit Schemes and Parallel Computing in Unstructured Grid CFD," ICASE report No. 95-28, 1995.
- [59]. Valarezo, W.O., Momonic, C.J. and McGhee, R.J., "Multi-Element Airfoil Optimization for Maximum Lift at Higher Reynolds Number," AIAA Paper 91-3332, 1991.
- [60]. Walters, R.W., Thomas, J.L. and Switzer, G.F., "Aspects and Applications of Patched Grid Calculations," AIAA Paper 86-1063, 1986.
- [61]. Wang, Z.J. "A Fully Conservative Interface Algorithm for Overlapped Grids," Journal of Computational Physics, vol. 122, pp.96-106, 1995.
- [62]. Wang, Z.J., Buning, P.G and Benek, J., "Critical Evaluation of Conservative and Non-Conservative Interface Treatment for Chimera Grids," AIAA Paper 95-0077, 1995.
- [63]. Wang, Z.J., Hariharan, N., and Chen R.F., "A Fully Conservative Chimera Approach for Structure/Unstructured Grids in Computational Fluid Dynamics," SBIR Phase II Final Report for NASA ARC, Contract Number: NAS2-14226, 1997.
- [64]. Wang, Z.J., Hariharan, N., and Chen R.F., "Recent Developments on the Conservation Property of Chimera," AIAA Paper 98-0216, 1998.
- [65]. Wang, Z.J. and Yang, H.Q., "A unified Conservative Zonal Interface Treatment for Arbitrarily Patched and Overlapped Grids," AIAA Paper 94-0320, 1994.
- [66]. Wang, Z.J., Yang, H.Q. and Przekwas, A.J., "Implicit Conservative Interfacing for 3D Overlapped Chimera Grids," AIAA Paper 95-1683-CP, 1995.
- [67]. Warming, R.F. and Beam, R.M. "On the Construction and Application of Implicit Factorized Schemes for Conservation Laws," SIAM-AMS Proceedings, vol. 11, pp.85-129, 1978.
- [68]. Warming, R.F. and Beam, R.M. "Upwind Second-Order Difference Schemes and Applications in Unsteady Aerodynamic Flows," Proc. AIAA 2nd Computational Fluid Dynamics Conference, Hartford, Connecticut, pp.17-28, 1975.
- [69]. Whitham, G. B., "Linear and Nonlinear Waves," Wiley-Interscience, New York,

1974.

- [70]. Yee, H. C., "A Class of High-Resolution Explicit and Implicit Shock-Capturing Methods," NASA TM 101088, 1989.
- [71]. Zhuang, M., and Chen, R.F., "Optimized Upwind Dispersion-Relation-Preserving Finite Difference Schemes for Computational Aeroacoustics." AIAA Journal, Vol. 36, No. 11, 1998.
- [72]. Zhuang, M., and Chen, R.F., "Applications of the Optimized Upwind Dispersion Relation Preserving Schemes for Multi-Dimensional Acoustic Problems." AIAA 98-2367, 1998.
- [73]. Zigg, D.W., "A Review of High-Order and Optimized Finite-Difference Methods for Simulating Linear Wave Phenomena," AIAA Paper 97-2088, 1997.
- [74]. Zigg, D.W., Lomax, H., and Jurgens, H., "An Optimized Finite-Difference Scheme for Wave Propagation Problems," AIAA paper 93-0459, 1993.